SEMICONDUCTOR DIODE LASER MATERIAL AND DEVICES WITH EMISSION IN VISIBLE REGION OF THE SPECTRUM

I. Ladany and H. Kressel

Prepared by
RCA LABORATORIES
Princeton, N. J. 08540
for Langley Research Center

NATIONAL AERONAUTICS AND SPACE ADMINISTRATION • WASHINGTON, D. C. • JULY 1975

1. Report No.	2. Government Accession No.	3. Recipient's Catalog No.
CR-2556		

4. Title and Subtitle	5. Report Date
SEMICONDUCTOR DIODE LASER MATERIAL AND DEVICES WITH EMISSION IN VISIBLE REGION OF THE SPECTRUM	July 1975
	6. Performing Organization Code

7. Author(s)	8. Performing Organization Report No.
I. Ladany and H. Kressel	PRRL-74-CR-74

9. Performing Organization Name and Address	10. Work Unit No.
RCA Laboratories Princeton, New Jersey 08540	11. Contract or Grant No. NAS1-11421
	13. Type of Report and Period Covered

12. Sponsoring Agency Name and Address	
Langley Research Center National Aeronautics & Space Administration Hampton, VA 23365	Final Report
	14. Sponsoring Agency Code

15. Supplementary Notes

16. Abstract

Two alloy systems, (AlGa)As and (InGa)P, have been studied for their properties relevant to obtaining laser diode operation in the visible region of the spectrum. (AlGa)As was prepared by liquid-phase epitaxy (LPE) and (InGa)P was prepared both by vapor-phase epitaxy (VPE) and by liquid-phase epitaxy. Various schemes for LPE growth were applied to (InGa)P, one of which was found to be capable of producing device material. However, as the LPE method is less advanced and in many ways less suitable than the VPE method, all the InGaP device work was done using vapor-phase epitaxy. The most successful devices were fabricated in (AlGa)As using heterojunction structures. At room temperature, the large optical cavity (LOC) design has yielded devices lasing in the red (7000 Å). However, because of the relatively high threshold due to the basic band structure limitation in this alloy, practical laser diode operation is presently limited to about 7300 Å. At liquid-nitrogen temperature, practical continuous-wave operation has been obtained for the first time at a wavelength of 6500 to 6600 Å, with power emission in excess of 50 mW. The lowest pulsed lasing wavelength is 6280 Å. At 223°K, lasing was obtained for the first time at 6770 Å, but with high threshold currents. The work dealing with cw operation at room temperature has been particularly successful with practical operation having been achieved to about 7800 Å. Many of the factors which have previously prevented reliable cw operation at room temperature have been identified and eliminated. Reliable power operation well in excess of 1000 hr has been demonstrated at power levels up to about 30 mW, and the limits remain to be established.

17. Key Words (Selected by Author(s))	18. Distribution Statement
Lasers Heterojunctions Large-optical cavities Vapor-phase epitaxy Liquid-phase epitaxy	Subject Category 76 Solid-State Physics

19. Security Classif. (of this report)	20. Security Classif. (of this page)	21. No. of Pages	22. Price*
Unclassified	Unclassified	147	$5.75

*For sale by National Technical Information Service, Springfield, Virginia 22151.

TABLE OF CONTENTS

TABLE OF CONTENTS (Continued)

LIST OF ILLUSTRATIONS

LIST OF ILLUSTRATIONS (Continued)

LIST OF ILLUSTRATIONS (Continued)

LIST OF ILLUSTRATIONS (Continued)

LIST OF ILLUSTRATIONS (Continued)

LIST OF ILLUSTRATIONS (Continued)

LIST OF ILLUSTRATIONS (Continued)

LIST OF ILLUSTRATIONS (Continued)

SEMICONDUCTOR DIODE LASER MATERIAL AND DEVICES WITH EMISSION IN VISIBLE REGION OF THE SPECTRUM

by

I. Ladany and H. Kressel
RCA Laboratories
Princeton, NJ 08540

SUMMARY

Two alloy systems, (AlGa)As and (InGa)P, have been studied for their properties relevant to obtaining laser diode operation in the visible region of the spectrum. (AlGa)As was prepared by liquid-phase epitaxy (LPE) and (InGa)P was prepared both by vapor-phase epitaxy (VPE) and by liquid-phase epitaxy. Various schemes for LPE growth were applied to (InGa)P, one of which was found to be capable of producing device material. However, as the LPE method is less advanced and in many ways less suitable than the VPE method, all the (InGa)P device work was done using vapor-phase epitaxy.

The most successful devices were fabricated in (AlGa)As using heterojunction structures. At room temperature, the large optical cavity (LOC) design has yielded devices lasing in the red (7000 Å). However, because of the relatively high threshold due to the basic band structure limitation in this alloy, practical laser diode operation is presently limited to about 7300 Å. At liquid-nitrogen temperature, practical continuous-wave operation has been obtained for the first time at a wavelength of 6500 to 6600 Å, with power emission in excess of 50 mW. The lowest pulsed lasing wavelength is 6280 Å. At 223°K, lasing was obtained for the first time at 6770 Å, but with high threshold currents.

The work dealing with cw operation at room temperature has been particularly successful with practical operation having been achieved to about 7800 Å. Many of the factors which have previously prevented reliable cw operation at room temperature have been identified and eliminated. Reliable laser operation well in excess of 1000 hr has been demonstrated at power levels up to about 30 mW, and the limits remain to be established.

Despite the achievement of a record low laser diode wavelength value, the research conducted on (InGa)P epitaxial materials using electroluminescence, photoluminescence, and cathodoluminescence leads to the conclusion that several major problems limit the use of this alloy for practical laser diodes.

(1) Heterojunction structures are impractical because of the metallurgical limitations inherent in the lattice parameter mismatch which is much larger with composition change than in (AlGa)As. Thus, efficient room-temperature lasing in the visible is difficult to achieve.

(2) While electron-beam-pumped lightly doped material shows that epitaxial (InGa)P is relatively efficient in the direct portion of the alloy composition range, the laser diodes fabricated have high threshold current densities and low differential quantum efficiencies. This is believed due to the difficulty of incorporating the requisite high dopant density without introducing an unacceptably high defect density. The dopant-related defects are intimately related to the existing flaws formed in the process of epitaxial growth. Despite the difficulties encountered in fabricating (InGa)P laser diodes, this program has resulted in diodes emitting at 77°K at $\sim$6420 Å in material desposited on GaAs substrates, and at 5980 Å in material deposited on GaP substrates, which is the first time such a short diode laser wavelength was achieved.

(3) Because of the relatively deep acceptor ionization energies, considerable freeze-out occurs at low temperatures. This results in poor power conversion efficiencies compared with those of (AlGa)As or GaAs devices.

I. INTRODUCTION

In the past decade, the field of semiconductor laser diodes has seen a continuing improvement with the most important change being due to the introduction of heterojunctions. The GaAs homojunction laser was replaced in 1968 by the (AlGa)As-GaAs heterojunction diode which greatly improved the room-temperature performance, thus making possible the first practical system's use of semiconductor laser diodes (ref. 1). Further evolution and sophistication in materials synthesis, based on the use of liquid-phase epitaxy to prepare very thin active region laser diodes, led to devices capable of high-duty-cycle operation in near-infrared. In parallel with the effort on improving GaAs lasers, research has been conducted over a period of years on other materials, including heterojunction lasers capable of emitting visible stimulated radiation; (AlGa)As and (InGa)P are of particular interest: (AlGa)As because of its characteristically excellent heterojunction devices and (InGa)P because of its relatively high direct-bandgap energy at room temperature ($\sim$2.2 eV). Extensive research was conducted in both materials at RCA Laboratories in the areas of synthesis of epitaxial layers and diode fabrication. The present research program was undertaken to explore the limitation of these alloys with regard to efficient visible stimulated emission from laser diodes. This work has included materials characterization, determination of the heterojunction requirements for carrier and radiation confinement, properties of dopants which would affect laser properties, and properties of laser diodes.

This Final Report describes the research performed during the period 24 April 1972 to 23 November 1974.

The authors gratefully acknowledge many valuable discussions with Dr. C. J. Nuese and the cathodoluminescence data provided by Dr. F. H. Nicoll.

In addition to the authors the following contributed to the research reported in this work: J. K. Butler, S. H. McFarlane (section on x-ray topography of InGaP), H. F. Lockwood, H. S. Sommers, Jr., and F. Z. Hawrylo. Technical support was provided by D. Gilbert, D. P. Marinelli, V. M. Cannuli, M. G. Harvey, and T. J. Zamerowski. The work at Yeshiva University was conducted under subcontract and is reported in Section VI and the Appendix. It was performed by Y. Juravel and P. M. Raccah.

II. REVIEW OF BASIC LASER DIODE REQUIREMENTS

In this section we review the basic requirements for obtaining stimulated emission from p-n junction diodes and the factors which affect the threshold current density and efficiency. Additional details of laser operation can be found in a recent book (ref. 3) and in a review chapter (ref. 4).

A. General Considerations

In direct-bandgap semiconductors (the only ones in which stimulated emission has been definitely observed), both photon emission and absorption occur without the need for a phonon to conserve momentum, because the conduction band minimum and valence band maximum are at the same $\bar{k}$ value in the Brillouin zone.

In direct-bandgap semiconductors, where this is not the case, photon emission and absorption require the participation of phonons. Lasing in indirect-bandgap semiconductors is improbable because the lowest energy band-to-band transition probabilities are much smaller than in the direct-bandgap semiconductors. Since the stimulated recombination rate is a function of the band-to-band absorption coefficient, the lower absorption coefficient for indirect transitions also means that the potential laser gain coefficient is correspondingly reduced.

Optical gain requires carrier population inversion such that the probability of photon emission with energy $h\nu$ is greater than the probability of absorption at the same photon energy. When minority carriers are injected into a semiconductor (for example, electrons into p-type material), thermodynamic equilibrium does not exist, but a steady-state distribution of carriers in the conduction and valence bands, independently, can be assumed to occur.

A "quasi-Fermi level" for electrons, F_c, and for holes, F_v, can be defined and the necessary condition for gain at a photon energy $h\nu$ is

$$F_c - F_v > h\nu \tag{1}$$

which requires a degenerate carrier distribution. Stimulated emission in p-type material requires the injection of a sufficient density of electrons to raise the quasi-Fermi level F_c (and lower F_v) sufficiently for condition (1) to be satisfied.

As shown in Fig. 1(a), in a highly forward-biased p-n junction, the injection electrons are distributed over a distance roughly equal to the diffusion length which can vary from $\sim$ 0.1 to 7 μm, depending on the material quality and doping. Figure 1(a) shows the carrier confinement which occurs if a potential barrier exists a distance, d, from the p-n junction interface, where d is *smaller* than the diffusion length. In Fig. 1(b), the potential barrier is due to a p^+-p heterojunction with a bandgap difference ΔE_g. Improved electron confinement reduces the volume which must be inverted and, hence, helps to reduce the threshold current density.

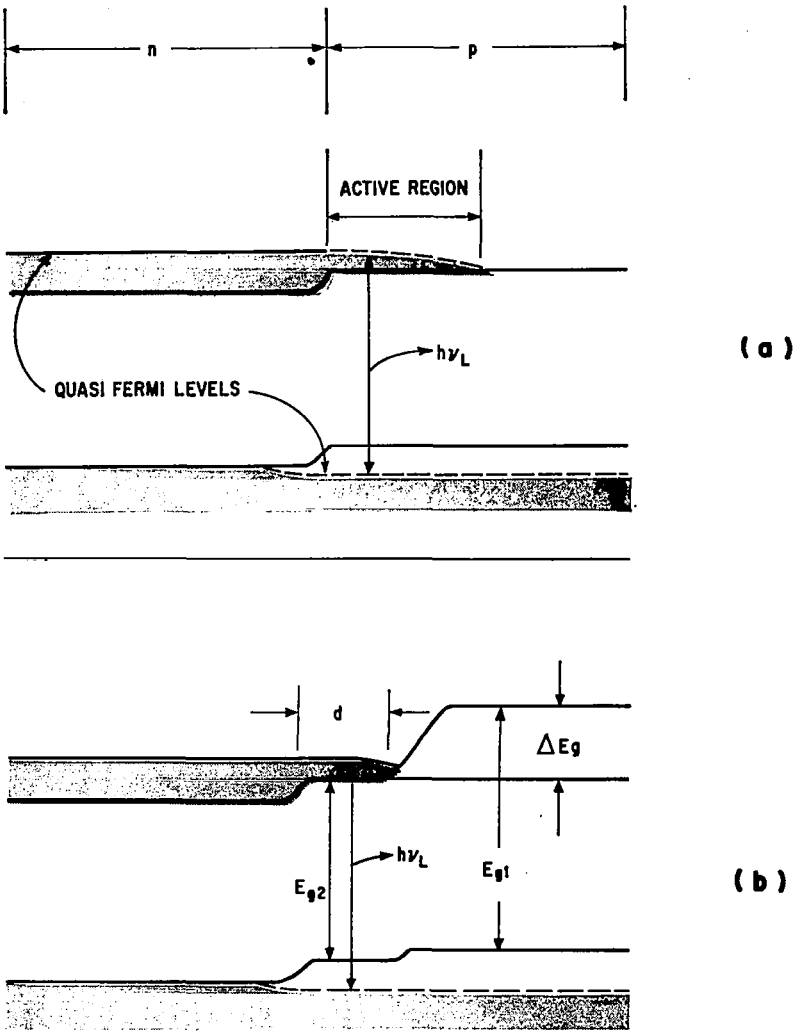

Figure 1. Electron distribution in a forward-biased p-n junction. (a) No potential barrier is present to confine the electrons and (b) a potential barrier is placed at a distance d (smaller than the diffusion length) from the p-n junction.

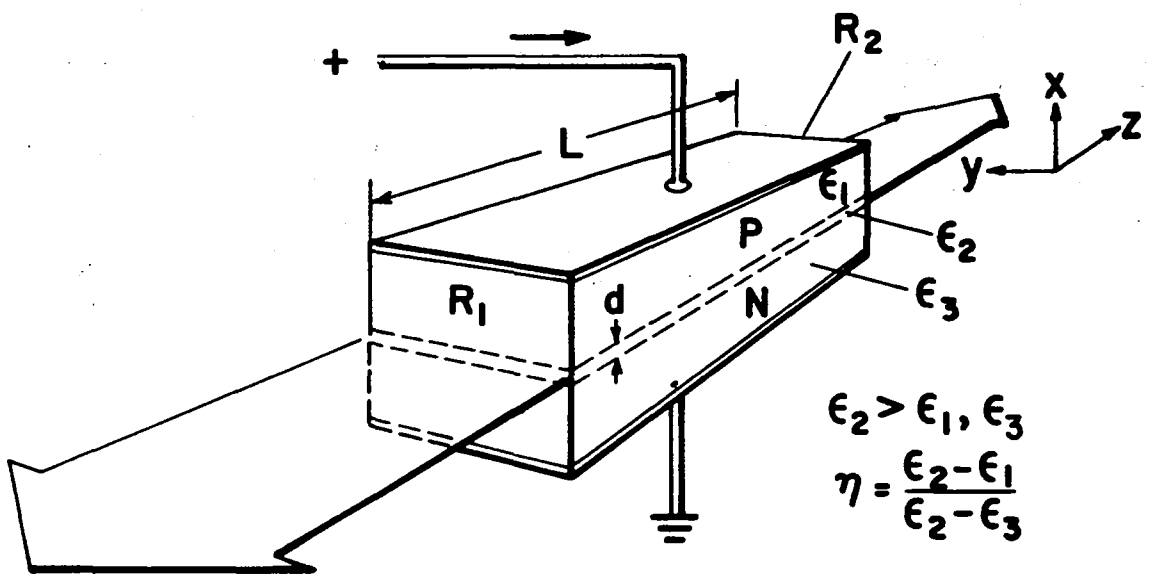

Figure 2. Three-region waveguide approximation of a heterojunction laser with active region width d and Fabry-Perot cavity length L.

In a Fabry-Perot cavity of length L (Fig. 2) with facet reflectivities R_1 and R_2 (0.32 for cleaved GaAs facets), lasing will begin when the optical gain just matches the losses during one pass of the beam in the cavity. The lasing threshold relationship between optical gain and losses can therefore be expressed as

$$R_1 R_2 \exp 2[(g_{th}-\alpha)] L = 1 \tag{2a}$$

or

$$g_{th} = \alpha + \frac{1}{2L} \ln \frac{1}{R_1 R_2} \tag{2b}$$

Here, g_{th} is the optical gain coefficient at threshold (which is a function of the current density), and α is the absorption in the cavity, which includes free carrier absorption, absorption in the noninverted regions adjoining the p-n junction plane, and absorption by material inhomogeneities (precipitates, for example).

The onset of lasing is characterized by a large increase in the exterior efficiency of the device because the light propagation inside the diode is in the plane of the junction and a fraction (1-R) of the light incident on the facet is emitted. The internal quantum efficiency, η_i, can be but need not be very high in direct-bandgap semiconductors (60 to 100% in good-quality GaAs). However, below threshold the isotropic spontaneous emission is for the most part absorbed.

Above threshold the external *differential quantum efficiency*, η_{ext}, is given by

$$\eta_{ext} = \eta_i \left(\frac{\ln 1/R}{\alpha L + \ln 1/R} \right) \tag{3}$$

where η_i is the internal quantum efficiency, and α is the internal absorption coefficient which also appears in Eq. (2), ($R_1 = R_2$).

B. Factors Affecting the Threshold Current Density

Theoretical estimates of J_{th} require a determination of g_{th} and the dependence of g_{th} on the diode current density. In the simplest approximation of a *two-level laser*, the gain coefficient is a linear function of the current density J,

$$g = \beta J \tag{4}$$

where the proportionality constant β is called the gain factor, which should be as large as possible. β can be given as

$$\frac{1}{\beta} = \frac{8\pi q \, n_2^2 \, \Delta\nu}{\eta_i \, \lambda^2 \, \Phi} \, d \tag{5}$$

Here, n_2 is the refractive index in the lasing region of width d, λ is the wavelength, $\Delta\nu$ is the recombination line width, and Φ is a temperature-dependent factor that takes into account the distribution of carriers in the bands ($\Phi = 1$ at $T = 0°K$). Implicit in Eq. (5) is the assumption that the optical emission is confined to the region of inverted population.

In highly doped semiconductors, the gain coefficient dependence on the current density is not easily calculated because the density of

states distribution is not accurately known, the band edges being perturbed by the internal field due to the ionized impurities. Furthermore, the inverted population region and the optical path do not necessarily overlap. The most general way of expressing the threshold current density is

$$J_{th} = \frac{d}{\eta_i \Gamma} J_{nom} \tag{6}$$

where d is the thickness of the region of inverted population in μm, Γ is the fraction of the optical modes confined to the inverted region, and J_{nom} is a function of g_{th}:

$$J_{nom} = \left[\frac{(\alpha + \frac{1}{L} \ln \frac{1}{R})}{\beta_o} \right]^{1/b} \tag{7}$$

Theory predicts an increase of β_o with decreasing temperature. The theoretical value of b is 1 to 3 at 300°K and $\sim$ 1 at low temperature. Since the value of Γ depends on the degree of optical confinement, waveguiding in the junction vicinity is necessary to keep it high. Furthermore, because the narrow inverted region in the vicinity of the p-n junction is bound by highly absorbing noninverted regions, waveguiding is also needed to reduce absorption losses.

Thus, it is clear from Eqs. (4) - (6) that low-threshold devices require *small d values* $\lesssim$ 2 μm , *a low absorption coefficient a, and high* η_i.

C. Device Design Considerations

Good optical and electron confinement in the inverted population region is desirable to obtain the highest possible gain coefficient for a given current density and to minimize absorption losses by preventing the spread of light into the lossy regions surrounding the inverted population region. Waveguiding occurs because the refractive index in the immediate vicinity of the p-n junction is generally higher than in the surrounding regions, mainly due to variation of the doping level and/or the bandgap energy. For purpose of analysis the schematic structure shown in Fig. 2 is helpful. The light emission is through the cleaved facets separated by a distance L.

Various laser structures have evolved, some of which (e.g., those with heterojunctions) have so far been most successful in the $Al_xGa_{1-x}As$-GaAs system. The simplest device is, of course, the diffused or epitaxial p^+n diode (*homojunction* laser) in which a modest amount of radiation confinement occurs as a result of the small refractive index decrease in the junction vicinity due to the bandgap shrinking in compensated material, Fig. 3(a). Such lasers have high threshold current density, even in the best material (60,000 to 100,000 A/cm^2 for GaAs), as a result of the poor radiation and electron confinement.

In the single heterojunction "close-confinement" laser [Fig. 3(b)], the threshold current density is considerably reduced to about 10,000 A/cm^2 by confining the radiation to an active region only 2 μm wide. This structure can be used wherever a heterojunction can be fabricated with a minimum of interfacial strain.

The double heterojunction (DH) laser, Fig. 3(c), allows a further reduction in J_{th} if the active region between the heterojunctions is under 1 μm. Values of J_{th} of 900 A/cm^2 have been obtained with DH lasers at 300°K. Specific aspects of design for room-temperature cw lasers are described in Section V.

A more sophisticated laser structure is the *large optical cavity* (LOC) device shown in Fig. 3(d) where the "waveguide region" consists of an n-type (3) and a p-type (2) region surrounded by two heterojunctions. In effect, region 2 is a narrow leaky waveguide, of width d_2, within the thicker waveguide of width d_2+d_3, enclosed by the heterojunctions. The operation of the LOC structure is briefly as follows. The radiation is produced in region 2 by radiative recombination of electrons injected from region 3, while the radiation is confined within the large cavity, regions 2 plus 3. The larger optical cavity is desirable to reduce the optical flux density (which affects the diode reliability). Furthermore, absorption losses are lower and the possibility exists of reducing the far-field beam divergence. However, J_{th} will increase with increasing d_3 [i.e., decreasing Γ in Eq. (6)].

D. Summary of Requirements for Efficient Laser Diodes

(1) The material should have a direct bandgap with high η_i.
(2) The material must be as free as possible from inclusions, dislocations, and inhomogeneities.
(3) The diode should incorporate a method of confining the radiation and carriers to a small region in the junction vicinity. A heterojunction is the best way of obtaining this confining barrier.

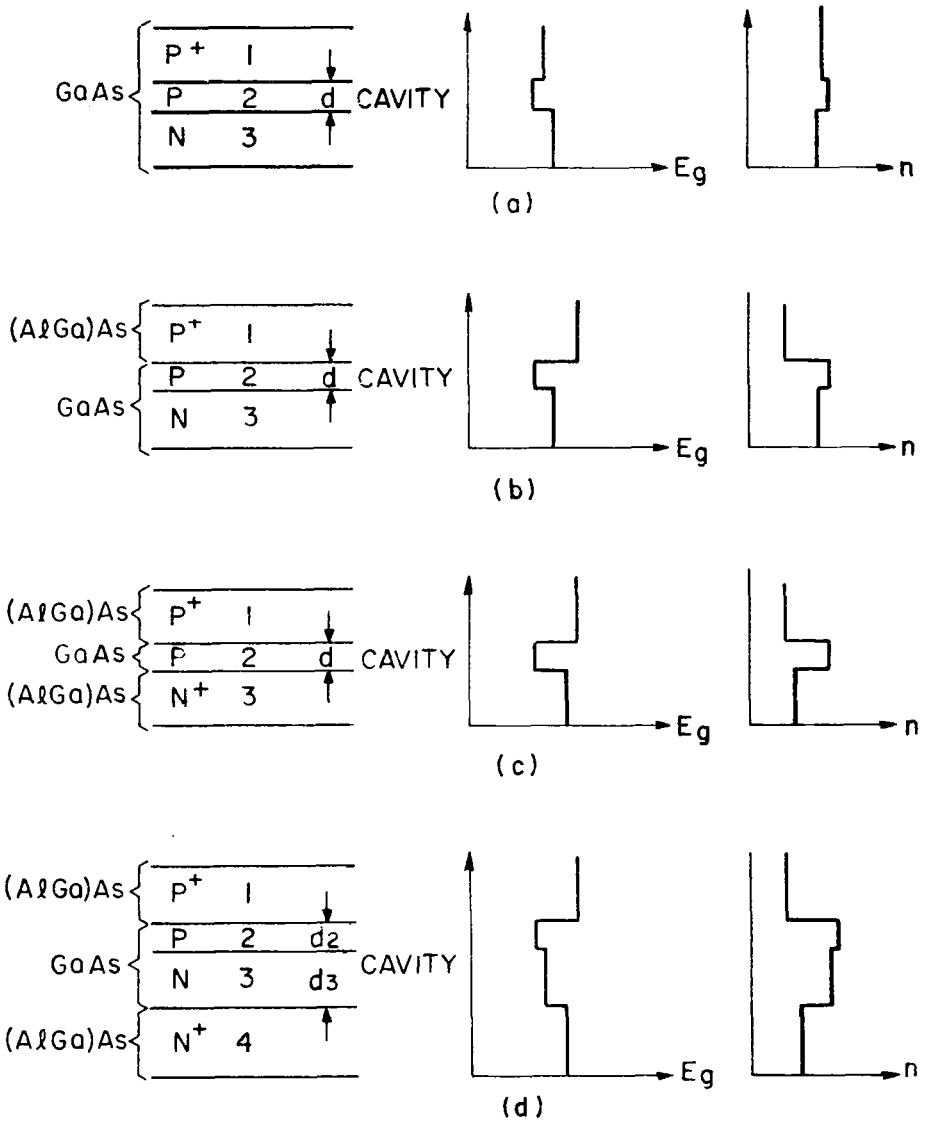

Figure 3. Schematic cross section of various laser structures in the (AlGa)As alloy system showing the variation of the bandgap energy and of the refractive index at the lasing photon energy. (a) Homojunction laser made by liquid-phase epitaxy, (b) single heterojunction close-confinement laser, (c) double heterojunction laser, and (d) large optical cavity (LOC) laser. Note that the diode design concepts are general and applicable to all types of laser diodes provided that heterojunctions can be made where the interface is reasonably free of defects and is also planar.

E. Choice of Materials for Visible Laser Diodes

Four III-V alloys are of potential interest for visible laser diode construction because they can be doped both n- and p-type: $In_{1-x}Ga_xP$, $In_{1-x}Al_xP$, $GaAs_{1-x}P_x$, and $Al_xGa_{1-x}As$. Table I shows the value x_c change where the "direct" to "indirect" bandgap transition occurs and the bandgap energy at that composition. Single crystals of these alloys can be prepared epitaxially, in platelet form or as polycrystalline ingots. However, for practical devices, single crystals deposited epitaxially on suitable substrates are needed; therefore, epitaxial materials were the central feature of this program.

TABLE I

Direct-Bandgap Materials for Visible Laser Diodes

Material	Energy Gap Range @ 300°K (eV)	x_c*	Egc @ 300°K† (eV)	Egc @ 77°K† (eV)	Major Problems
GaN	3.5	---	---	---	p-type doping
$In_{1-x}Ga_xP$	1.34-2.26	0.7	∿2.2	∿2.30	strain; lattice mismatch
$In_{1-x}Al_xP$	1.34-2.45	0.44	∿2.3	∿2.4	strain; lattice mismatch; difficult to prepare
$GaAs_{1-x}P_x$	1.44-2.26	0.46	1.99	2.08	strain; lattice mismatch
$Al_xGa_{1-x}As$	1.44-2.16	0.32-0.37	1.92	2.01	limited direct bandgap alloy range

*Value of x where the material changes from "direct" to "indirect."

†Direct bandgap energy at x_c.

Of the four alloys, (AlGa)As is best prepared by liquid-phase epitaxy and Ga(AsP) by vapor-phase epitaxy; both techniques have been used to prepare (InGa)P. Liquid-phase epitaxy is probably the best technique for preparing (InAl)P because of the difficulty of preparing compounds containing aluminum in the usual reactors used in vapor-phase epitaxy. Unfortunately, because of the fundamental thermodynamic consideration (related to the fact that InP and AlP have widely differing melting temperatures), it is very difficult to reproducibly grow (InAl)P even by liquid-phase epitaxy because of the much larger segregation coefficient of Al as compared with that of In. This program concentrated on (InGa)P and (AlGa)As devices. The potential advantage of (InGa)P is that it is theoretically possible to fabricate laser diodes having emission wavelengths in the yellow portion of the spectrum in contrast to (AlGa)As, which is limited to red-stimulated emission.

Assuming defect-free material, the internal quantum efficiency depends on alloy composition even in the direct-bandgap alloy composition range. If the direct- and indirect-conduction band minima are separated by an energy large with respect to kT, the fraction of the injected carriers "lost" by transfer from the direct- to the indirect-condition band minima is insignificant. Based on reasonable assumptions concerning the density of states distribution in the direct- and indirect-conduction band minima, the relative dependence of η_i on the bandgap energy (and hence, lasing photon energy) can be calculated for several alloy systems. These calculated results are compared in Fig. 4

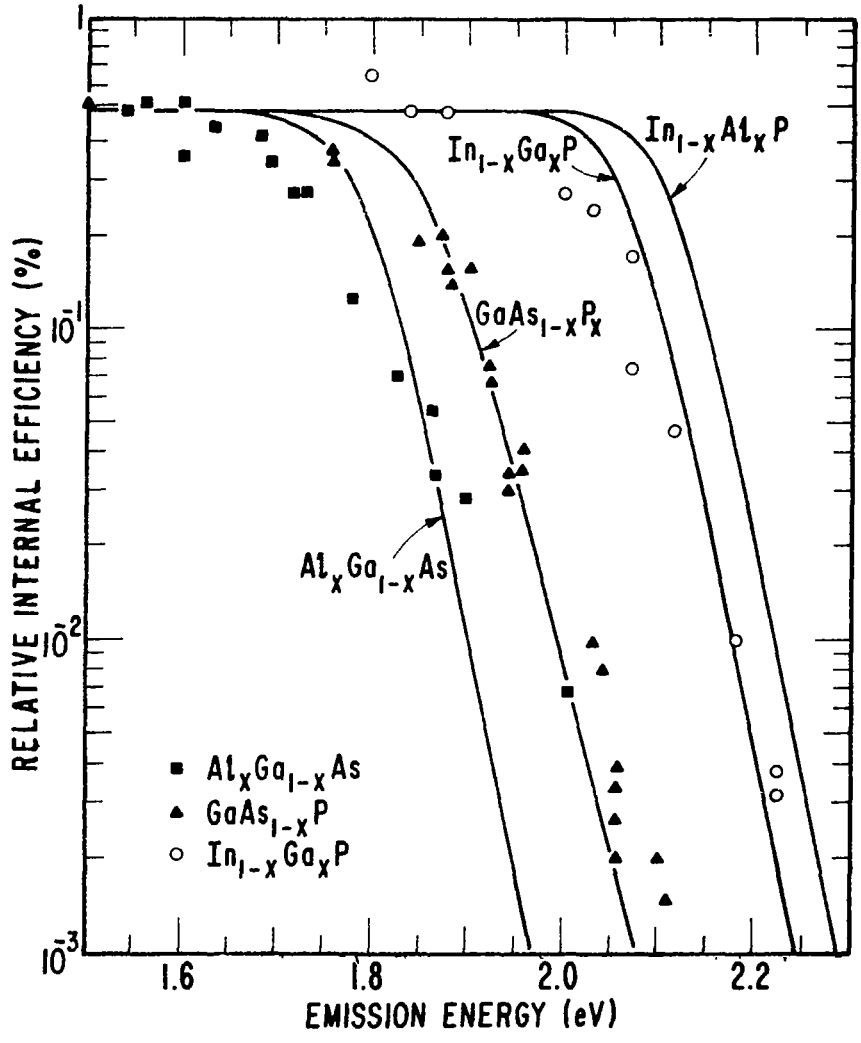

Figure 4. Experimental variation of the relative internal quantum efficiency in various alloys as a function of the bandgap energy. The experimental points are compared with the theoretical curves.

with the experimental spontaneous efficiency (ref. 5). The agreement between theory and experiment is reasonably good. However, the fall-off in η_i is faster than predicted in some regions, most probably because of the metallurgical flaws resulting from the lattice mismatch between the epitaxial films and the substrate.

Figure 4 shows that in $In_{1-x}Ga_xP$, η_i can remain essentially *constant* to $E_g \cong 2$ eV, which means that room-temperature lasing with good efficiency is potentially possible to about $\lambda \cong 6400$ Å (assuming that the lasing photon energy is below the bandgap energy by about 0.05 eV, as is the case in other materials). The theoretical advantage to be obtained from using $In_{1-x}Al_xP$ is small; and in view of expected difficulties in preparing this material, it does not appear to be worthwhile at this time to concentrate on its development.

Good-quality heterojunctions are desirable for laser diodes, as discussed above. This means that we wish to use materials with as small a change in the lattice constant with composition as possible to minimize interfacial defects. Figure 5 shows the dependence of the lattice constant on x in the alloys of potential interest. (AlGa)As is unique among the alloys because the lattice parameter hardly changes

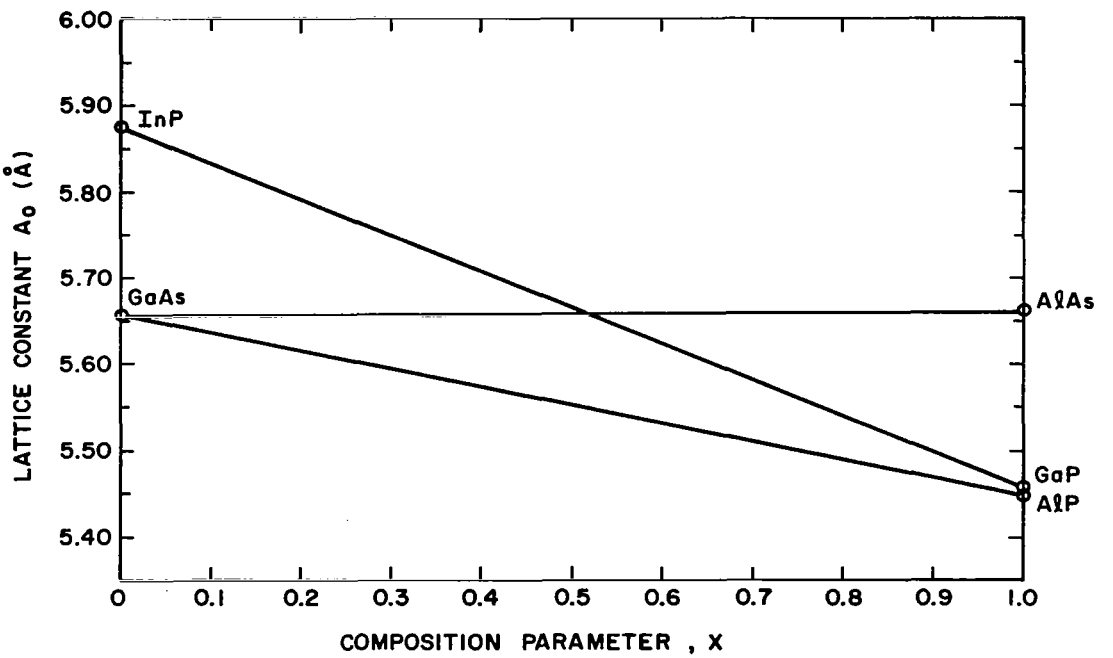

Figure 5. Lattice parameter vs. x for various alloys.

with composition. Ga(AsP) is second in this respect. While Ga(AsP) laser diodes have been fabricated by several investigators in the past (ref. 3), their performance was inferior to those of (AlGa)As devices. The small additional indirect bandgap energy range of Ga(AsP) does not appear to justify a significant technological investment aimed at laser diode fabrication.

The choice of substrates for the material is of crucial importance since the closest possible lattice constant match is desired to minimize the defect density of the layer. Figure 5 shows that only for (AlGa)As alloys is GaAs an excellent substrate for all compositions. However, for $In_{.49}Ga_{.51}P$ and $In_{.49}Al_{.51}P$, GaAs also provides a suitable substrate. For other materials, the lattice parameter mismatch is greater and compositional grading must be used to minimize the dislocation density in the epitaxial layer whether deposited on InP, GaAs, or GaP. (AlP single crystals are difficult to grow and are hygroscopic.)

III. PROPERTIES OF MATERIALS AND DEVICES: $Al_xGa_{1-x}As$

The (AlGa)As epitaxial layers were all prepared by liquid-phase epitaxy using a multiple-bin apparatus of the type first described by Nelson (ref. 6) in which a slider is used to move the GaAs substrate into bins containing Ga solutions, with various constituents needed to grow the desired material. With modifications of the apparatus to make it more flexible (ref. 7) it is possible to reproducibly grow epitaxial layers only a fraction of 1 μm thick. The bandgap energy of the material is controlled by changing the Al content in the Ga solution. Figure 6 shows the variation of the bandgap energy of $Al_xGa_{1-x}As$ with x. The work in this program was restricted to the Ga-rich side of the alloy system.

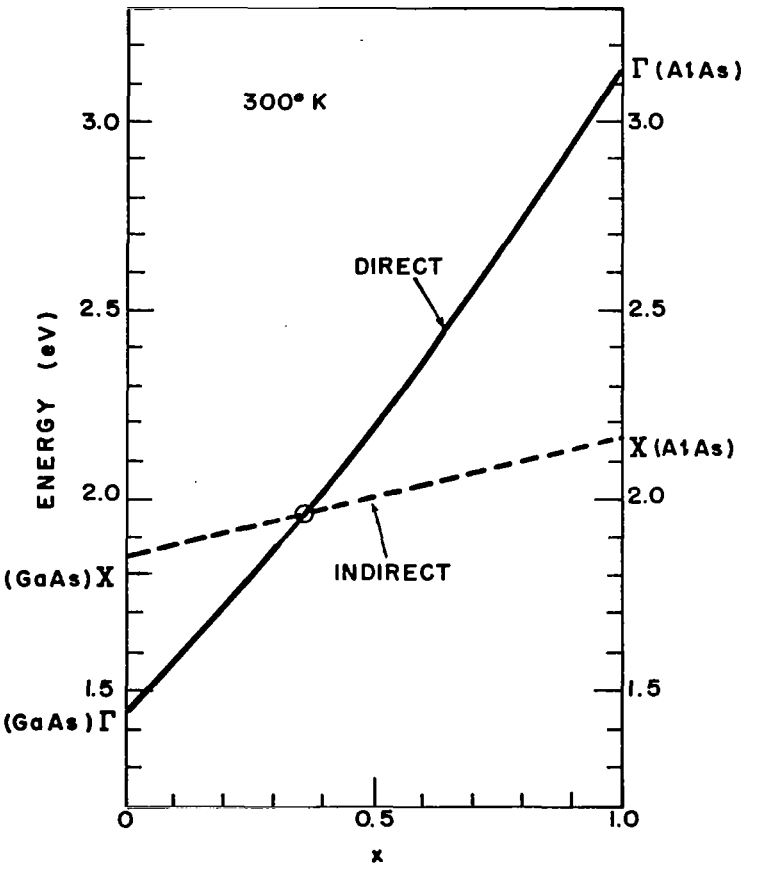

Figure 6. Direct and indirect bandgap in $Al_xGa_{1-x}As$ as a function of x at 300°K.

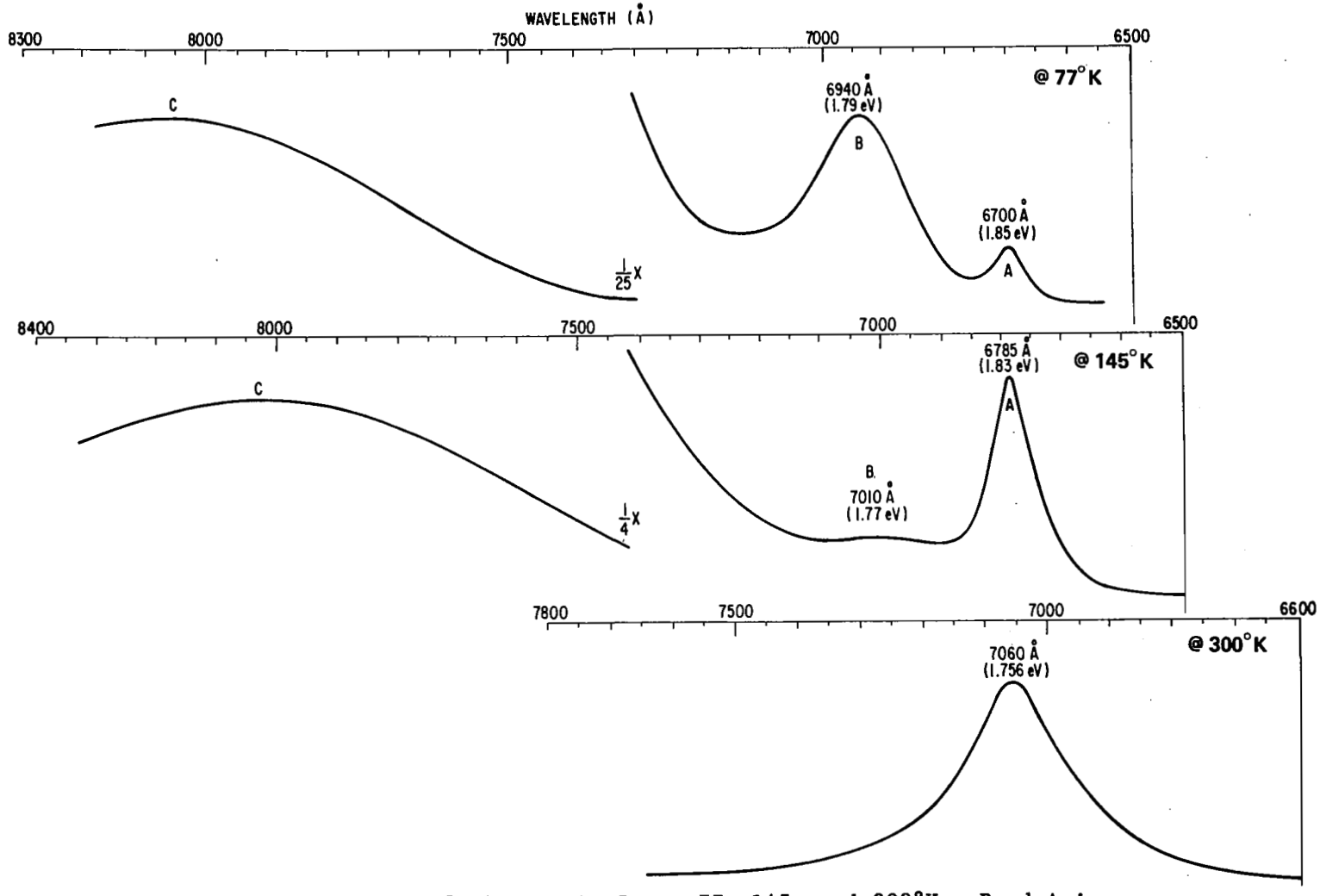

Figure 7. Photoluminescence of $Al_{.2}Ga_{.8}As$:Ge at 77, 145, and 300°K. Band A is near bandgap luminescence, band B is due to transitions terminating on the Ge acceptor, and band C is due to an atomic complex involving Ge.

A. Donors and Acceptors in $Al_xGa_{1-x}As$

Germanium, Si, and Zn are commonly used to dope the GaAs recombination region in heterojunction laser diodes. Because of the deep bandtailing obtained with Si doping, the threshold current densities at room temperature are typically lower than those obtained with Ge or Zn for comparable waveguide region widths. However, in the case of $Al_xGa_{1-x}As$ devices, designed for visible emission, we found that neither Si nor Ge were suitable dopants. Silicon in $Al_xGa_{1-x}As$ has been previously studied (ref. 8). The relatively deep levels formed as x increases may not participate in the stimulated emission and would then increase the absorption and thus degrade the lasing properties. Similarly, the shallow Ge acceptor in GaAs ($E_a \approx 0.035$ eV) increases its ionization energy with increasing Al, even in the direct-bandgap portion of the alloy system. This was studied by photoluminescence (PL) and cathodoluminescence (CL). Figure 7 shows for example, the photoluminescence of a sample of $Al_{.2}Ga_{.8}As$:Ge at 77, 145, and 300°K. At 300°K only a single emission band is seen in this sample, with a weak emission band (not shown) centered at about 8000 Å. At 145°K, two high energy bands centered at 1.83 eV (band A) and 1.77 eV (band B) are observed, but the strong infrared band C dominates the emission. At 77°K, band B is more prominent than band A, with band C even more prominent. A study of samples of varying Al and Ge content led to the conclusion that band A is basically the bandgap transition, while band B is due to the radiative transitions from the conduction band to the Ge acceptors, about 0.06 eV from the valence band edge. Band C is due to a complex involving Ge and possibly some native defects such as vacancies. The above results are consistent with the data of Alferov et al. (ref. 9).

Various samples with different Al compositions were studied, and the Ge ionization energy was deduced from peak energy differences between A and B. The resultant E_a estimate is shown in Fig. 8 as a function of the room-temperature bandgap energy. The ionization energy increases greatly with bandgap energy and very steeply in the vicinity of $E_g \cong 1.92$ eV, where the material becomes indirect.

The behavior of Zn is far more favorable for utilization in laser diodes. The ionization energy appears to remain essentially constant at $E_a \approx 0.03$ eV in the direct-bandgap portion of the alloy system; no deep levels appear to be introduced as long as the doping level is in the useful 10^{18} cm^{-3} range. In fact, we found that the best lasers were made using Zn in the recombination region, and this dopant has been used exclusively in the latter phase of our program.

With regard to the usual shallow donors, such as Te, we find that the ionization energy also remains small (~ 0.05 eV) in the direct-bandgap alloy. Thus, no difficulties are encountered in n-type doping.

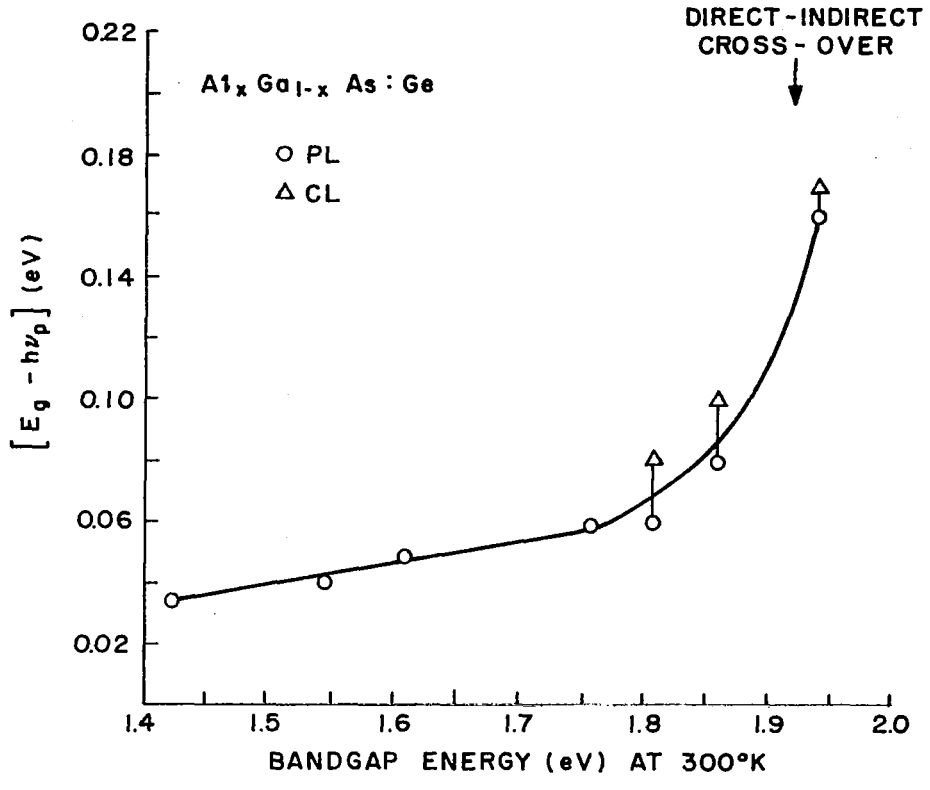

Figure 8. Estimated ionization energy of "isolated" Ge acceptor in $Al_xGa_{1-x}As$ as a function of the room-temperature bandgap energy.

B. Carrier and Optical Confinement in Heterojunction Diodes*

As reviewed in Section II, radiation confinement and minority-carrier confinement by heterojunctions is known to be important in the improved operation of laser diodes. However, few quantitative experimental data are available concerning the dependence of either the refractive index step (Δn) or the carrier confinement on the barrier height. These are basic data needed in heterojunction device design. The confinement was measured in a special diode structure over a temperature range 77 to 350°K. In addition, measurement of Δn at the lasing energy of GaAs is reported for various heterojunction barrier heights.

*The work in this section was performed in collaboration with H. F. Lockwood, J. F. Butler, and H. S. Sommers, Jr.

The structure used in the *carrier confinement* study is shown in Fig. 9. The p-type GaAs:Si recombination region (0.4 μm thick) is bracketed by two low-barrier heterojunctions. The thick p-type region 4 ensures a satisfactory current distribution in the diode by preventing current crowding under the small-area ohmic contact. Since the uppermost p-type layer is essentially transparent to the radiation emitted in layers 2 and 3 (except for free carrier absorption), the

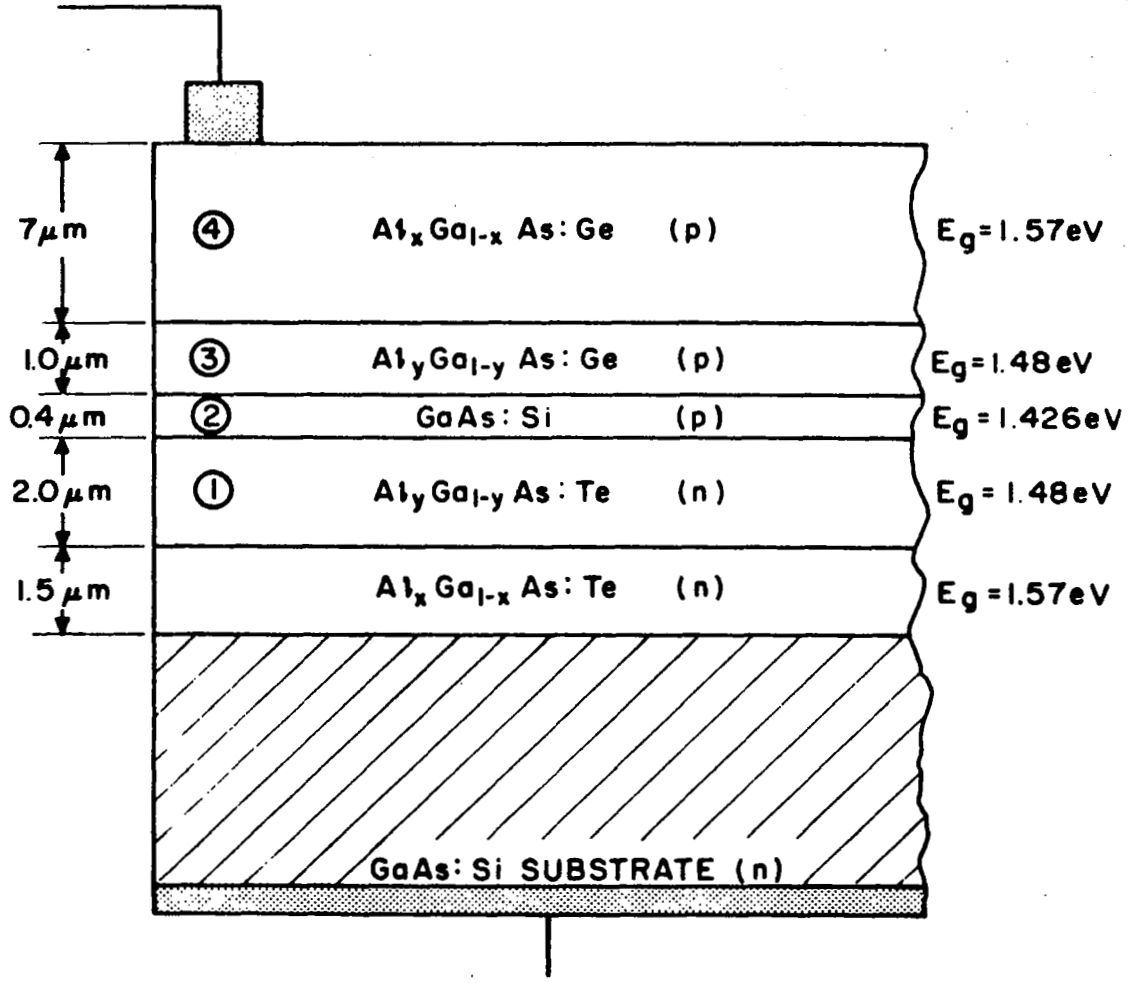

Figure 9. Cross section of the heterojunction structure studied for carrier confinement. The spontaneous emission is observed through the top (p) layer of the diode. The edges are covered with black wax to eliminate spurious emission peaks.

observed spontaneous spectra are essentially undistorted. (Observation of the spontaneous emission from the edge of such diodes is frequently misleading because of "ghost" peaks due to selective absorption in the substrate.)

Reference to the simplified band diagram in Fig. 10 shows that some of the electrons injected from the n-type region 1 into region 2 are able to diffuse across region 2 and surmount the potential barrier between regions 2 and 3 to recombine in region 3. Thus, the spontaneous emission spectra will consist of an emission band from region 2 (GaAs) and another higher energy band due to region 3. By using Si as the dopant in region 2 we ensure that the emission peak is substantially below the bandgap energy of GaAs, which eases the identification of radiation from regions 2 and 3 by reducing the spectral overlap.

Figure 11 shows the spontaneous emission spectrum of the diode (logarithmic plot) as viewed through its surface. At 300°K, two

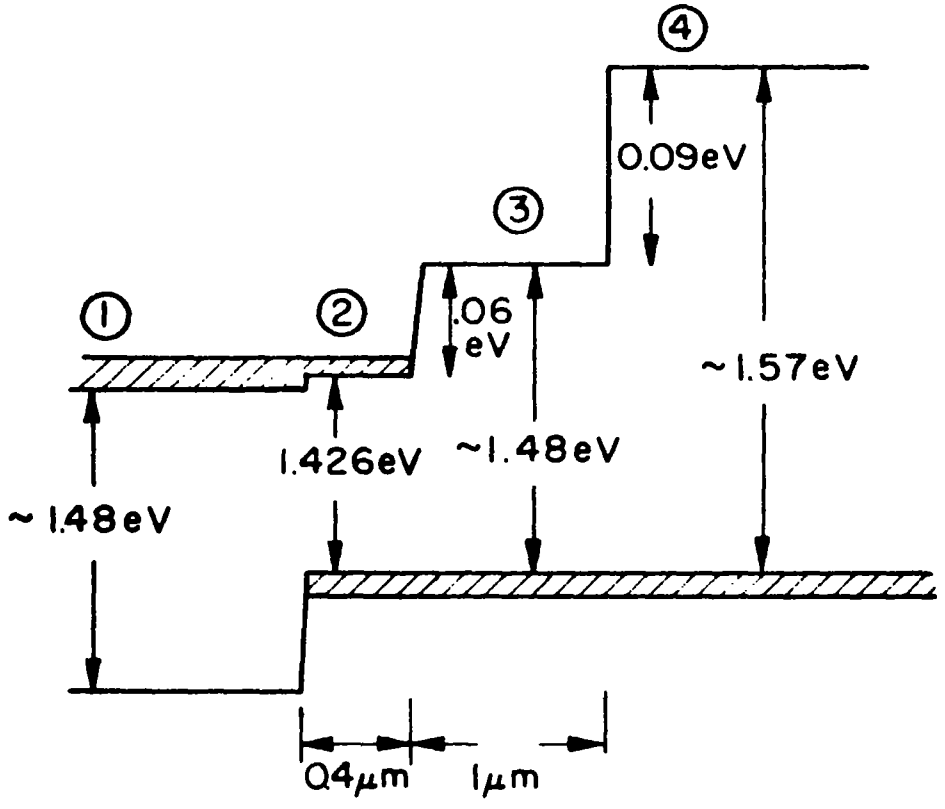

Figure 10. Band structure of the heterojunction diode shown in Fig. 9 under strong forward bias. The bandgap in each of the regions is shown.

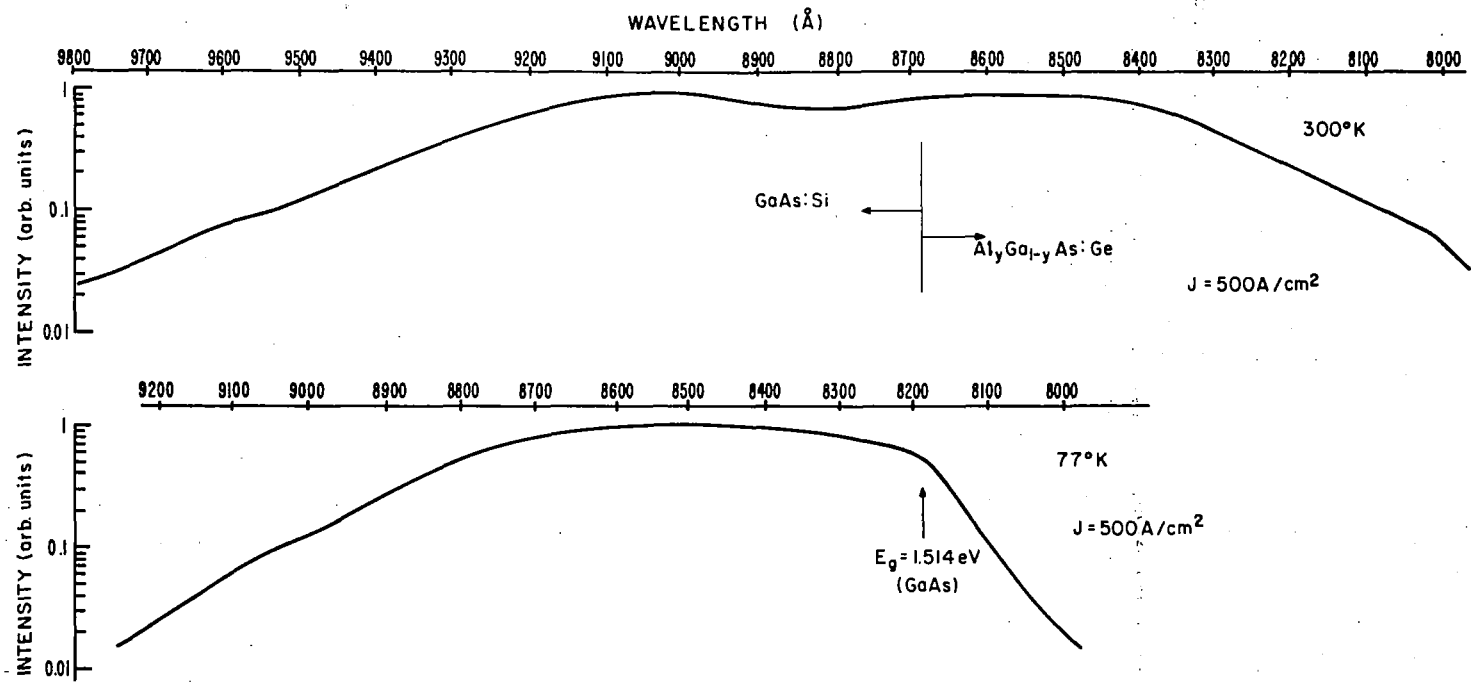

Figure 11. Spontaneous spectra at 300 and 77°K at a current density of 500 A/cm^2. At 300°K emission is seen from both region 2 (GaAs:Si) and region 3 [(AlGa)As:Ge]. At 77°K only the (GaAs:Si) radiation is observed.

relatively broad bands are seen to arise from recombination in regions 2 and 3; the vertical line indicates the GaAs bandgap. At 77°K, on the other hand, only emission originating in the GaAs region is observed, with no measurable (AlGa)As emission.

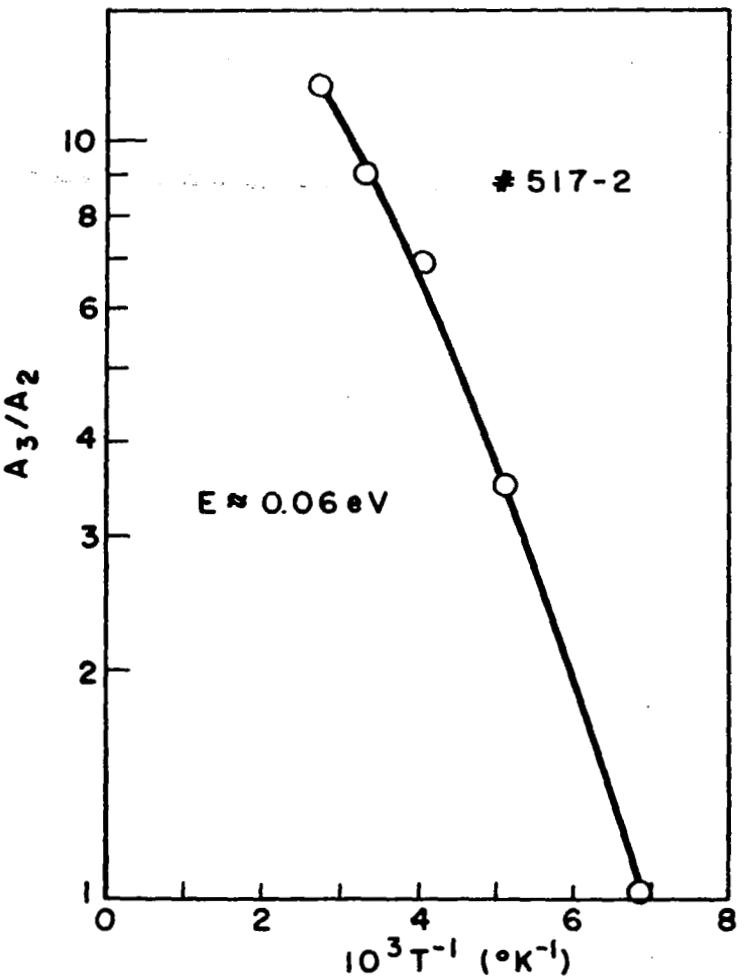

Figure 12.

The ratio of the intensity of the radiation from region 3 (A_3) to that from region 2 (A_2) as a function of temperature.

If the heterojunction barrier can be represented by a simple potential energy step, we expect increasing carrier diffusion from region 2 into region 3 as the temperature is increased. This is indeed the case, as shown by the increase with temperature of the intensity ratio A_3/A_2 of the radiation from the (AlGa)As region 3 to the radiation from the GaAs region 2, Fig. 12. These data can be fitted to an expression such as

$$A_3/A_2 \propto \exp\ (-\ E/kT) \qquad (8)$$

with

$$E \approx 0.06 \text{ eV} \tag{9}$$

This value of E is consistent with the measured energy difference at the heterojunction of 0.054 eV on the basis of photoluminescence measurements. Thus, the change in confinement indicated by the temperature dependence of A_3/A_2 as deduced from Fig. 11 is consistent with the model of thermal excitation over the heterojunction barrier 2-3 which is essentially temperature-independent.

The heterojunction bandgap energy difference was generally determined on the basis of photoluminescence measurements on material selected from the wafers studied, and checked on individual diodes studied by photocurrent measurements. The photocurrent measurements were made by irradiating the edge of an assembled diode with the chopped spectral array slip output from a monochrometer in conjunction with a phase-locked detection system. Figure 13 shows a typical photocurrent curve as a function of the incident wavelength for a large optical cavity (LOC) laser at room temperature. For *symmetrical* double heterojunction diodes, the analysis of the photocurrent and its relationship to the bandgap

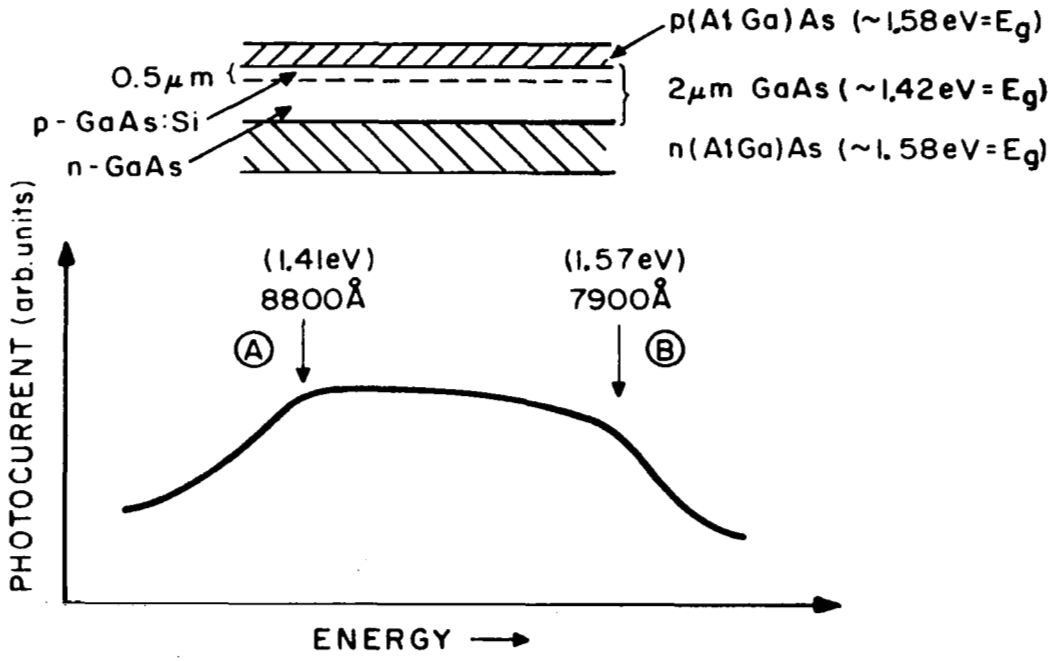

Figure 13. Photocurrent vs. incident photon energy of a typical LOC laser diode irradiated at the lasing facet. The bandgap energies shown in the cross section of the device are estimated from photoluminescence measurements.

energy differences is simple. In Fig. 9, the knee in the curve at A (at ∿ 1.41 eV) results from strong absorption in the GaAs:Si region while the knee at B (∿ 1.57 eV) is due to absorption in the (AlGa)As. Only light absorbed within a distance of the order of a diffusion length from the p-n junction (see the cross section of the device in Fig. 9) can contribute to the photocurrent. These energies are close to the known bandgap of GaAs, 1.426 eV, and that of the (AlGa)As layers, ∿ 1.58 eV. Thus, the photocurrent measurement provides a very simple, nondestructive method of determining the bandgap difference at the heterojunctions (ΔE_g ∿ 0.16 eV in the above case) in the same device whose far-field radiation pattern can be analyzed.

The transverse profile of the laser beam (perpendicular to the plane of the p-n junction) provides information on the variation of the refractive index step at the heterojunctions. Although reflectivity measurements can, in principle, be used to determine Δ, the small widths of the regions of interest, the small Δn differences, and the possible gradients in the Al concentration at the heterojunctions complicate such a measurement. Furthermore, the *useful* Δn value appropriate to the operation of the optical waveguide region of the laser diode can best be determined from radiation patterns as described previously (ref. 11). Once the radiation pattern has been obtained and the transverse mode order determined, only the heterojunction spacing need be known to calculate Δn at the lasing wavelength.

Figure 14 shows Δn, determined from pattern fitting, as a function of the bandgap energy difference at the heterojunction. For comparison we also show the theoretical curve for Δn at ∿ 9000 Å vs. ΔE_g (ref. 12). The agreement is satisfactory, particularly since the difference in the doping level on opposite sides of the heterojunctions was not considered in the theoretical curve. Such doping differences will have the effect of increasing Δn for a given ΔE_g by as much as 0.01 in a typical laser diode (refs. 13 - 15).

From the work described in this section, we conclude that irrespective of the requirements for optical confinement, a bandgap discontinuity of about 0.10 eV at the p-p heterojunction is needed to obtain significant carrier confinement.

C. Laser Diode Properties

Laser diodes of the LOC and simple double heterojunction type were made, with the active region consisting of (AlGa)As near the direct-indirect cross-over composition.

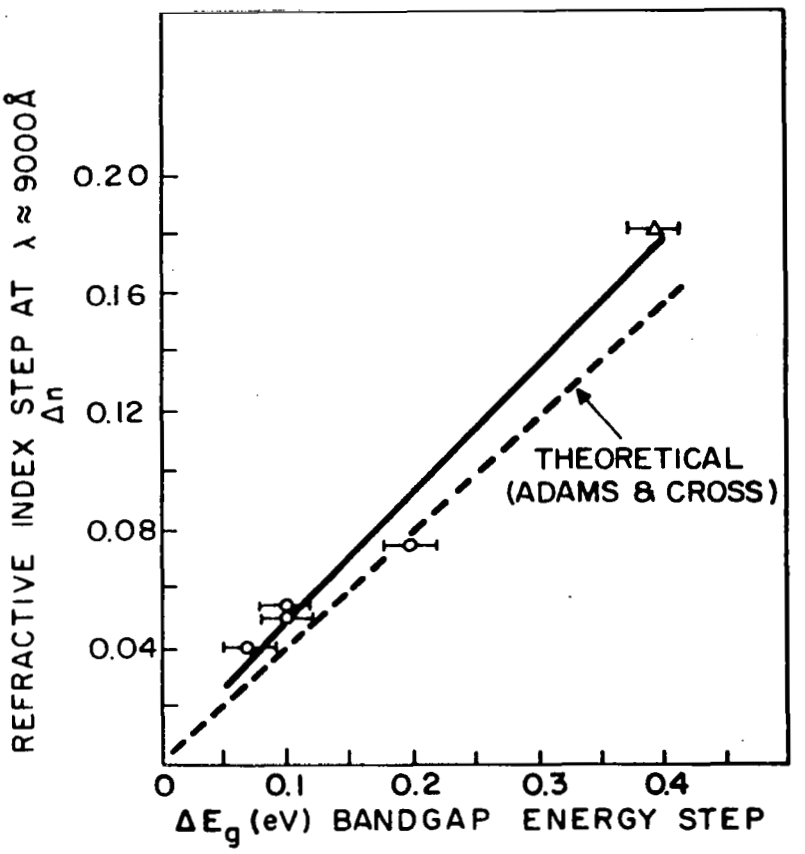

Figure 14. Refractive index step (Δn) at 9000 Å as a function of the bandgap energy step at the heterojunction at room temperature. The theoretical curve of Adams and Cross (ref. 12) does not include the contribution to Δn due to differences in the free carrier concentration.

Figure 15 shows a typical double heterojunction device used to explore the material limits and to fabricate 77°K cw lasers in which the 1-μm-thick active region was Zn-doped to a level of 10^{17} to 10^{18} cm^3. The n-type regions of the diodes were doped with Te. The uppermost p-type region consisted of a thin (∿ 5 μm) GaAs region heavily doped with Zn to minimize the series resistance of the diodes. The active region of the diodes was about 1 μm thick, while the higher bandgap $Al_xGa_{1-x}As$ n- and p-type regions were 3 to 5 μm thick. The diodes were mounted p-side down with indium on copper packages (ref. 16), of the type shown in Fig. 16 and operated on a cold finger. The diode dimensions, with cleaved facets and sawed sides, were typically 100 μm x 300 μm. For low-temperature operation, Zn rather than Ge is used for the acceptor doping because of the lower Zn acceptor ionization energy.

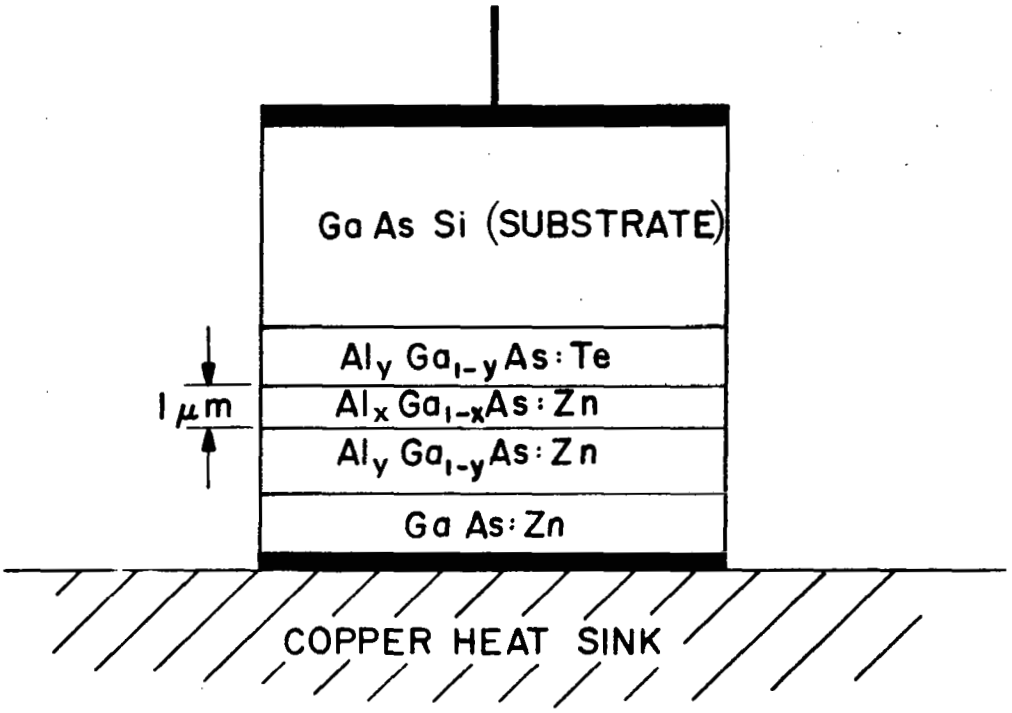

Figure 15. Schematic profile of double heterojunction structure used for devices described in Fig. 17 and for 77°K cw operation.

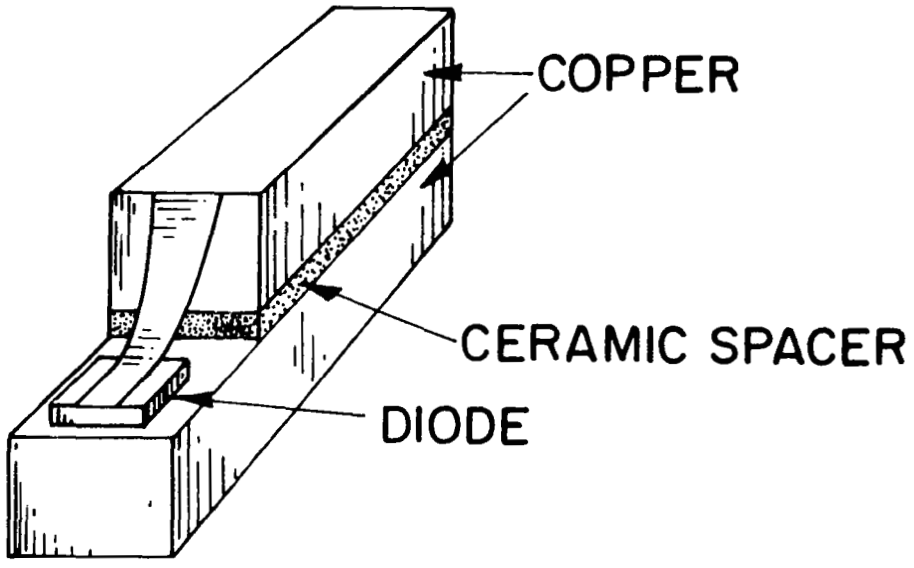

Figure 16. Mount used to test diodes (ref. 16), including room temperature and 77°K cw operation.

Diodes were made with varying $Al_xGa_{1-x}As$ compositions to determine the effect of alloy composition on the 77°K threshold current density. In all cases the heterojunction barrier height was maintained at about 0.1 eV. As indicated in the previous section, this barrier height is sufficient for good radiation and carrier confinement up to room temperature, while minimizing the lattice parameter mismatch. Figure 17 shows the threshold current density at 77°K of laser diodes with different emission wavelengths made from material in the direct-bandgap composition range. For comparison we also show similar data for single heterojunction diodes, as previously reported (ref. 17). The lower threshold for the double heterojunction diodes is due to their narrower active regions of 1 μm compared with about 2 μm for the single heterojunction units. For both types of diodes the threshold current density

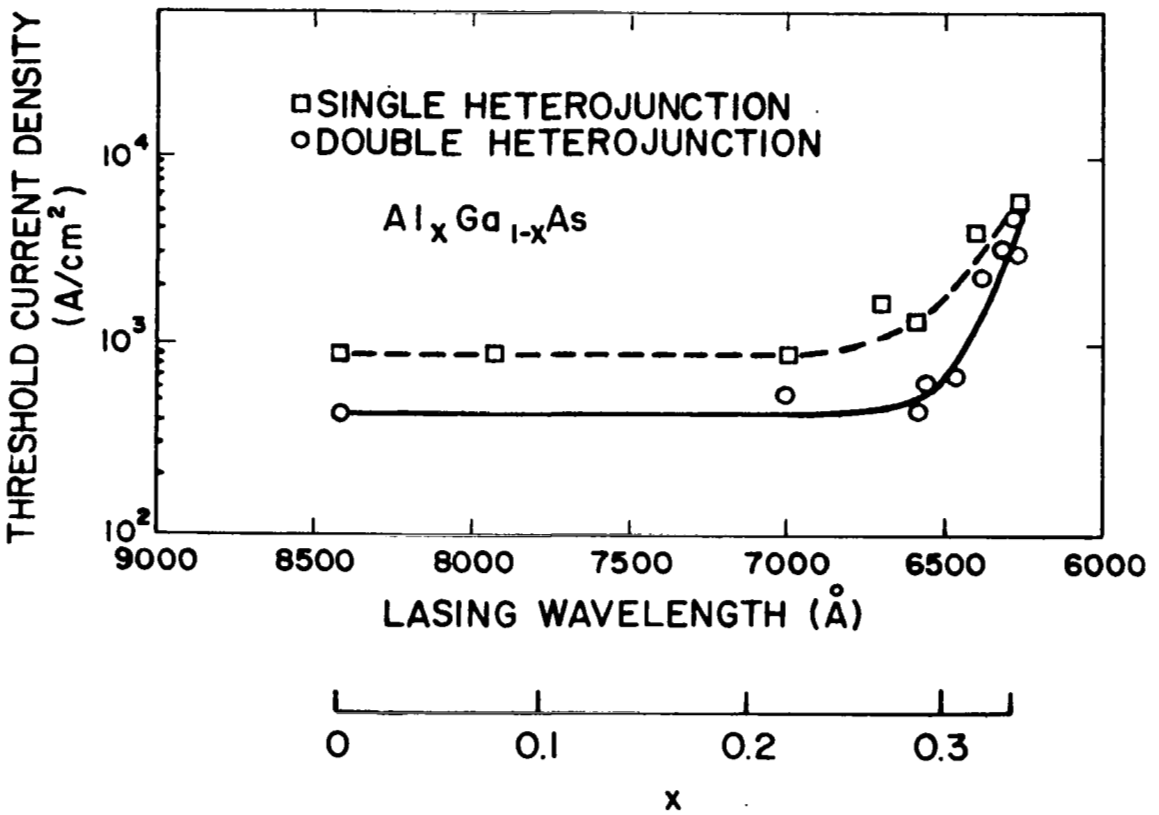

Figure 17. Threshold current density of single heterojunction laser diode (ref. 16) and present double heterojunction laser (pulsed) diodes at 77°K in direct bandgap $Al_xGa_{1-x}As$. The width of the active region of the single heterojunction devices is 2 μm, and in the double heterojunction units, 1 μm.

is essentially constant between 8500 Å (GaAs) and 6500 Å ($Al_{.3}Ga_{.7}$), as is the differential quantum efficiency (30 to 60% typically). The increase in J_{th} for units with λ_L < 6500 Å is due to the thermal depopulation of electrons in the $\bar{k} = 0$ conduction band minimum. The lowest lasing wavelength of 6280 Å, with J_{th} = 5000 A/cm^2, is limited because the indirect bandgap energy is lower than the direct bandgap for materials with a higher Al content.

The threshold current density increases steeply with temperature for diodes made from material near the bandgap "cross-over" composition, as qualitatively expected from the thermal change in the distribution of electrons in the bands. This is illustrated in Fig. 18 for a diode

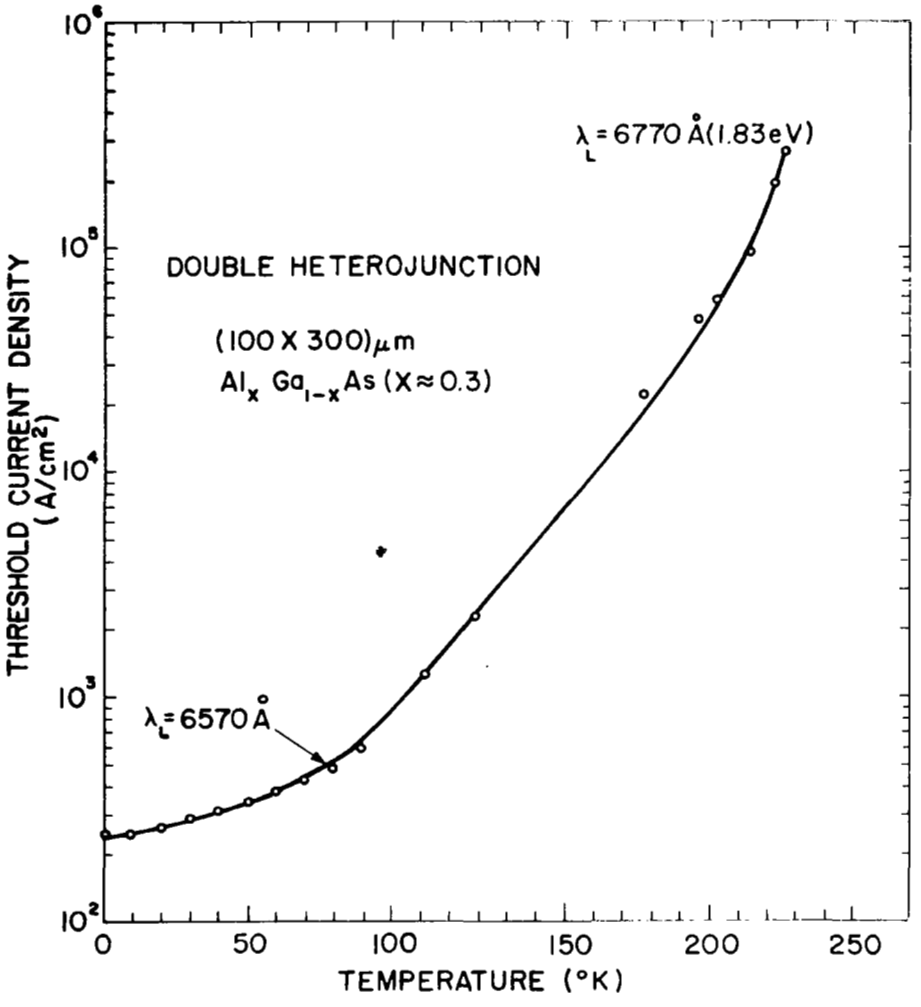

Figure 18. Threshold current density as a function of temperature of a double heterojunction laser diode with $Al_xGa_{1-x}As$:Zn in the 1-μm-wide active region as a function of dc current.

with $Al_{.3}Ga_{.7}As$ in the active region. While lasing was observed up to 223°K (λ_L = 6770 Å), the threshold current density increases by nearly a factor of 10^3 from its value at 77°K. (This compares with a factor of ∿ 10 for diodes made from material well removed from the cross-over region.) Tests of various diodes with equal bandgap energies showed that some differences existed in the threshold current dependence on temperature. It is possible that the strain in various diodes differed, which could affect the high-temperature threshold current density.

Continuous-wave operation of diodes with λ_L > 6560 Å is easily achieved since the threshold current density is well below 1000 A/cm^2. The amount of power which can be obtained depends on the heat sinking and thermal resistance of the diodes. Figure 19 shows a typical curve of the power emitted as a function of dc current from a diode lasing (J_{th} = 656 A/cm^2) at 6570 Å. This is the shortest cw lasing wavelength so far reported for a laser diode. The spectral width is 20 Å, significantly above threshold, and the beam divergence at the half-power

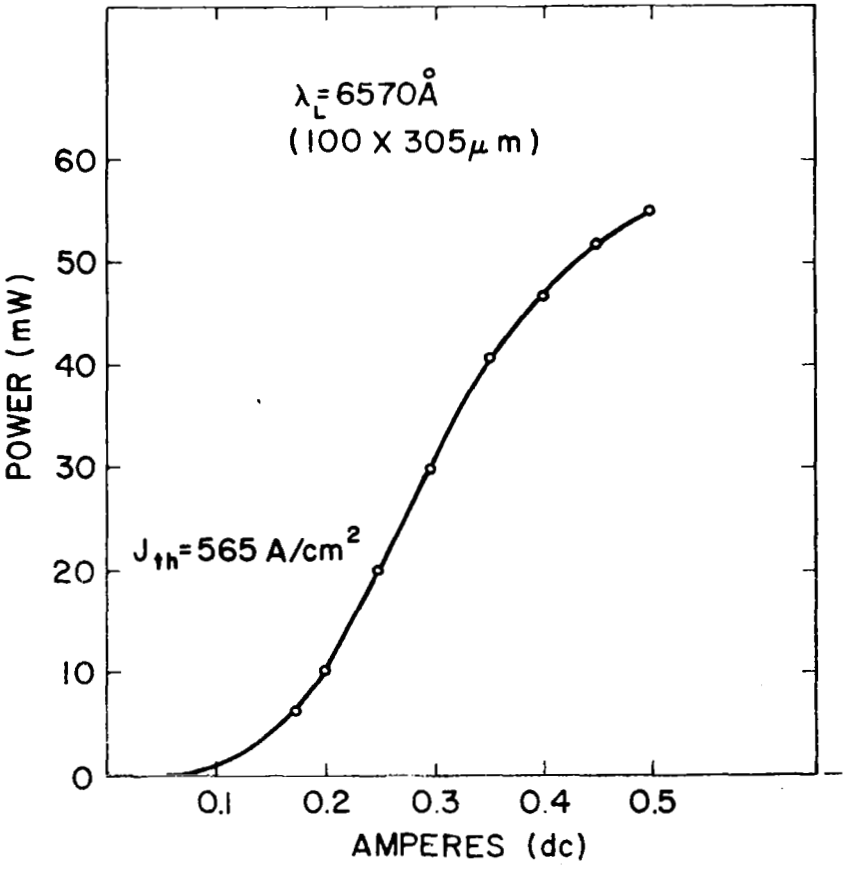

Figure 19. Power output from one side of a double heterojunction diode emitting at a wavelength centered at 6570 Å at 77°K.

point is 30° x 20°. With single heterojunction diodes having a higher threshold current density, cw operation was limited to 6635 Å (ref. 17), and a double heat sink (i.e., both p- and n-sides) was needed, in contrast to the simpler diode assembly used here.

The available life test of devices of this type is still limited to rather short operation (order of 10 hr) during which time no permanent deterioration in output was observed. However, it is important to prevent contamination of the emitting facet which can occur if oil is allowed into the cold chamber or liquid nitrogen comes in contact with the diode. The tests were all conducted with the diodes on a cold finger (i.e., without immersion into liquid nitrogen).

Room-temperature laser diode operation has been limited to wavelengths above ∿ 7000 Å. Figure 20 shows the dependence of J_{th} normalized in terms of spacing between the heterojunctions to facilitate comparison. The increase in J_{th} with decreasing λ_L is strongly affected

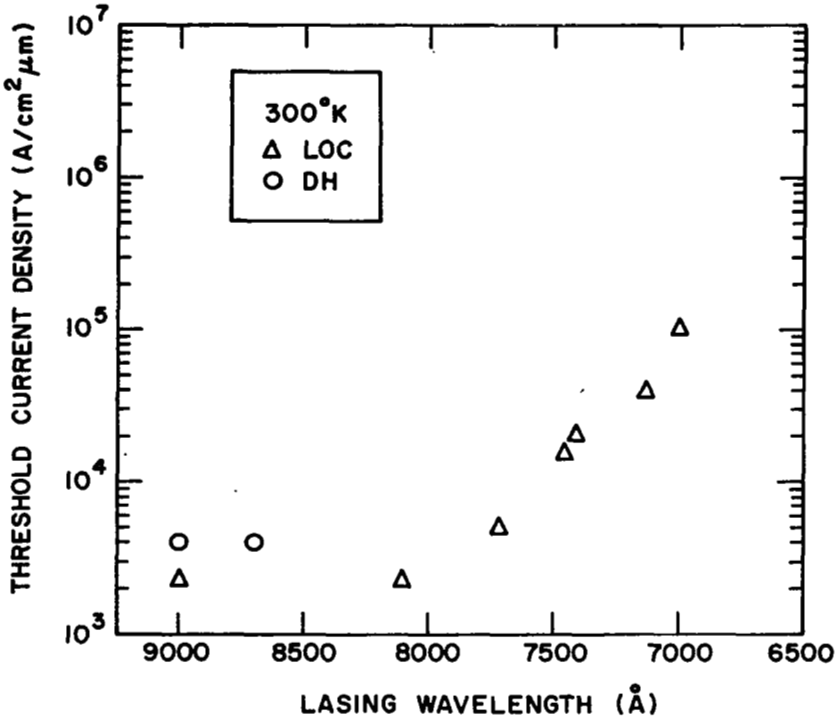

Figure 20. Threshold current density (normalized to a 1-μm waveguide region thickness) at room temperature as a function of lasing wavelength. Two types of structures were studied: large optical cavity units (LOC) and simple double heterojunctions (DH) using Zn as the acceptor dopant. For the DH structures, the heterojunction spacing was ∿1 μm.

by the thermal depopulation of electrons near the direct-indirect crossover composition. We found that the LOC structure was the only one which resulted in consistent laser action at 7000 Å, while the simple double heterojunction diodes (even with the same heterojunction spacing of 1 μm) did not lase consistently at that wavelength. It is unlikely, of course, that this experimental observation represents a fundamental limitation. A more probable explanation is that the superlinear dependence of the gain coefficient on the current density results in a more favorable situation in the case of the narrow recombination region LOC diode than in the double heterojunction device.

The threshold current density at 7000 Å of about 100,000 A/cm^2 is too high for most practical applications. The diodes emitting at 7300 to 7400 Å are of greater practical interest, since they can be seen while their threshold current density is lower. Figure 21 shows the power output as a function of drive current at room temperature of a laser emitting at 7360 Å having a threshold current density of about 39,000 A/cm^2. The heterojunction spacing of this laser was 1 μm. Further extensive discussion of laser diodes specifically designed for room-temperatue operation will be found in Section V.

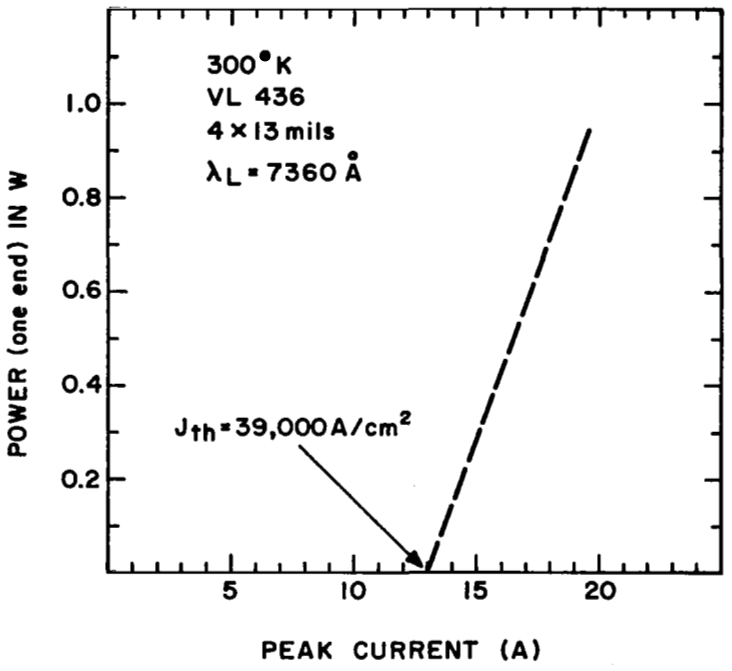

Figure 21. Power output (one side) as a function of peak diode current at room temperature.

IV. PROPERTIES OF MATERIALS AND DEVICES: $In_{1-x}Ga_xP$

A. Preparation of (InGa)P by Vapor-Phase Epitaxy

The technique used for preparing epitaxial layers of (InGa)P by vapor-phase epitaxy has been described in detail elsewhere (ref. 18). The growth apparatus is shown schematically in Fig. 22. The use of separate quartz tubes to contain the In and Ga source materials allows the independent control of the HCl concentrations over each of the metal sources. HCl reacts with Ga and In to form monochlorides of these metals,

$$yM(\ell) + HCl(g) = yMCl(g) + (1-y)HCl(g) + \frac{y}{2} H_2(g) \qquad (10)$$

Here, M = In or Ga and y = mole fraction of HCl consumed in the reaction. The metal monochlorides are carried in hydrogen into the mixing zone where they mix but do not react with gaseous phosphine, the source of phosphorus. In the reduced temperature of the deposition zone, where the substrate is positioned, (InGa)P is formed as an epitaxial film with HCl as the gaseous by-product according to the reaction:

$$MHCl(g) + P^*(g) + H_2(g) = MP(s) + HCl(g) \qquad (11)$$

Here, P^* denotes PH_3 and the products of the decomposition of PH_3, (P_2 and P_4). *In situ* doping with n- and p-type dopants is accomplished with H_2Se and Zn vapor respectively, using sidearms as shown in Fig. 22. Junctions are formed by introducing the dopants sequentially during growth without removing the substrate.

This system allows the gradual changing of the alloy composition or more abrupt transitions if heterojunctions are desired. Grading is accomplished at a given temperature by changing the ratio of the HCl flow rates to the In and Ga sources (HCl_{In}/HCl_{Ga}) (see Fig. 23). Precision electronically activated gas-flow controllers are used for each of the metal sources.

The appearance of the wafer surface is generally smooth; however, surface defects such as hillocks may occur whenever small leaks exist in the growth apparatus. The substrate wafer preparation prior to growth is also important in this regard. For the GaAs substrates used for the bulk of our work, etching in Karo's acid of the <100> oriented substrates was found satisfactory.

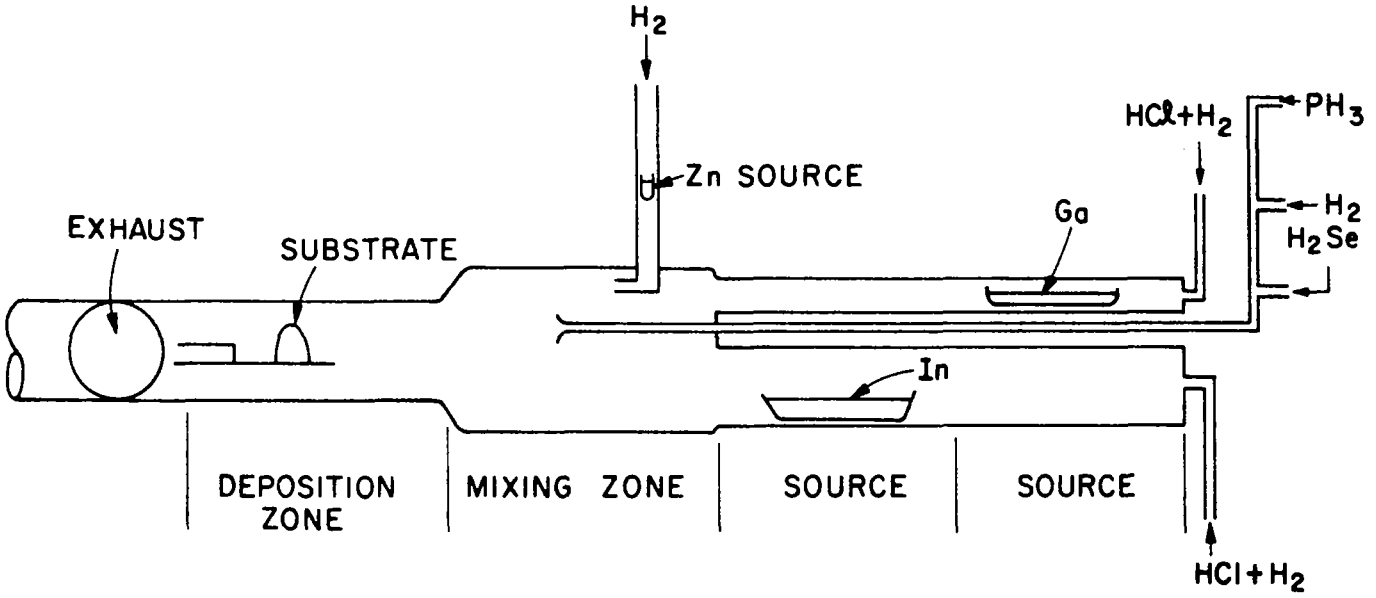

Figure 22. Schematic representation of the growth system used for the vapor-phase epitaxial deposition of $In_{1-x}Ga_xP$.

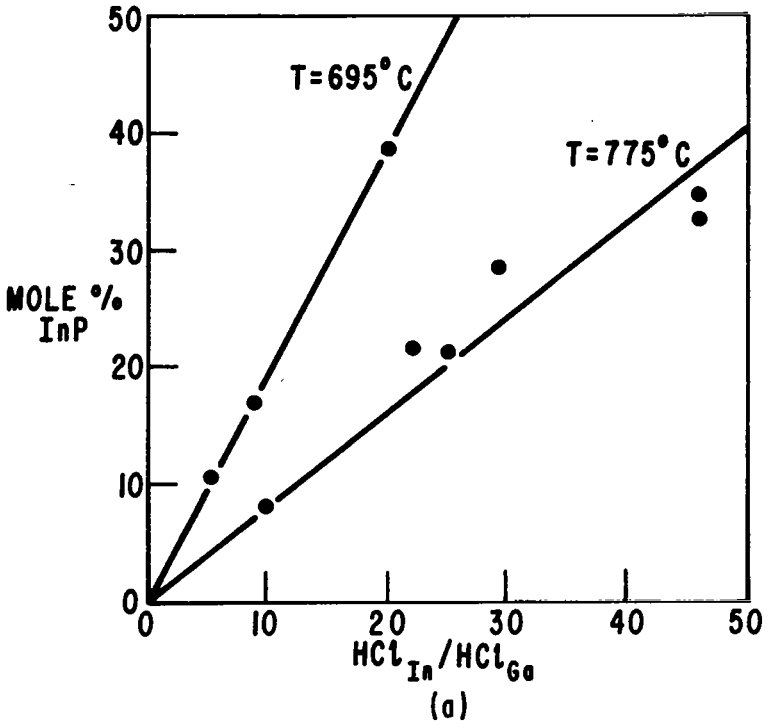

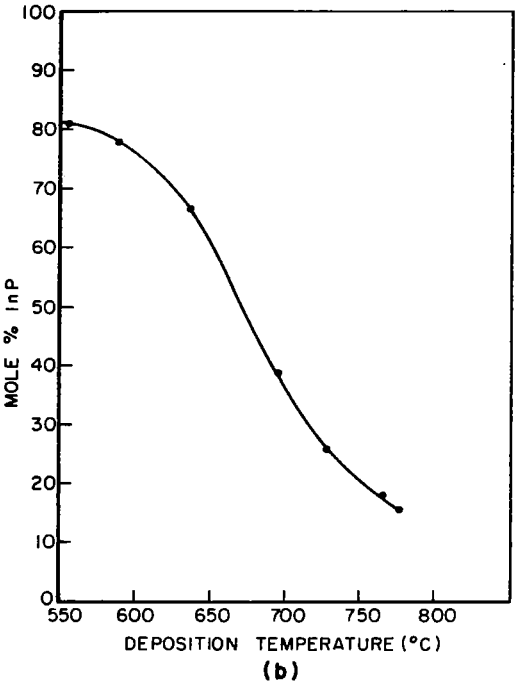

Figure 23.

The dependence of the mole fraction of InP in the $In_{1-x}Ga_xP$ alloy on (a) the ratio of the HCl flow rate over the In and Ga sources and (b) deposition temperature (ref. 18).

The undoped layers have a carrier concentration of 10^{15} to 10^{16} cm^{-3} and were always n-type. Silicon is believed to be the major contaminant in the material. The hydrogen carrier gas was purified in a palladium diffuser. The HCl and phosphine gas used were the purest commercially available.

B. Behavior of Donors and Acceptors

Studies were made of material properties relevant to lasing, in particular of the properties of the highly doped materials ($\gtrsim 10^{18}$ cm^{-3}) required for homojunction diode lasers.

Previous studies had dealt with luminescence from $In_{1-x}Ga_xP$ prepared by various techniques as a function of composition (refs. 18-26). However, detailed studies of the emission spectra over a broad temperature range in material with well-controlled dopants had not been reported. We, therefore, studied epitaxial material doped with Cd, Zn, Se and without intentional doping (lightly doped n-type) deposited by vapor-phase epitaxy on GaAs substrates. Various luminescence bands involving shallow donors and acceptors are identified, and ionization energy values are deduced from the data. In the case of the most heavily doped material (p-type, Zn-doped) we find new deep-level emission bands due to complex centers involving Zn. Such material has a very low radiative efficiency.

The photoluminescence measurements were made using pulsed argon laser excitation (4880-Å line) with an incident average power density of ~ 0.06 W/cm^2 and peak power density of ~ 15 W/cm^2. The spot size was sufficiently small (about 0.2 cm diameter) that the compositional uniformity could be assumed to be perfect. The samples were mounted on a cold finger inside a cryostat. The 4.2°K data were obtained by immersing the samples in liquid helium. An RCA photomultiplier with a negative-electron-affinity GaAs cathode was used for the measurements, and the data shown are as-recorded because of the uniform spectral response in the wavelength range studied.

The experimental data presented in this section concern n- and p-type samples. Since the spectra of all but the most heavily Zn-doped sample have similar features, we begin with the most lightly doped n-type sample (#UN-1) to establish a frame of reference. Note that because of the slight ($\lesssim 1$ mole %) compositional differences between samples (Table II), it was not possible to compare the emission spectra on the basis of the *absolute* peak photon energies but only on the basis of the *relative* positions of the various bands.

TABLE II

Properties of $In_{1-x}Ga_xP$ Samples Tested at 300°K

Sample (a)	Doping Density n or p (cm^{-3})	Mobility μ (cm^2/V-sec)	PL Intensity (c)	Mole Fraction GaP, x (d)
Cd-1 (p)	9.3×10^{17}	43	855	0.505
Cd-2 (p)	4.0×10^{17}	37	755	0.501
Cd-3 (p)	1.4×10^{17}	35	234	0.505
Cd-4 (p)	1.8×10^{16}	28	221	0.505
Zn-1 (p)	5.4×10^{17}	31	335	0.505
Zn-2 (p)	5.4×10^{18}	18	11	0.511
Se-1 (n)	1.0×10^{17}	1170	(b)	
Se-2 (n)	7.2×10^{17}	810	965	0.517

(a) Cd-doped, Zn-doped or Se-doped. Analysis of the Cd-doped material showed no detectable amount of Zn ($\leq$0.6 ppm).

(b) Not measured.

(c) Only a single emission band peaked at $\sim$1.90 eV was seen at 300°K in all samples.

(d) Determined from the empirical relationship $h\nu = 1.35 + 0.735x + 0.70x^2$ (ref. 39).

1. N-Type Material. - As shown in Fig. 24, four major bands are seen in the "undoped" n-type sample #UN-1 ($n \cong 3 \times 10^{15}$ cm^{-3}) of $In_{.497}Ga_{.503}P$ which contains only residual (and unidentified) donors and acceptors. The two highest energy bands, separated by 7 $\pm$ 1 meV, are denoted A_1 and A_2. The two lower energy bands, B_1 and B_2, are similarly separated by $\sim$ 8 meV. Figure 24 shows the increase of the intensity of A_1 relative to A_2 with increasing temperature; above 60°K, only A_1 remains and its energy shifts downward with increasing temperature, as shown in Fig. 25. Both bands B_1 and B_2 are prominent at very low temperatures, but with increasing temperature, B_2 decreases relative to B_1. The energy of the B_1 peak also decreases with increasing temperature up to 200°K, the maximum temperature at which it was detectable.

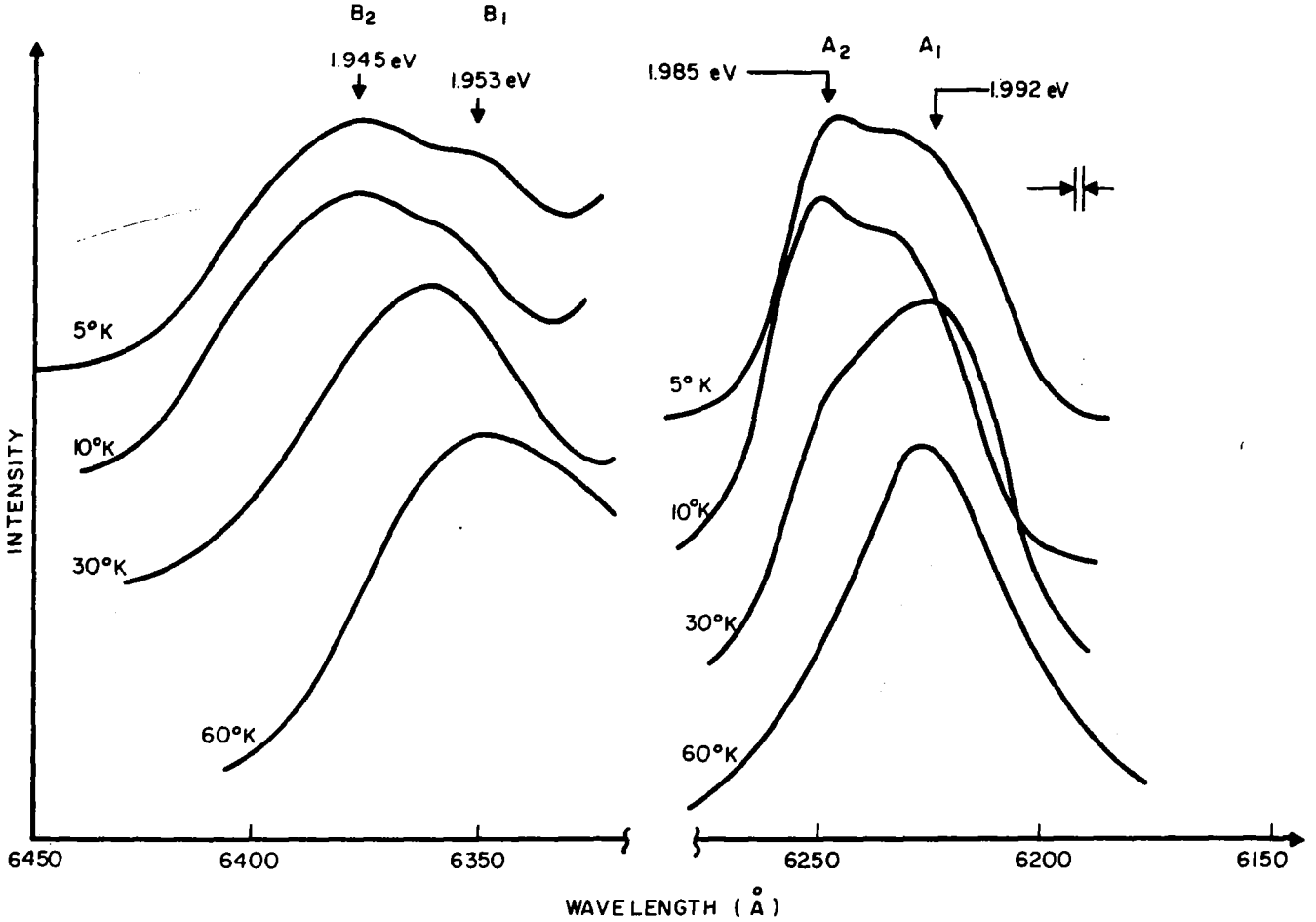

Figure 24. Photoluminescence spectra of an n-type, not deliberately doped epitaxial layer of $In_{.497}Ga_{503}P$ at 5, 10, 30, and 60°K showing the evolution of the four basic emission bands (sample #UN-1).

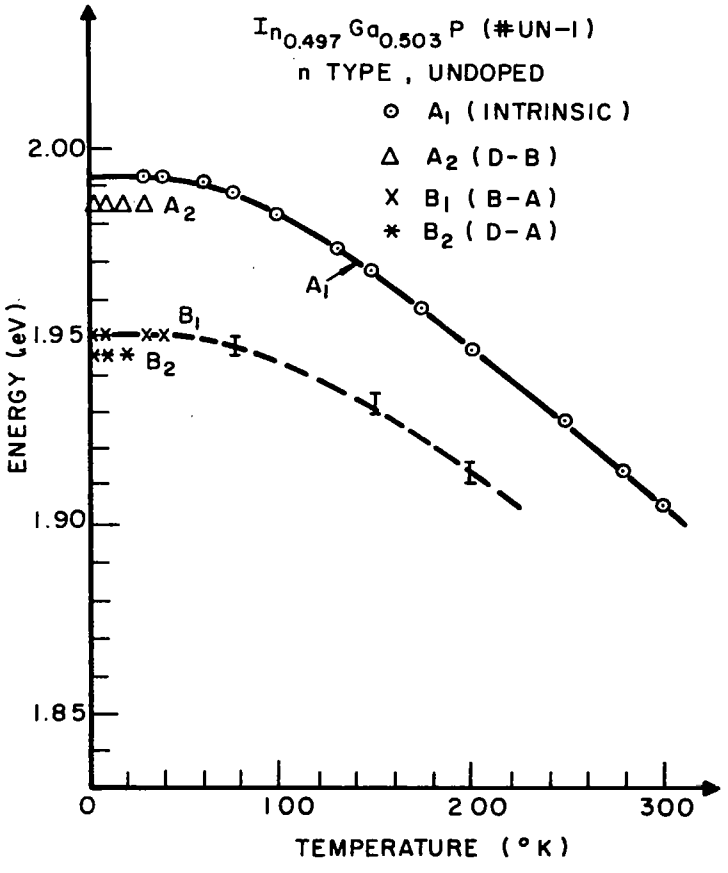

Figure 25. Variation of the peak positions of the various bands as a function of temperature for sample #UN-1 with spectra shown in Fig. 24.

Bands A_1 and A_2 could not be further subdivided to obtain the types of sharp lines previously seen, for example, in relatively pure, unstrained GaAs (ref. 27) and InP (refs. 28-30). Thus, the "fine" interpretation of the bands in terms of various possible bound excitonic processes is not possible. The most straightforward interpretation of the emission consistent with the data is as follows.

Consider first bands A_1 and A_2. Since it is known that at high temperatures the highest photoluminescence emission band in III-V compound

direct-bandgap materials is within a few meV of the bandgap energy, we interpret band A_1 as intrinsic recombination: free-carrier or free-exciton recombination, but possibly including excitons bound to neutral centers at very low temperatures. Above ∿100°K, free-carrier recombination is most probable. In any case, the shift of the peak position of A_1 is taken to be indicative of the shift of the bandgap energy with temperature. Above ∿100°K, we estimate $\Delta E_g/\Delta T = 3.7 \times 10^{-4}$ eV/K.

Band A_2, being displaced by 7 ± 1 meV from A_1, is believed to involve transitions between shallow donors and the valence band (D-B). This interpretation is based on a donor ionization energy E_D of 7 ± 1 meV, as in InP where $E_D = 7.65$ meV (ref. 31). Furthermore, previous $In_{1-x}Ga_xP$ data hint that the donor ionization energy remains invariant in the direct-bandgap compositional range (ref. 24). Thus, a value of $7 \pm .1$ meV for E_D in the present material is reasonable. The decrease in the intensity of band A_2 relative to A_1 with increasing temperature can then be readily explained by the decrease in the electron population of the shallow donors.

Turning to bands B_1 and B_2, the shift of the two bands with temperature is consistent with the assumption that band B_1 involves transitions from the conduction band to shallow acceptors (B-A), while band B_2, which is seen only at low temperatures where A_2 is also prominent, involves shallow donor-to-acceptor transitions (D-A). Neglecting the small Coulomb interaction energy term in this lightly doped sample, the peak separation between B_1 and B_2 should equal E_D, which is in fact the case. From the separation between the A_1 and B_2 peak energies, an approximate ionization energy of the unidentified acceptor of ∿ 40 meV is deduced.

We have also studied n-type samples deliberately doped with Se with $n \geq 10^{17}$ cm^{-3}. In these samples, it was not possible to resolve the near-bandgap emission into two bands as above. This is not surprising in view of the small donor ionization energy, since the donor levels will tend to merge with the conduction band tail states at these doping levels. The emission associated with residual acceptors was vanishingly low in the more heavily doped samples because of the more intense A_1 line, suggesting very little additional compensation by residual acceptors when the donor level is raised.

2. P-Type Materials: Cd-Doped. - Four Cd-doped samples ranging from $p = 1.8 \times 10^{16}$ cm^{-3} to 9.3×10^{17} cm^{-3} were studied (Table II). Unfortunately, more highly Cd-doped samples were not available due to temperature limitations of the auxiliary sidearm furnace of the vapor-growth system, and to the reduced incorporation of Cd into the $In_{1-x}Ga_xP$ (relative to Zn). Figure 26 shows the spectra of the four

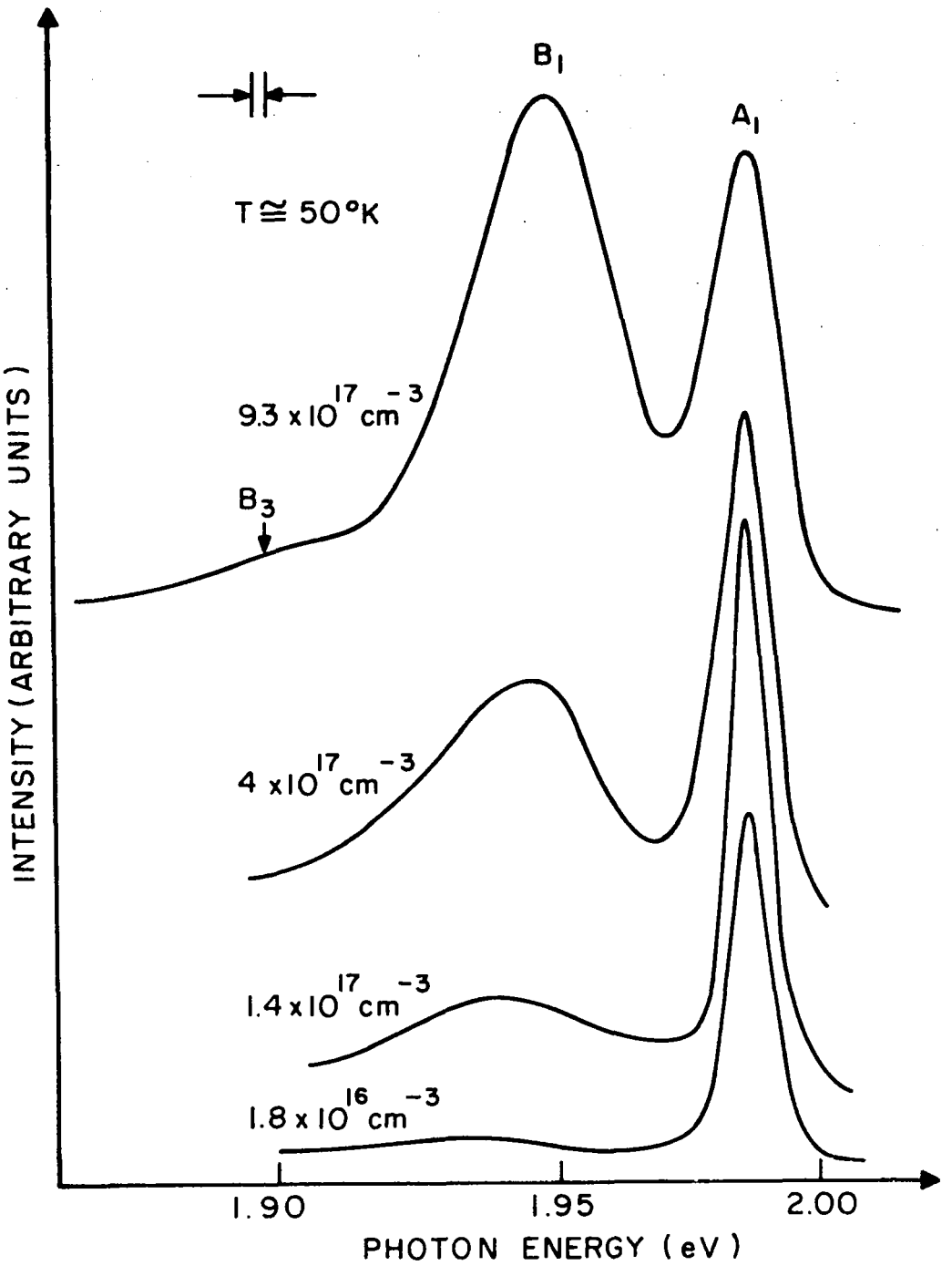

Figure 26. Photoluminescence of four Cd-doped samples at 50°K showing the relative increase of the B_1 band (B-A) involving the Cd acceptor. The peak position of A_1, which differs very slightly in the samples owing to small differences in the $In_{1-x}Ga_xP$ alloy composition, has been aligned to facilitate comparison.

samples at 50°K to emphasize the increase of the relative intensity of the B-A emission band B_1 with increasing Cd doping. (In Fig. 26, the peak position of A_1 was brought into coincidence to facilitate comparison.) In addition to B_1 and A_1, the only additional structure at 50°K is a small band denoted B_3, $\sim$50 meV below B_1, believed to be a phonon replica of B_1.

We now turn to a more detailed description of the emission spectra of Cd-doped material with the aid of sample #Cd-1 ($p = 9.3 \times 10^{17}$ cm^{-3}). As shown in Fig. 27(a), the two high-energy bands A_1 and A_2 are separated by 7 ± 1 meV, and these have been discussed above (Section III.A). The fact that recombination involving a *distinct* donor level is observed suggests that the residual donor concentration is small in these samples ($\lesssim 10^{16}$ cm^{-3}); otherwise, the donor levels would be significantly smeared. In #Cd-1, only band B_1 was prominent [see Fig. 27(b)], with the donor-acceptor band B_2 not being resolvable. However, in two more lightly doped samples (#Cd-3 and #Cd-4), a weak band B_2 was seen. The absence of B_2 is presumably due to the great imbalance between the density of the donors and acceptors in the heavily doped samples. Figure 28 shows the temperature dependence of the various emission bands in sample #Cd-1 between 4.2 and 300°K. Note that at room temperature the only emission is in the intrinsic A_1 band, with the Cd acceptors making no distinct contribution to the observed emission. The dominance of the A_1 peak at high temperatures for *both* n- and p-type $In_{.5}Ga_{.5}P$ (Figs. 25 and 28) is consistent with the fact that room-temperature photoluminescence peaks for n- and p-type $In_{1-x}Ga_xP$ have been found to have the same energy dependence on composition across the direct-bandgap portion of the alloy system (ref. 32).

Since it is well known that the impurity ionization energy is a function of the dopant concentration, it is of interest to analyze the photoluminescence data of the four Cd-doped samples to determine whether any significant variations can be found which correlate with the doping level. In the simplest analysis, the ionization energy can be deduced from low-temperature D-A recombination spectra or, at higher temperatures where the D-A emission is no longer observed, from the position of the B-A line.

From the peak energy, $h\nu_{B_2}$ of the donor-acceptor band, we find that

$$E_A = E_g - h\nu_{B_2} - E_D + q^2/\varepsilon r \qquad (10)$$

where E_g is the bandgap energy, q is the electronic charge, ε is the dielectric constant, and r is the average donor-acceptor spacing.

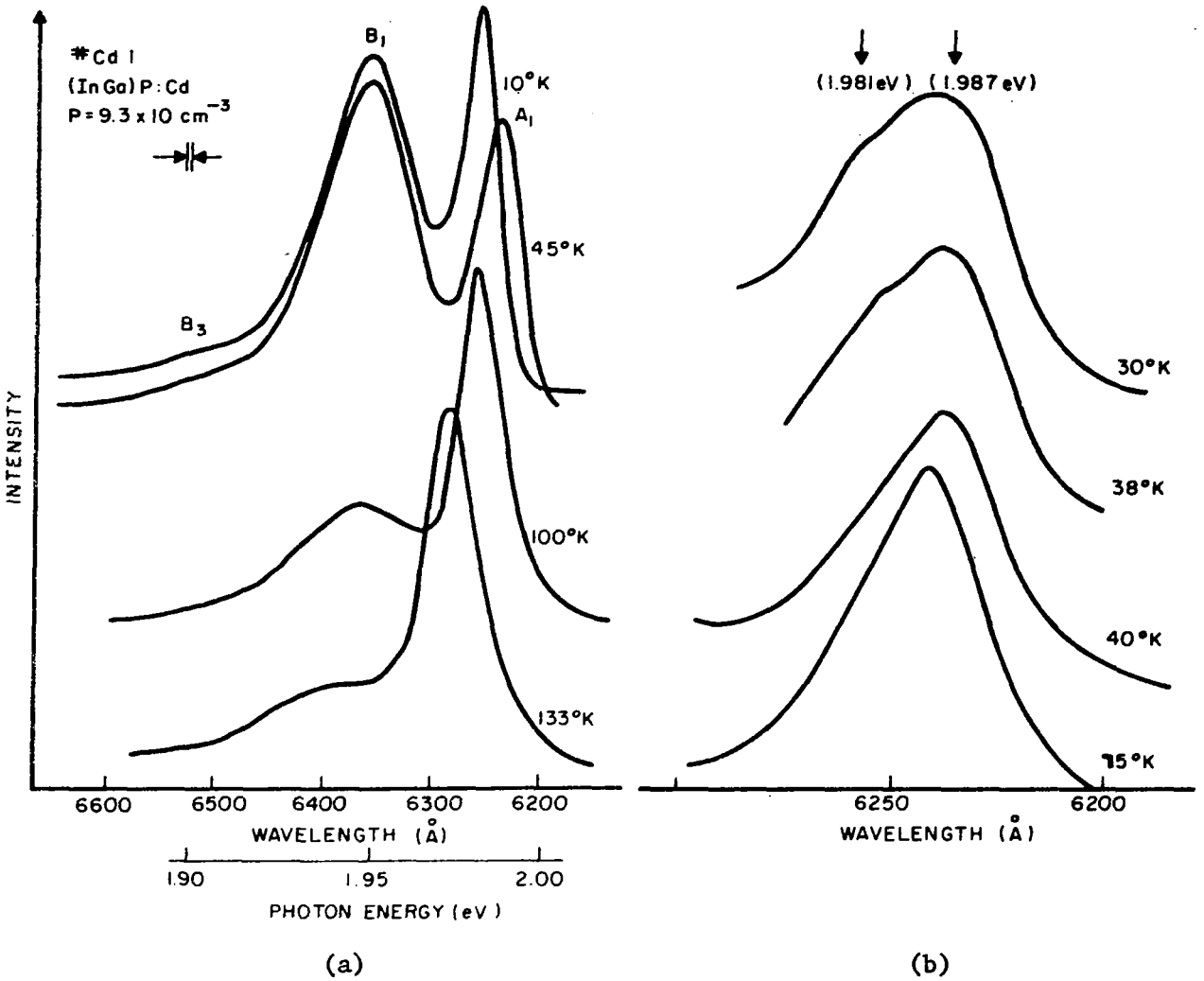

Figure 27. Photoluminescence of a Cd-doped sample with $p = 9.3 \times 10^{17}$ cm^{-3} at 10, 45, 100 and 133°K showing the gradual evolution of the various bands. At 10°K, band A_2 (D-B) dominates the near-bandgap emission, but at high temperatures the intrinsic band A_1 is dominant. Figure 27(b) shows the evolution of A_1 and A_2 between 30 and 75°K. Band B_3 is believed to be a phonon replica of Band B_1.

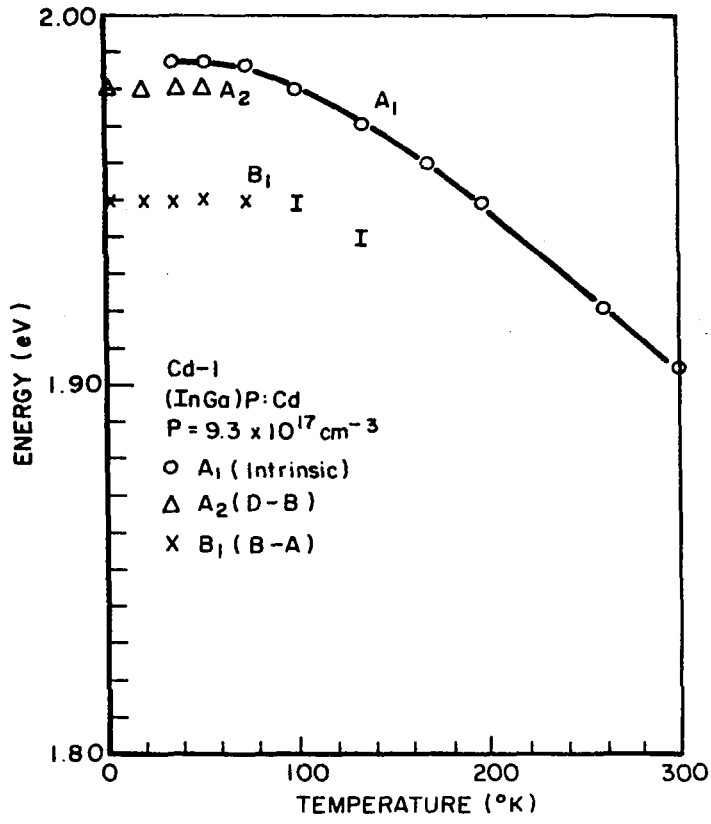

Figure 28. Temperature dependence of the various emission bands seen in sample Cd-1 ($p = 9.3 \times 10^{17} cm^{-3}$) between 4.2 and 300°K. Band B_1 is not resolvable above ~ 150°K. Thus, the room-temperature luminescence is basically intrinsic and does not involve the Cd acceptor levels.

Following our earlier discussions, we assume that the band A_2 peak energy $h\nu_{A_2} = (E_g - E_D)$ at 4.2°K; hence,

$$E_A = (h\nu_{A_2} - h\nu_{B_2}) + q^2/\epsilon r \qquad (11)$$

The value of E_A also can be estimated from the peak energy $h\nu_{B_1}$ of the B-A band B_1 using Eagles' equation (ref. 33),

$$E_A = E_g - h\nu_{B_1} + kT/2 \qquad (12)$$

The thermal energy correction term kT/2 is negligible at 4.2°K, but adds about 2 meV to $(E_g - h\nu_{B_1})$ at 50°K.

We show in Fig. 29 plots of the quantities $(h\nu_{A_2} - h\nu_{B_2})$ and $(h\nu_{A_1} - h\nu_{B_1})$ as a function of $p^{1/3}$ for the Cd-doped samples. Both quantities could be estimated for the most lightly doped samples, but for the two highest doped ones, only $(h\nu_{A_1} - h\nu_{B_1})$ could be determined. The data in Fig. 29 show a decrease in the effective ionization energy of the acceptor as the inter-impurity spacing is decreased. The extrapolated value of the ionization energy for very low doping is 57 meV + kT/2 = 59 meV, with an uncertainty of $\pm$ 2 meV. The data of Fig. 29 can be fitted with the approximate expression for the Cd ionization energy as a function of N_A-N_D:

$$E_A \cong E_A^o - 2 \times 10^{-8} (N_A - N_D)^{1/3} \quad \text{(in eV)} \tag{13}$$

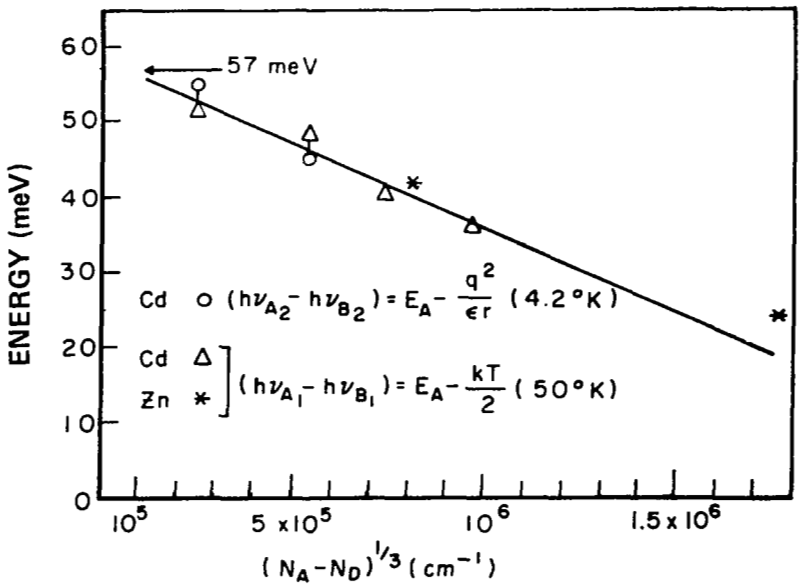

Figure 29. The quantities $(E_A - q^2/\epsilon r)$ determined at 4.2°K, and $(E_A - kT/2)$ determined at 50°K in four Cd-doped and two Zn-doped samples plotted as a function of the cube root of the hole concentration $(N_A-N_D)^{1/3}$, measured at 300°K. The extrapolated low doping energy value for the Cd acceptor is 57 $\pm$ 2 meV, or with the kT/2 correction, E_A = 59 $\pm$ 2 meV.

where E_A^o is 59 $\pm$ 2 meV. It should be emphasized that this analysis is predicated on the assumption that the peak energy of A_1 coincides with the bandgap energy. If A_1 is somewhat lower than the bandgap energy at 50°K, the ionization energy would be correspondingly larger (but by a value which should not exceed 3 to 5 meV). It is interesting to note that the above estimate of E_A(Cd) of 59 $\pm$ 2 meV is close to the value reported for InP (E_A = 56.1 $\pm$ 0.5 meV) at low temperatures (ref. 34), but is much lower than the GaP value of 97 meV (ref. 35).

3. P-Type Materials: Zn-Doped. - Figure 30 shows the 77°K emission spectrum of sample #Zn-1 (p = 5.4 x 10^{17} cm^{-3}). In addition to the high

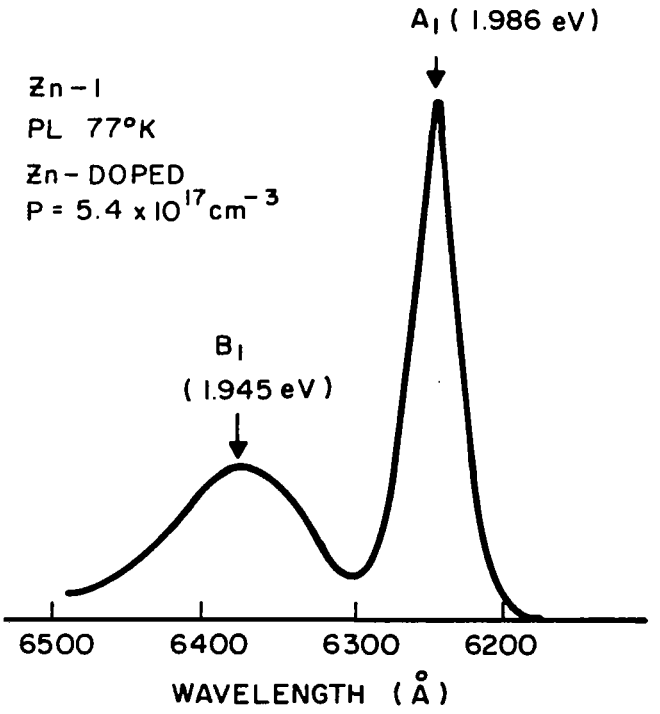

Figure 30. Photoluminescence at 77°K of Zn-doped sample #Zn-1 with p = 5.4 x $10^{17}$$cm^{-3}$ showing the two basic emission bands.

energy line in the vicinity of the bandgap energy, the B-A band B_1 involving the Zn acceptors is seen with no additional well-defined structure. From analysis of the 50°K data, $E_A(Zn) \approx 42 + \frac{kT}{2} \approx 44$ meV is deduced, which fits well into the E_A(Cd) data of Fig. 29.

The interesting effect of *high* Zn doping is illustrated by sample #Zn-2 with $p = 5.4 \times 10^{18}$ cm^{-3}. In contrast to the simple spectrum of #Zn-1, several new features are observed, as shown in Fig. 31(a). At 45°K, bands peaked at 1.968 eV and 1.92 eV are seen and also a broad band with tails off into the infrared. At 80°K, the broad infrared band is now well defined as a peak at ∿1.80 eV (∿0.19 eV below E_g), and the 1.92-eV emission is no longer resolved. The bandgap energy of the material is significantly above the highest energy band seen by low-intensity excitation photoluminescence. Cathodoluminescence measurements made at a nominal 77°K sample temperature indicate that the emission is strongly dependent on the excitation level in this particular sample. As shown in Fig. 31(b), the emission band centered at 1.971 eV under optical excitation (PL) shifts upward in energy with increasing electron beam excitation to a maximum peak at 1.992 eV, suggesting that the initial state for the radiative transition is inside the conduction band tail or that the final state is inside the valence band tail. At the same time the 1.80-eV band, while reduced in relative intensity, remains centered at the same peak energy.

The origin of the 1.992-eV band in Fig. 31(a) is uncertain. Since it is peaked 74 meV below the bandgap energy, it is improbable that it involves the *shallow Zn acceptor* level because such a large ionization energy does not appear reasonable. This leaves in question the contribution of the shallow acceptor to the emission spectrum. A plausible hypothesis is that the 45°K peak at 1.968 eV involves the shallow acceptor. This implies an approximate Zn ionization energy of $E_g - 1.968 + kT/2 \cong 1.994 - 1.968 + 0.002 \cong 28$ meV in this highly doped sample. This value is, in fact, quite consistent with the values obtained in similar Zn-doped samples on the basis of simple curve fitting of Hall data (ref. 20), and not unreasonable in view of the extrapolated curve in Fig. 29.

Finally, the ionization energy of Zn for sample #Zn-1 in Fig. 30 appears quite similar to that of Cd, although admittedly this conclusion is somewhat tentative and requires evaluation of further samples at very low Zn concentrations. Nonetheless, the extrapolated value of ∿59 meV for our Cd-doped samples is entirely consistent with a Zn ionization energy of 55 to 60 meV previously estimated from thermal ionization curves taken from Hall measurements of our Zn-doped $In_{.5}Ga_{.5}P$ (ref. 20), which yields approximate ionization energy values.

It is clear from the above discussion that new, relatively deep centers are formed at high Zn concentrations. It is relevant to note in Table II that the *radiative efficiency* at 300°K of sample #Zn-2 is very low with a rating (arbitrary units) of 11 compared with 335 for sample #Zn-1 with $p = 5.4 \times 10^{17}$ cm^{-3}. This observation and the above

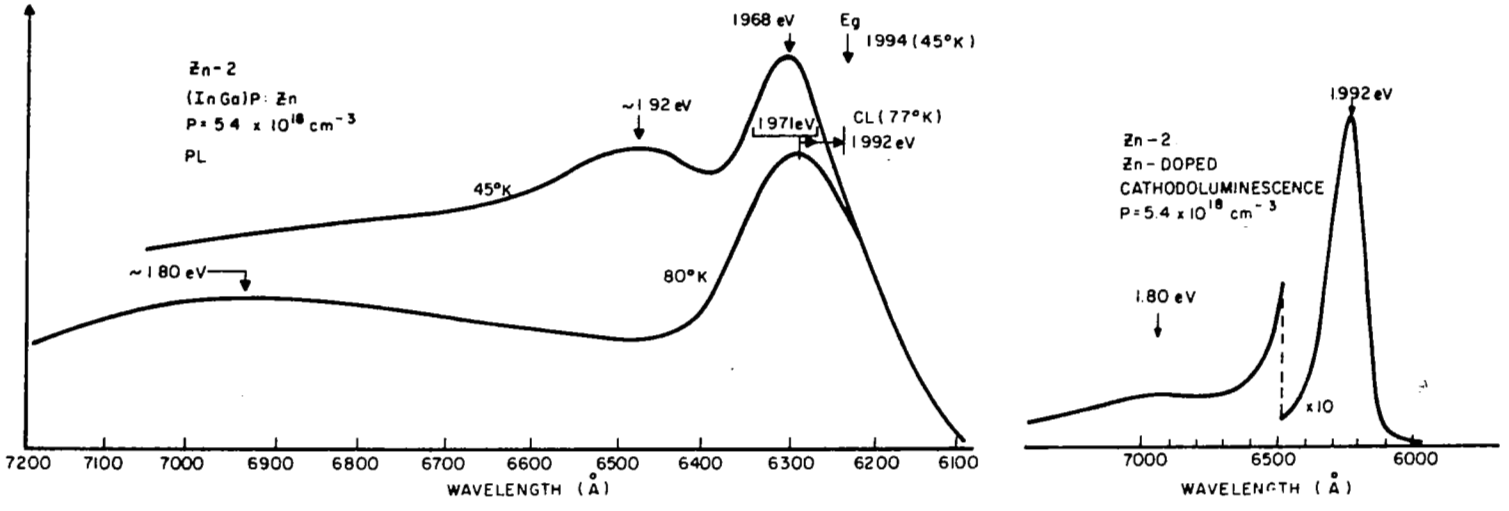

Figure 31. Emission spectra as determined by: (a) photoluminescence (low excitation level) and (b) cathodoluminescence (high excitation level) of the highly Zn-doped sample #Zn-2 ($p = 5.4 \times 10^{18}$ cm^{-3}.

spectral data suggest that the significant density of new centers, which form in the heavily doped p-type material, contributes to lowering the radiative efficiency. Furthermore, transmission electron microscopy studies have shown that precipitates of Zn_2P_3 are present in highly Zn-doped $In_{1-x}Ga_xP$ (ref. 32), which would be expected also to reduce the radiative efficiency, as is the case in GaAs (ref. 36). Thus, the "useful" solubility of Zn (and perhaps other acceptors as well) for luminescence purposes is clearly limited to values in the low 10^{18} cm^{-3} range (see Fig. 32), in sharp contrast to the case of GaAs, for example, where the radiative efficiency peaks at $\sim$ 1 to 3 x 10^{19} cm^{-3} (refs. 37, 38).

C. Electron-Beam-Excitation Studies of (InGa)P

The use of the electron beams to excite luminescence in semiconductors has several advantages over the usual photoluminescence techniques. These include:

1. The ability to obtain much higher excitation density using short low-duty-cycle pulses of electrons. Under these conditions the shortest wavelength emission occurs very near the band edge, thus giving a fairly accurate indication (+ 10 mV) of the bandgap (see Fig. 33).
2. Since the electron beam defines a spot about 50 μm in diameter, it is possible to observe moderate scale nonuniformities in composition. Furthermore, since beam penetration is small, emission is from a depth of only 1 to 2 μm.
3. Lasing can be observed under electron beam pumping if the samples are thin and shaped in the form of an optical cavity. Such lasing with bulk material requires no junction technology, but, nevertheless, indicates the lasing quality of the material itself in the area under the electron beam.

The cathodoluminescence results were obtained with a simple electron gun, producing electrons in the range of 5 to 25 keV focused to a maximum of 5 A/cm^2 and operating in a low-duty-cycle mode of 50-nsec-wide pulses at repetition rates up to 10 kHz. The samples were attached with silicon lubricant to a copper cold finger, which can be cooled to 77°K if desired. The luminescence was observed at 90° to the direction of the beam striking the sample, and the output is focused on the slit of a spectrometer. The spectra are recorded using a lock-in amplifier.

For observation of lasing the sample is normal to the electron beam and is in the form of a very thin (<10 μm) piece sandwiched between two aluminum layers which form an end-pumped Fabry-Perot cavity. The

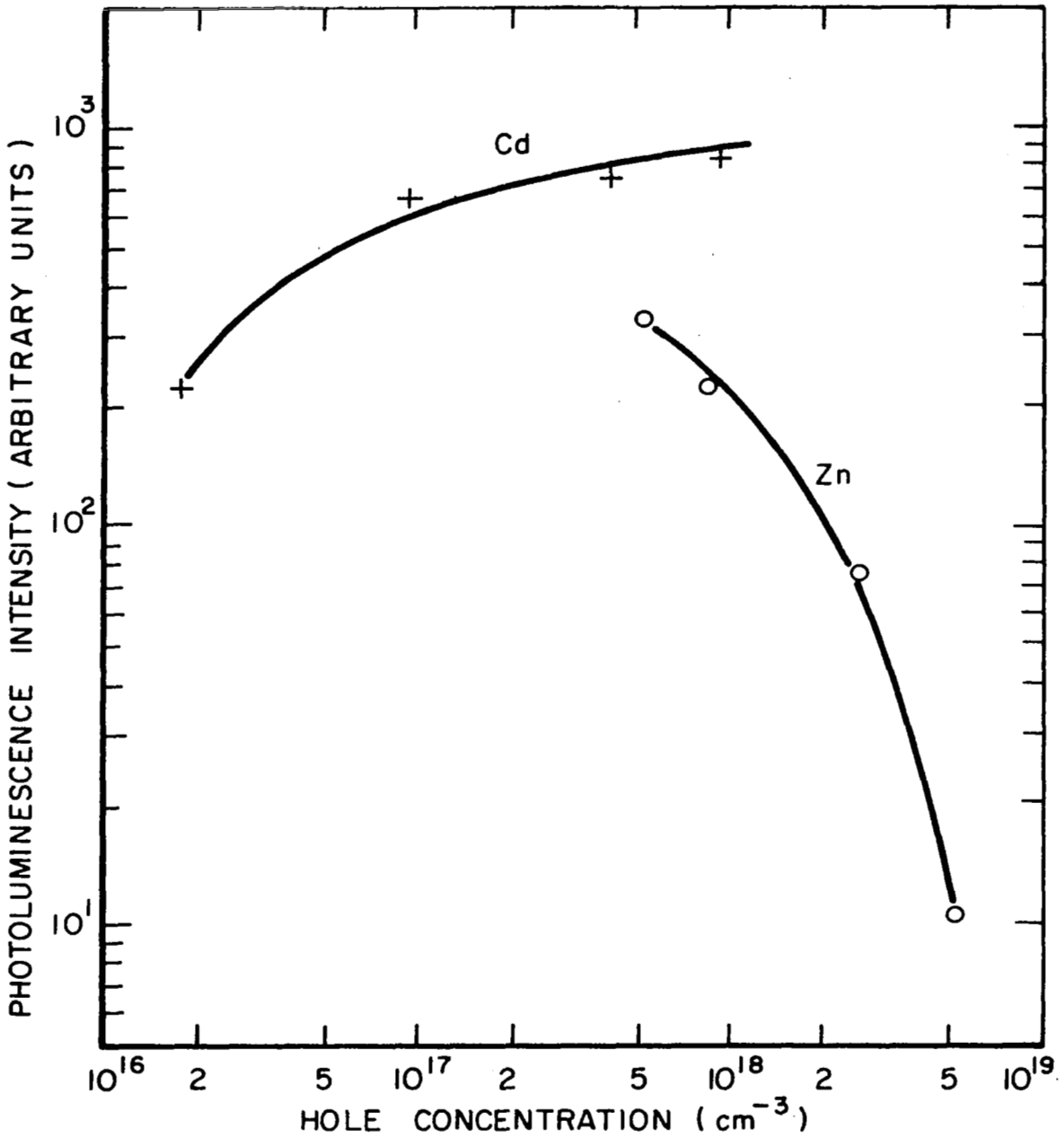

Figure 32. Relative photoluminescence intensity of bandgap peak A1 at room temperature versus the hole concentration (in cm^{-3}) for the Zn- and Cd-doped $In_{.5}Ga_{.5}P$ epitaxial layers discussed in this report. Hole concentrations were determined by standard Hall measurements (at 300°K).

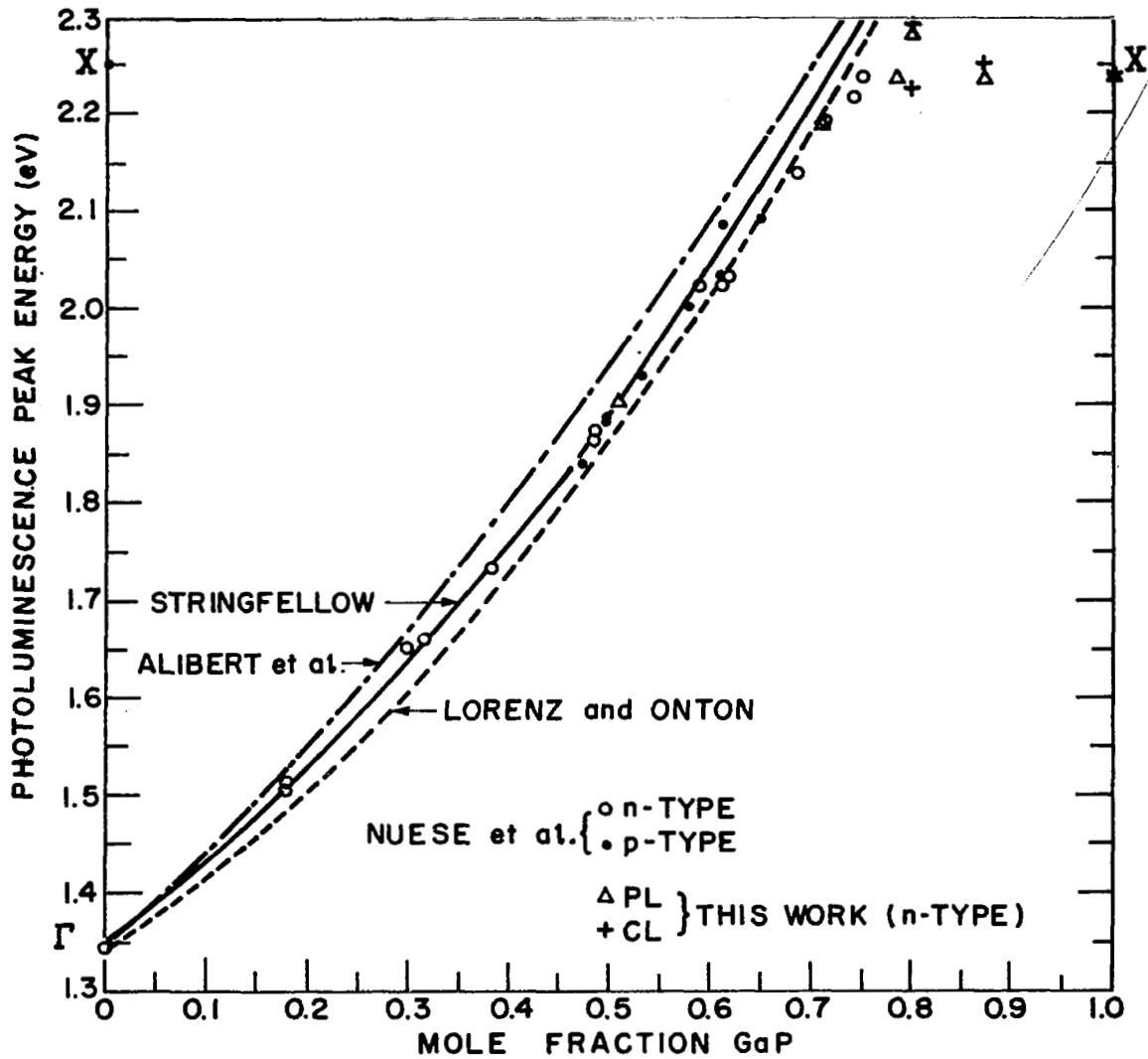

Figure 33. Variation of the bandgap energy in $In_{1-x}Ga_xP$ with x at 300°K as deduced from photoluminescence and cathodoluminescence data. The curve of Alibert et al. is deduced from electroreflectance measurements. The data are from references 32, 39, 40, and other recent work.

aluminum layer being struck by the electrons is 1000 Å thick, optically highly reflecting but quite permeable to electrons in the voltage range used. The other side of the sample rests on aluminum about 600 Å thick on a sapphire piece, allowing some light to pass through but reflecting more than 50% of the light.

End pumped lasing under electron beam excitation has been observed for a number of samples of (InGa)P of varying composition and doping. Lasing is indicated by the emission of a sharp spectral line on top of the near-bandgap emission peak. The narrow line is observed only above a sharp threshold and associated with it is a 10 to 30° conical laser beam emitted normal to the sample through the semitransparent aluminum. At the same time, since the emission is visible, an intense spot develops in the lasing area under the electron beam; this can be observed under a microscope.

Figure 34 shows the spectral emission curve from a sample of Zn-doped (2×10^{17} cm^{-3}) $In_{.42}Ga_{.58}P$ (grown in a boule) below and above lasing threshold. This occurred at 77°K for 15-keV electrons at a density of about 5 A/cm^2. The narrow lasing line is evident at 5820 Å (2.13 eV). This sample consisted of small grains. Lasing occurred

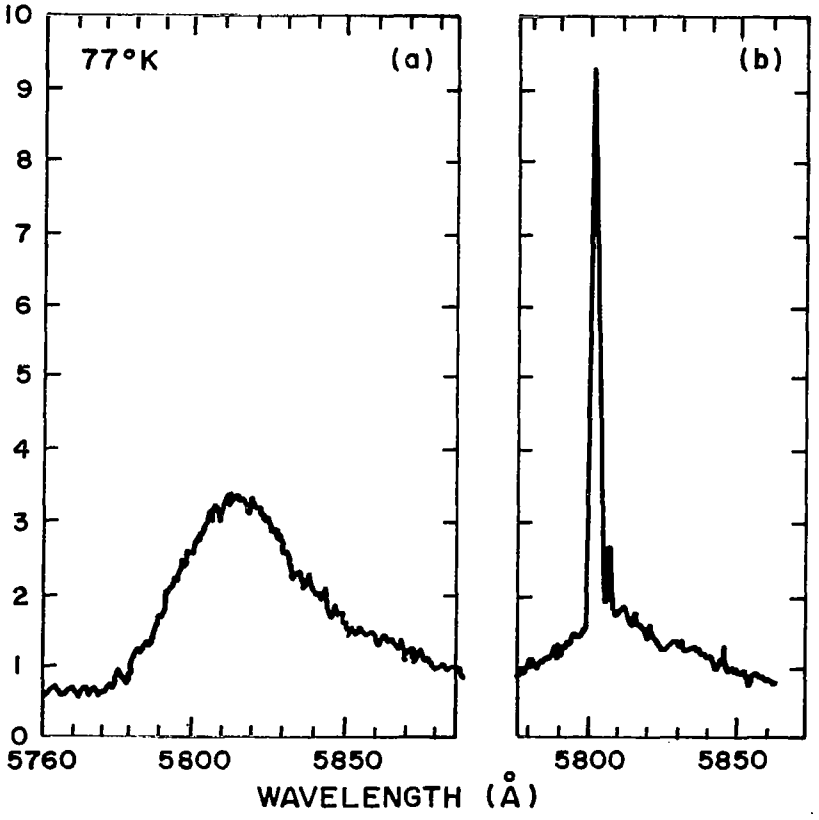

Figure 34. Cathodoluminescence below (a) and above (b) lasing threshold of a p-type sample of $In_{.42}Ga_{.58}P$ (boule-grown) at 77°K.

only in certain areas where the crystal quality was good. Vapor-grown $In_{.495}Ga_{.505}P$ samples doped with Cd lased under similar conditions at 6290 Å up to about 100°K but lasing at room temperature was not observed in any sample at the maximum available excitation density. In general, our results show that the lightly doped bulk material has high luminescent efficiency and is capable of lasing at thresholds comparable to or lower than that of bulk II-VI compounds under electron beam excitation. Unfortunately, material of this type is not suitable for laser diode fabrication because of the small grain size.

As mentioned earlier the electron beam can provide higher excitation density than is readily obtained by photoluminescence and therefore can show up near bandgap emission, which is present only after the long wavelength (deep level emission) is saturated. By controlling the intensity of the electron beam it is also possible to observe the long wavelength emission.

To test for the effect of strains and variation across the epitaxial layers, we have studied (InGa)P grown on a GaAs substrate, first with the layer on the substrate and later with the substrate removed. These observations have shown significant spectral differences which are not understood but which are presented here because of their possible significance in terms of nonuniformity in the layers and possible effects of strain resulting from growth on the GaAs substrate.

Figure 35 shows representative cathodoluminescent spectra of an $In_{.5}Ga_{.5}P$ sample lightly doped with Cd and compensated by residual donors. The layer, about 10 μm thick, was grown on Cr-doped GaAs by vapor deposition. The spectra in Fig. 35(b) were obtained with the epitaxial layer on the GaAs substrate. These show single peaks at 6230 Å for 77°K and 6480 Å for 300°K, and are consistent with photoluminescent spectra. Figure 35(a) shows spectra for the same epitaxial layer after it was removed from the substrate by chemically dissolving the substrate. The current density of excitation has been chosen here to show the two peaks most clearly since their relative height is a function of excitation density. Several features of the spectra should be noted. The position of the two peaks shifts to longer wavelength as the temperature is raised and their width increases. Furthermore, the peak separation increases with temperature. On comparing the spectra for the epitaxial layer on the substrate with those for the epitaxial layer alone it is seen that the emission wavelength for the former is about 50 Å shorter at 77°K and about 80 Å shorter at 300°K. This difference cannot be due to beam heating since the substrate makes better thermal contact to the cold finger than the epitaxial layer alone. At the highest current-density excitation the long wavelength peak of the emission predominates with almost complete loss of the short wavelength

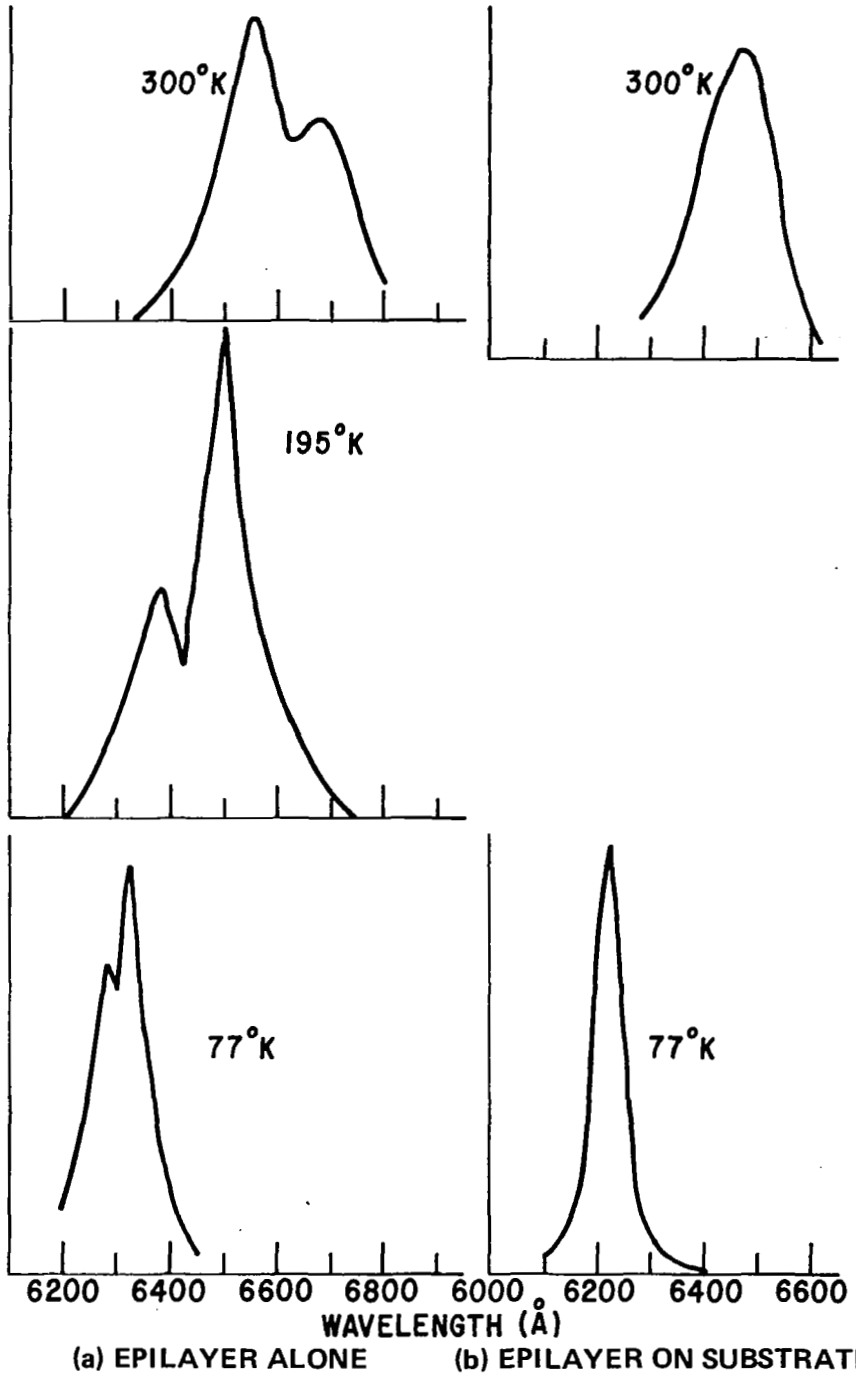

Figure 35. Cathodoluminescence of epitaxial layer of (InGa)P at various temperatures after (a) and before (b) removal from the GaAs substrate on which it was grown by vapor-phase epitaxy.

peak. Therefore, at these levels of excitation the difference between the peak emission of the layer on or off the substrate is as much as 90 Å at 77°K and 200 Å at 300°K. As a check on our cathodoluminescence results, this same epitaxial layer, removed from its substrate, was excited by photoluminescence at 77°K. This showed a main peak corresponding to the short wavelength peak on the left of Fig. 35 for 77°K. The longer wavelength peak now shows up as a weak shoulder, which is present only when the epitaxial layer is removed from the substrate. This shoulder would no doubt be more pronounced if higher density photoexcitation could be used.

Cathodoluminescence of the two different sides of the epitaxial layer (substrate removed) may well be different because the electron does not penetrate more than 1 to 2 μm into the 10-μm layer. A number of spectra were recorded on another sample of (InGa)P to compare the emission from the grown side and the interface side. While the excitation levels are not accurate the comparison is made with side-by-side samples, the beam being moved from one to the other with no change whatever in excitation density. This new sample was p-type Cd-doped (1.8×10^{16} cm^{-3}) $In_{1-x}Ga_xP$ ($x \cong 0.5$). The cathodoluminescent emission at 77°K for the epitaxial layer on the substrate peaks at 6240 Å while the main photoluminescence peak was at 6265 Å, with a small peak at 6425 Å. Figure 36 shows the spectra from the grown side of the layer on the left, and, for the same current density, the spectra from the interface side on the right. On the grown side of the removed epitaxial layer the emission peak at 6270 Å is at a longer wavelength than either the cathodoluminescence or photoluminescence peak for the layer on the substrate. At 2 A/cm^2 a peak at 6480 Å is seen which, however, would seem to be from a different source than the 6425-Å photoluminescence peak, which occurs at an excitation density orders of magnitude lower.

If we turn to the cathodoluminescence from the interface side of the (InGa)P layer, the spectra are shown on the right of Fig. 35. The main peak is at 6300 Å, which is at a considerably longer wavelength than the emission from the grown side of the layer. The other important feature is the peak at 6520 Å which is only about 70 Å wide and persists from low current density to the highest used.

The largest effect observed here is the occurrence of rather narrow double emission peaks when the epitaxial layer is removed from the substrate. The presence of the longer peak has been confirmed in photoluminescence although it is weak. Transmission measurements of the sample over the wavelength range from 6100 Å to 6800 Å show no changes of slope corresponding to the two peaks, but it is possible that such changes in slope cannot be resolved.

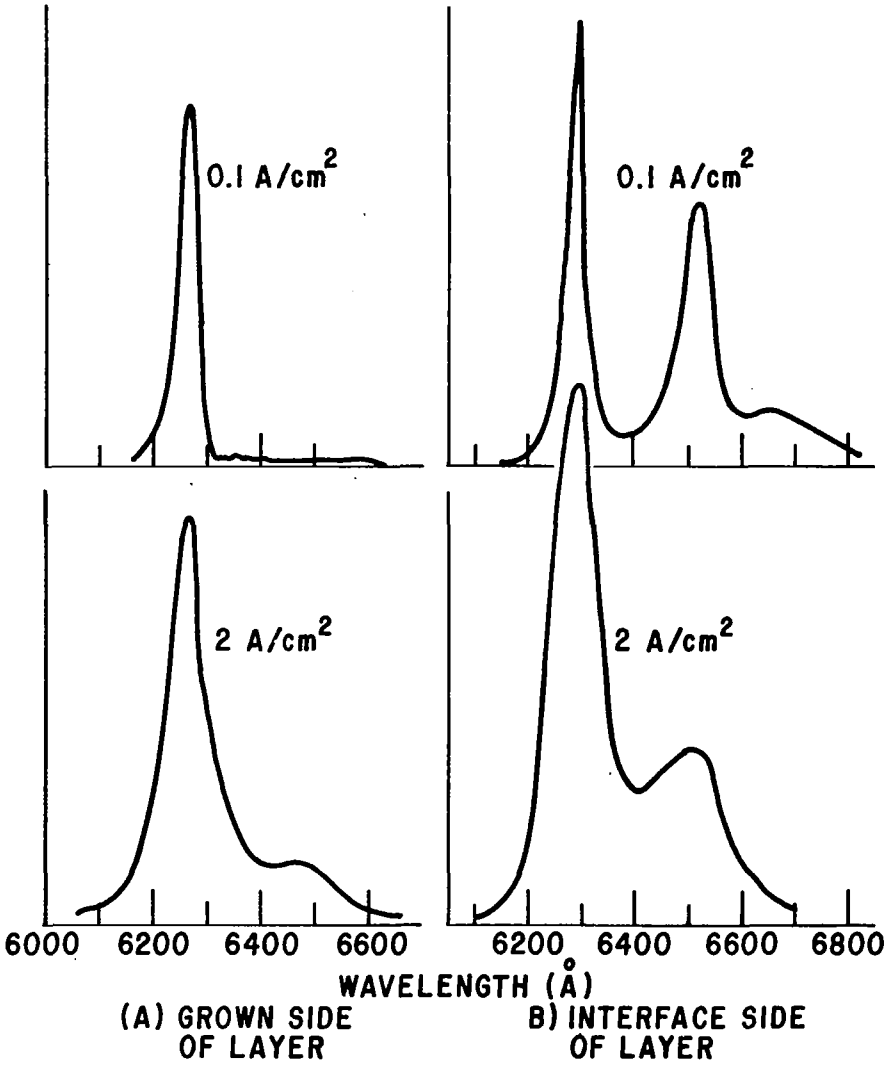

Figure 36. Comparison of the cathodoluminescence from the surface and the GaAs-(InGa)P interface of a sample epitaxially grown from the vapor on a GaAs substrate.

In general, the two emission peaks are of comparable width, $\approx$ 50 Å. While this width is reasonable for the near bandgap emission it is much too narrow for the second peak to be due to doping or impurities. Furthermore, at room temperature, a spectrum having two narrow peaks is unusual in direct-bandgap semiconductor luminescence; rather the spectrum consists of a broad single peak. The narrowness of the second peak seems

to suggest that the epitaxial layer studied is inhomogeneous in composition and that, in fact, the material has predominantly two compositions, with bandgaps corresponding to the two narrow peaks. The relative amounts of the two materials seem to vary with depth in the grown layer, there being more of the material with smaller bandgap on the interface side. In other words, there is a tendency for the material to become more and more single composition as it grows. The compositional variation, if this is the explanation, must occur uniformly in the plane of the layer since moving the 100-μm electron spot around on either the grown or interface surface produces little change in the spectra.

No complete explanation exists for the increase in wavelength of the bandgap peak on going from excitation of the grown side of the layer attached to the substrate to the grown side of the layer with the substrate removed, and finally to the interface side of the layer. In some way the wavelength increase may be due to change in absorption of the emitted light as it is reflected back and forth between the surfaces of the layer. In the case of the layer on the GaAs substrate, emitted light striking the interface region is largely absorbed in the GaAs. Although there is known to be strain in the epitaxial layer which is relieved when the substrate is removed, the magnitude of the observed spectral change is too large to be accounted for in this way.

The compositional inhomogeneities that seem to be indicated by these observations with the electron beam may be a problem of particular importance in injection layers where both a good diode behavior and a good optical cavity are essential for low threshold lasers, especially at room temperature. Experiments designed to study the effects of substrate removal on diode lasers are discussed in a later section.

D. Junction Properties

The $In_{1-x}Ga_xP$ p-n junctions prepared by VPE frequently have deep recombination centers which can be detected both by the radiative emission at low current densities and by photocurrent measurements. To study the diodes with a minimum of distortion of the emitted radiation, we prepared surface-emitting p-n junctions with an ohmic contact covering only a small portion of the diode surface. The photocurrent measurements were made on unbiased p-n junctions. Figure 37 shows the photocurrent and electroluminescent spectra of a Zn-doped diode ($x \gtrsim 0.5$) grown by VPE on a GaAs substrate. The wide emission band seen at low currents is related to the increased absorption below the bandgap energy. The peak of the emission at ∿7330 Å is approximately 0.23 eV below the bandgap at 77°K. Comparison of this band with that seen in the photoluminescence of heavily Zn-doped material [∿0.19 eV below the bandgap energy (Fig. 31)] does not clarify whether the two have the same origin.

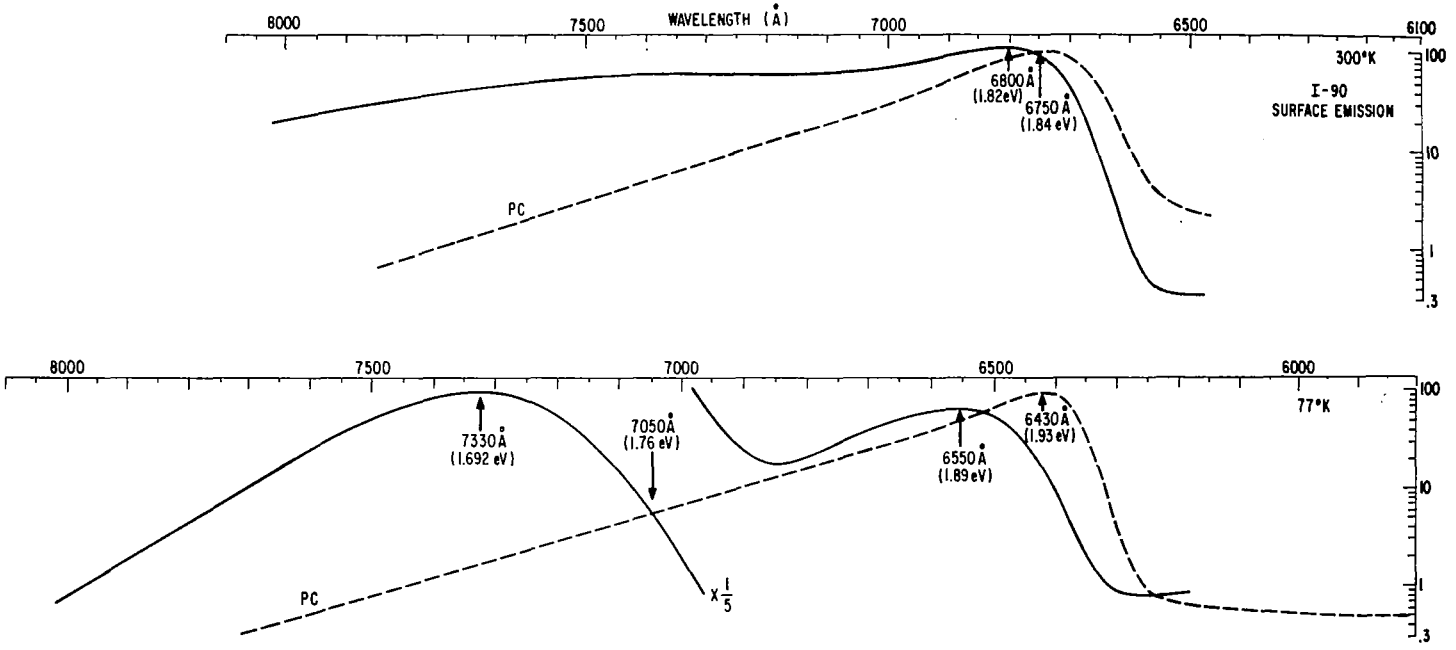

Figure 37. Electroluminescence and photocurrent (PC) of an $In_{1-x}Ga_xP$ diode at room temperature and 77°K showing the presence of deep levels. The material was grown by vapor-phase epitaxy on a GaAs substrate. The p-region was Zn-doped ($\sim 5 \times 10^{18} cm^{-3}$) and the n-region was Se-doped ($\sim 10^{18} cm^{-3}$).

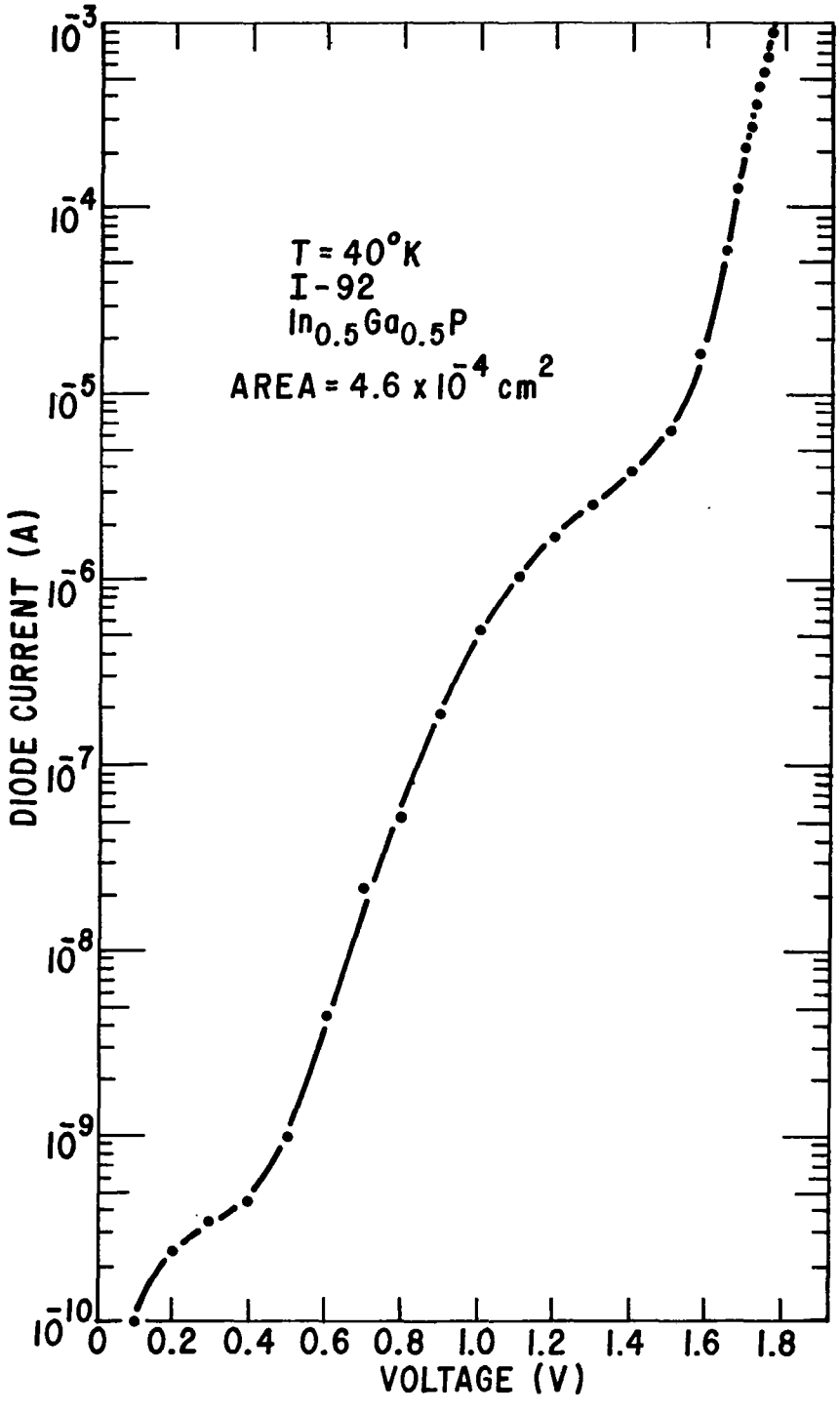

Figure 38. Forward I-V characteristic for a Zn-doped $In_{.5}Ga_{.5}P$ sample at 40°K showing typical tunnelling structure due to defects.

It is possible that the process of Zn diffusion into the heavily n-type material gives rise to other deep levels.

The presence of deep levels is also reflected in the I-V characteristics that indicate impurity-assisted tunneling in these junctions, but to a degree that varies from wafer to wafer. Figure 38 shows a typical I-V characteristic in the forward direction at 40°K with well-defined inflection points at 0.4 and 1.5 eV. Further study is needed to determine the relationship between these data and the deep levels discussed earlier.

E. Laser Properties

Homojunction, single heterojunction, and double heterojunction laser structures were prepared by VPE. The only structures which consistently lased were homojunctions in which the p-side of the junction was doped with Zn. (Cadmium-doped diodes did not lase.) During growth a narrow (∿ 1-2 μm) compensated region (see Fig. 39) was formed by allowing both the n- and p-type dopants to flow in the reaction at the same time. In some cases Zn was diffused *after* the epitaxial growth to further extend the diffused "overlap" region, but with no significant impact on the laser properties.

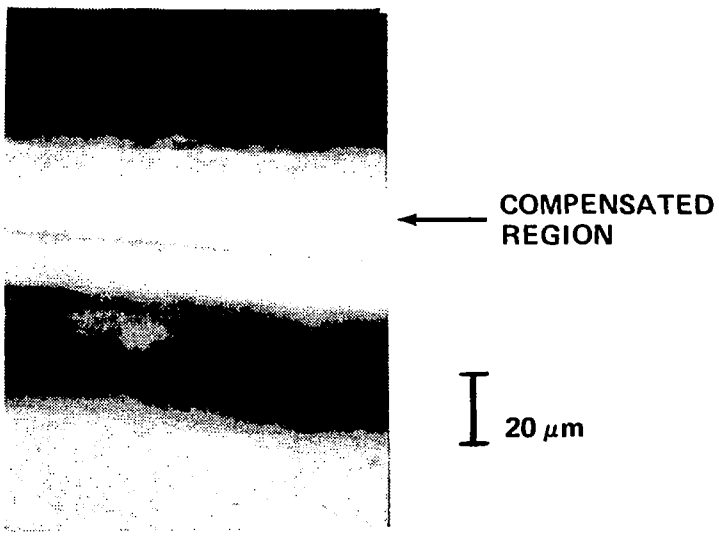

Figure 39. Cross section of (InGa)P homojunction grown on a GaAs substrate. The narrow dark region is the p-type compensated recombination region.

Extensive work was done with $In_{.5}Ga_{.5}P$ diode grown on GaAs substrates to study the best possible materials conditions. The lowest threshold current density seen was ∿30,000 A/cm^2 at 77°K, with a very steep increase in threshold with temperature which precluded lasing significantly above that temperature. The differential quantum efficiency was only on the order of a few percent. Figure 40 shows a typical laser emission spectrum near threshold of a unit emitting at ∿6400 Å.

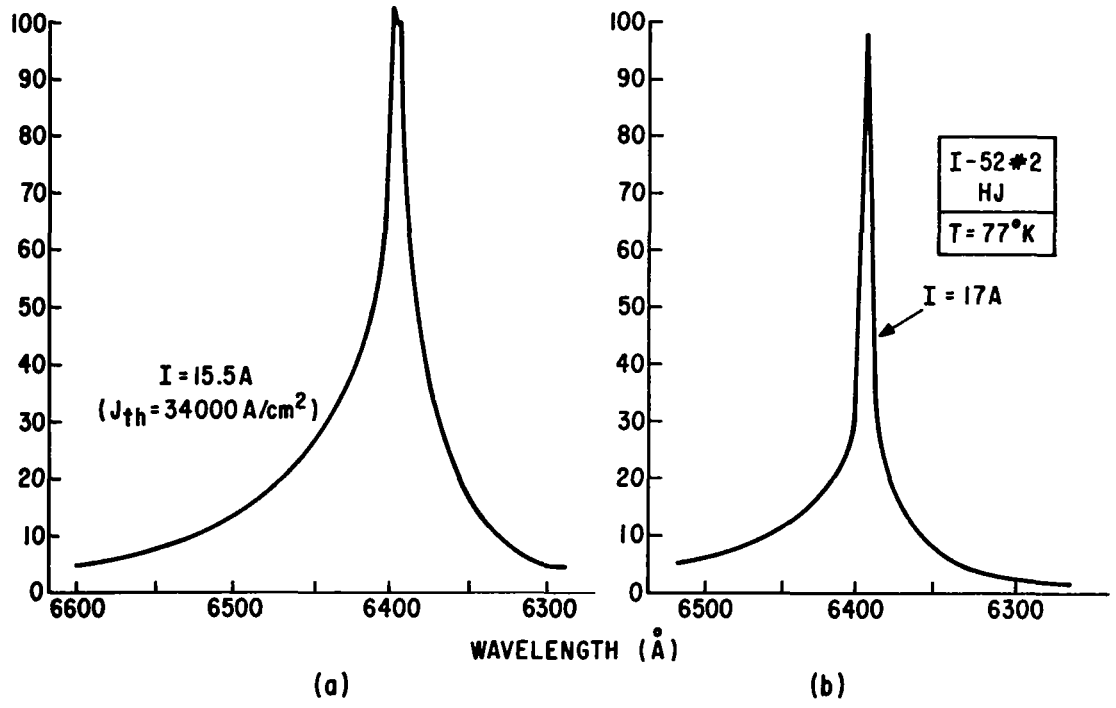

Figure 40. Lasing spectra at two current levels of a (InGa)P diode grown on a GaAs substrate (77°K).

To extend the lasing wavelength toward the green, diodes were also grown on GaP substrates (ref. 42) and graded to a composition of $In_{.4}Ga_{.6}P$ near the surface. We obtained lasing at 77°K at a wavelength as short as 5980 Å, which is the lowest semiconductor laser diode wavelength ever achieved. The threshold current density, however, was too high (70,000 A/cm^2) for sustained operation.

A variety of heterojunction structures were grown in an attempt to improve the performance of these lasers. None of the single, double, or LOC types of heterojunctions gave any indication of improved characteristics over those obtainable with homojunctions, despite the fact that the heterojunction barrier height was kept at a minimum (about 0.1 eV) to minimize the lattice defect introduction. In fact, double heterojunction units did not lase at all, while single heterojunction devices rarely lased.

A detailed study of the effect of the heterojunction in laser properties was made as follows: On a standard p-type GaAs substrate, a matched composition ($In_{.5}Ga_{.5}P$) p-layer was grown first, followed by a compensated layer and then an n-type layer. This program was maintained in every case, but at some particular time during the run, the temperature of the substrate was dropped about 23°C, which has the effect of changing the composition grown to $In_{.52}Ga_{.48}P$, i.e., to smaller E_g. Thus, a heterojunction (HJ) is introduced into the layer at a position relative to the p-n junction dependent on the degree of compensation, the diffusion of zinc during the run, and possibly various other factors. The exact position of the heterojunction was inferred from photomicrographs of etched cross sections and electron microprobe analyses.

TABLE III

Properties of Heterojunction Lasers

Sample	EL (Å)	Position of Heterojunction	Relative Output	$V_{breakdown}$ (V)
103	6690	p-side, 3.0 μm before	1.5	10, gradual
104	6620	p-side, 3.5 μm before	1	9, gradual
105	6570	n-side, 3.5 μm after	6.9	14, abrupt

As shown in Table III, the EL emission is longer in samples 103 and 104 because the HJ was introduced before the p-n junction, so that E_g was reduced. In sample 105, however, the emission is shorter, since the HJ was introduced after the junction. The most significant finding is that the junction is degraded in the two cases where it follows the heterojunction. This is almost certainly caused by the introduction of new misfit dislocations which propagate through the junctions. In sample 105, these dislocations only occur after the junction so that

they cannot have a direct influence on the junction. Thus, any attempt at introducing a double HJ in this way must fail. A single HJ after the p-n junction may help, at least as far as these data are concerned.

We have therefore introduced a HJ after the p-n junction, with the required increase in bandgap. The resultant material, I-92, was thoroughly analyzed. It was found to be an inefficient laser compared with another sample, I-90, which was designed to be identical to I-92, except that the HJ was omitted. That is, the threshold was reduced and the device resistance increased. The increased resistance may be associated with the generation of misfit dislocations, and the increased threshold could be due to long-range effects of the grading, such as stress. Of course, we cannot entirely eliminate the possibility of other factors having changed, such as doping in the higher bandgap region.

The thresholds and efficiencies obtained with (InGa)P diodes are inferior to those obtained with GaAs or (AlGa)As devices (see Section III). We believe that the much larger defect density in the highly doped epitaxial (InGa)P is basically at fault. It is not simple to determine the relative contributions to the poor laser performance due to excessive internal absorption [high α in Eq. (7)], low internal quantum efficiency η_i or inadequate waveguiding, Γ. An idea of the waveguiding properties can be obtained by measurement of the far-field radiation pattern in the direction perpendicular to the junction plane. Such a measurement yielded a half-power beam divergence of about 17°, a value typical of homojunction laser diodes in GaAs. (The indicated optical source size is about 2 μm.) The fact that J_{th} for the present laser diodes is 15 to 30 times higher than in comparably doped GaAs homojunction diodes at 77°K cannot therefore be attributed to large differences in the extension of optical field outside the recombination region. The more probable causes are believed associated with slightly irregular junctions which increase the light scattering, and high internal absorption at defect centers introduced by the high dopant density. The nonplanar junctions are due to enhanced diffusion in dislocated or unusually strained regions. In addition, the internal quantum efficiency in these diodes appears to be lower than in GaAs. In fact, comparable measurement of the spontaneous efficiency (although much affected by diode geometry) does indicate significantly (by factors of 3 to 5) lower quantum efficiency than in a typical diffused GaAs diode at 77°K with similar geometry.

It is of particular interest to recall, however, that the lasing seen in lightly doped samples using electron-beam excitation indicates that no significant differences exist in the pump power needed to obtain lasing. This suggests that inherently the material is efficient, but that the introduction of the high dopant density is a basic source of difficulty in obtaining efficient lasers.

Another important factor is the effect of strain which enters due to the substrate layer mismatch. Removal of the substrate was found to produce significant effects on electron-beam-pumped lasers. Related effects were also observed in the case of incoherent diodes. Laser diodes were fabricated from the same wafer both with the (InGa)P layers on the substrate and after the substrate was removed. It was found that removal of the substrate shifted the emission toward larger wavelengths, with a double peak (Fig. 41); a smaller peak, corresponding to the on-substrate emission, is also seen. Most important, the threshold current density was reduced by a factor of 2.7. There is little doubt that these effects are connected with the relief of stress induced by the substrate mismatch. (The qualitative aspects of this work are consistent with the results reported in Section VI.)

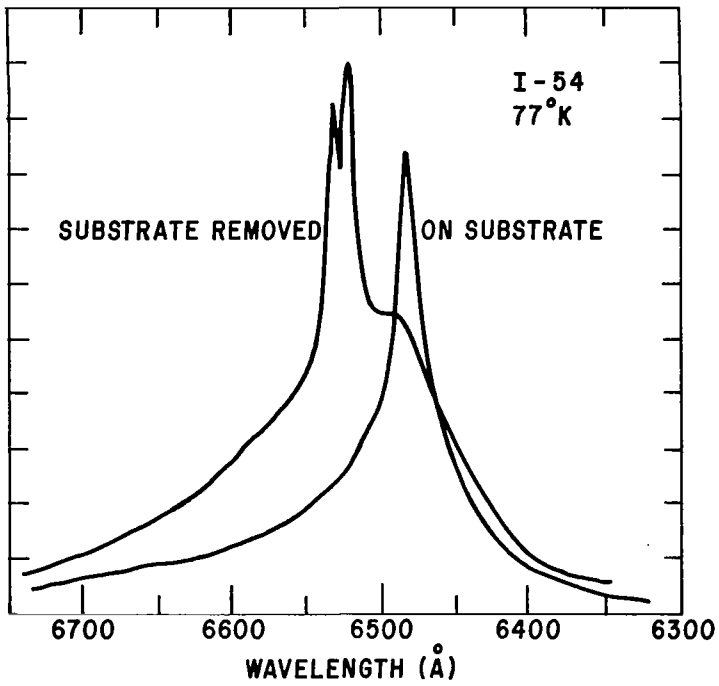

Figure 41. Lasing spectra of VPE (InGa)P with the GaAs substrate and after the substrate has been removed.

That this stress is significant can be appreciated from the fact that the GaAs-$In_{.5}Ga_{.5}P$ lattices were matched at 700°C where the material was grown, whereas the diodes are operated at 77°K, which is far removed from the matching temperature.

These results suggest that the GaAs substrate cannot be used as part of the device, but that it must be removed for optimum operation, although the effects should be less severe for operation at room temperature.

Finally, a source of difficulty with (InGa)P not present with (AlGa)As diodes is the fact that, because of the greater acceptor ionization energy in (InGa)P in the region of interest for visible lasers, significant carrier freeze-out occurs at low temperatures. This increases the diode resistance and hence results in lower power conversion efficiency.

F. Properties of (InGa)P Prepared by Liquid-Phase Epitaxy

1. Growth of Epitaxial Layers. - Simultaneously with the growth and study of VPE material, we have studied growth of (InGa)P using LPE. For reasons discussed elsewhere in this report, we have used one type of substrate exclusively, i.e., GaAs with the (111)B surface. Thus, the composition of the melt has to be adjusted to produce an alloy near $x = 0.5$ which most closely matches the substrate. Our basic objective has been to grow layers onto GaAs which would compare favorably with VPE layers as regards x-ray topography and photoluminescence. The reason for this approach was that previous work at RCA Laboratories has shown that (InGa)P layers and p-n junctions grown by LPE were poor in quality, the material grossly disturbed, and the electroluminescence efficiency very low. In contrast, VPE junctions were planar, the material was of excellent structure, and the EL highly efficient. Thus, it was clear that unless such material and junctions could be grown, LPE junctions in InGaP could not possibly yield laser material.

Based on this work and a study of the literature, two approaches were defined. In the first, a standard LPE process was used, involving the slow cooling of a melt resting on the substrate, and in the second, a melt is subjected to a thermal gradient while in contact with the substrate and a source wafer, so that the gradient provides the driving force for the deposition and the material is grown at a constant temperature. In what follows we discuss the results obtained with these and other methods, using a variety of systems.

A table of melt compositions was calculated from published data (ref. 43) and used to provide the starting point for the experimental optimization of the layers. For most of the runs, weighed amounts of In and InP were heated to the growth temperature and cooled. During the run, a GaP platelet was exposed to this solution, at the growth temperature, to saturate the melt with the amount of gallium and phosphorus called for by the system. In some runs, In and Ga were homogenized,

and InP was used to saturate the solution before and during the growth. Figure 42 is a photomicrograph of a cleaved cross section through the layer, showing typical structures obtained. In general, the surface of

Figure 42. Photomicrograph of cleaved edge of wafer, showing the (InGa)P layer on the GaAs substrate.

the layer shows evidence of degradation and decomposition, because of the phosphorus loss. This was established in a direct experiment, by heating an LPE layer of InGaP for one minute at 800°C in forming gas. The surface layer changed during this treatment, showing cracks and flaws which were not present before. Thus, it is clear that 800°C is a high temperature as far as material stability is concerned. With suitable changes in the melt, layers were grown at 700°C. Figure 43 compares a surface photograph of such a layer with one grown at 800°C. The improved surface shows that the decomposition problem has been reduced by the drop in temperature. However, other problems, such as depletion, are expected to be serious at 700°C.

Another approach to the problem of decomposition is to stabilize the atmosphere above the melt using phosphine, PH_3. This approach has been tried using a H_2-10% PH_3 gas mixture. There is no question that the melt decomposition can be stopped this way. Actually, when PH_3 is passed over In held at 800°C, InP is synthesized. Thus, the problem in using PH_3 is not so much to prevent the decomposition of (InGa)P but to

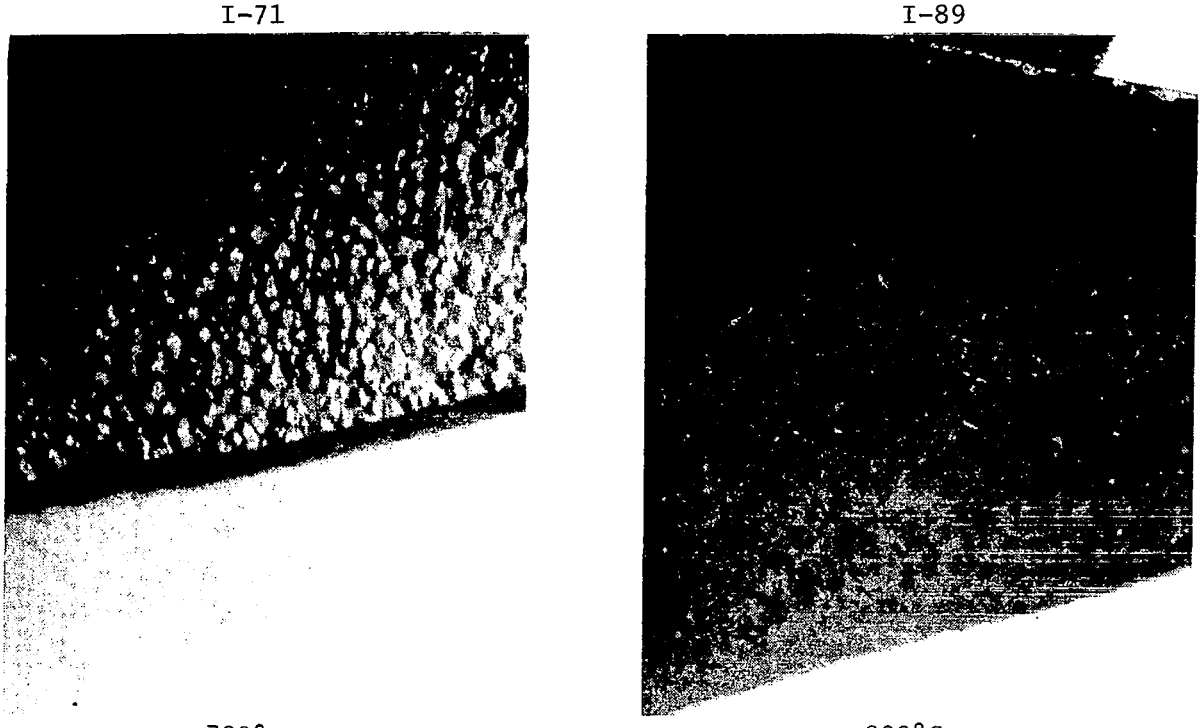

Figure 43. Surface photomicrograph showing structures grown at 700°C and at 800°C.

prevent changing the melt composition in either direction. This, however, requires extremely careful control of gas flow rates, so that one may wish to look at alternative approaches, for example, isothermal growth.

Isothermal growth was attempted, using a system similar to one described recently.* The layers obtained were generally unsatisfactory as the interface was not planar, nor was the material quality satisfactory. Photoluminescence measurements showed the material to have poor homogeneity as manifested by a broad emission spectrum. A number of attempts were made to obtain better layers without noticeable progress. The main problem was felt to be the initial wetting of the layer which could not be brought under control. Further attempts were abandoned in favor of a system that is described next.

Most of the work on LPE discussed so far was done with tipping furnaces, stationary furnaces with a slider-type boat, or rotating furnaces for the isothermal growth. The most controllable of all these is undoubtedly the slider type. In this scheme melts can be brought

*G. B. Stringfellow, P. F. Lindquist, and R. A. Burmeister, private communication.

into contact with a wafer in a more controlled way than by rotation of the boat, source wafers, etc. Wafers used to supply a desired element can be handled easily, and the melts can be removed from the wafers; that is, wiped and new melts can be brought in at any time. Furthermore, a vertical temperature gradient can be imposed on the boat by suitable design of the furnace, so that isothermal growth can also be performed. The work discussed below was done in some form of slider boat.

A problem encountered in the growth of (InGa)P junctions is the difficulty of adjusting the melt compositions so that the second melt grows the same E_g material as the end of the previous melt. A method was developed whereby this matching is greatly facilitated. The basic idea is to provide two GaAs substrates so arranged that both melts, the p- and n-melt, find themselves in an identical environment. Both melts use or gain phosphorus identically, and both melts lose material due to epitaxial growth at the same rate. Thus, one of the substrate wafers is a "dummy" wafer used to equalize the second melt, and the other wafer is the "real" wafer on which the junction is grown. This scheme is expected to be valuable in the growth of p-n junctions, especially if combined with a novel solution to the interface problem discussed next.

As mentioned above, a great deal of trouble was experienced in connection with the GaAs-(InGa)P interface. The GaAs substrate has to be chemically polished and then etched before growth; the way the (InGa)P is brought into contact with the GaAs is important. These problems contribute to the deviations and fluctuations in the results and account for the fact that the same melt composition and schedule produces different results in a series of nominally identical runs. Another source of trouble in initiating growth is the possibility that the substrate surface becomes contaminated during the run, before the (InGa)P melt is applied to the substrate. This is believed to be a common occurrence as we have found that the interface between the GaAs substrate and the (InGa)P layer sometimes contains reddish-orange deposits of phosphorus and phosphor compounds. In view of the volatility of P in the melt the condensation of phosphorus is not surprising. The scheme devised to overcome the above problems consists in the growth of a preliminary layer of GaAs, just before the (InGa)P growth. This is accomplished by a suitable modification of the boat so that the substrate is pulled under the GaAs melt first (Fig. 44). The temperature is then raised to melt back the substrate surface and dropped to regrow a GaAs layer. The substrate is next pulled under the (InGa)P bin for the regular growth. The interface obtained with this method is much improved over the standard interface, Fig. 45. However, only a very thin layer above the interface shows a good structure, the rest of the layer grown being grossly disturbed, presumably due to the change in composition. Although there are several ways in which the composition can be

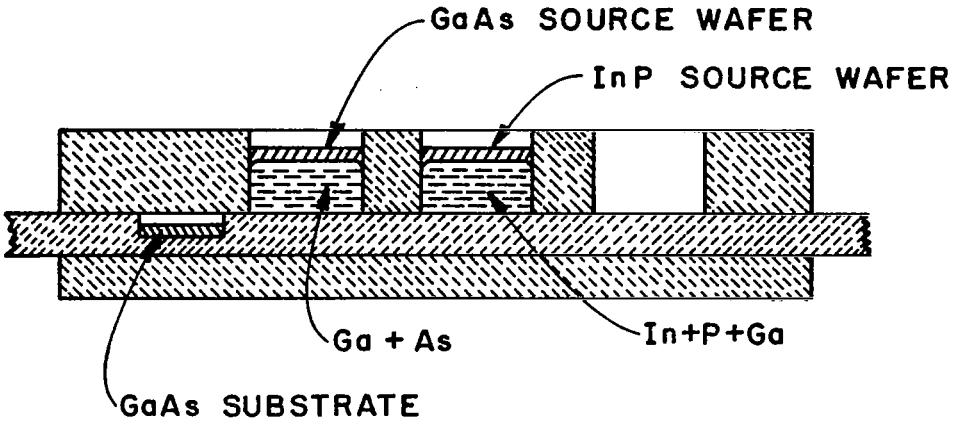

Figure 44. Slider boat used in the LPE growth of (InGa)P.

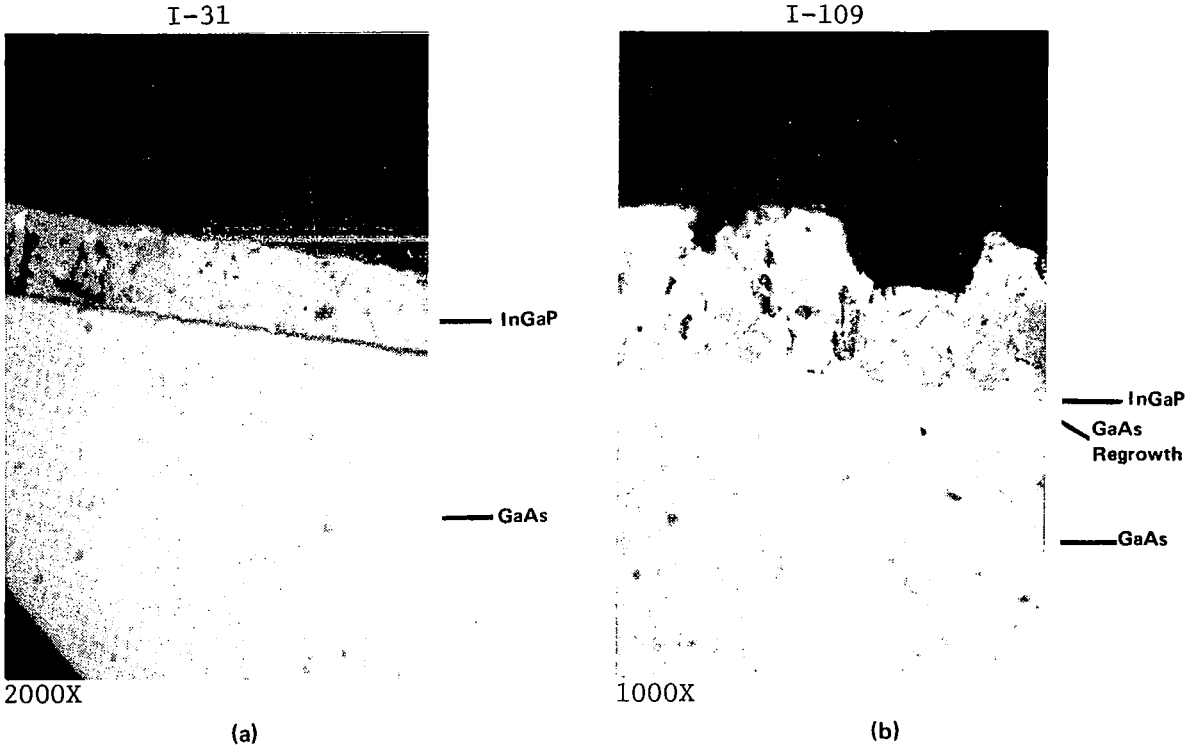

Figure 45. The interface between GaAs and (InGa)P, without GaAs regrowth (a) and with regrowth (b).

stabilized; e.g., by inducing suitable changes in the melt composition during growth or by isothermal growth, we have investigated another approach we call growth by precipitation.

Growth by precipitation consists of avoiding any cooling by exposing the substrate to a supersaturated melt, while the boat is held at a constant temperature. Thus, only that part of the melt in the vicinity of the substrate contributes to the growth. The duration of growth is short (< 1 sec), and only very thin layers were obtained. The usual causes of compositional variation (phosphorus or gallium loss) are thus avoided. Experimental tests of this method were carried out using a sliding boat. When combined with the GaAs as described before, a typical run proceeds as follows (Fig. 46). The melts are taken up to

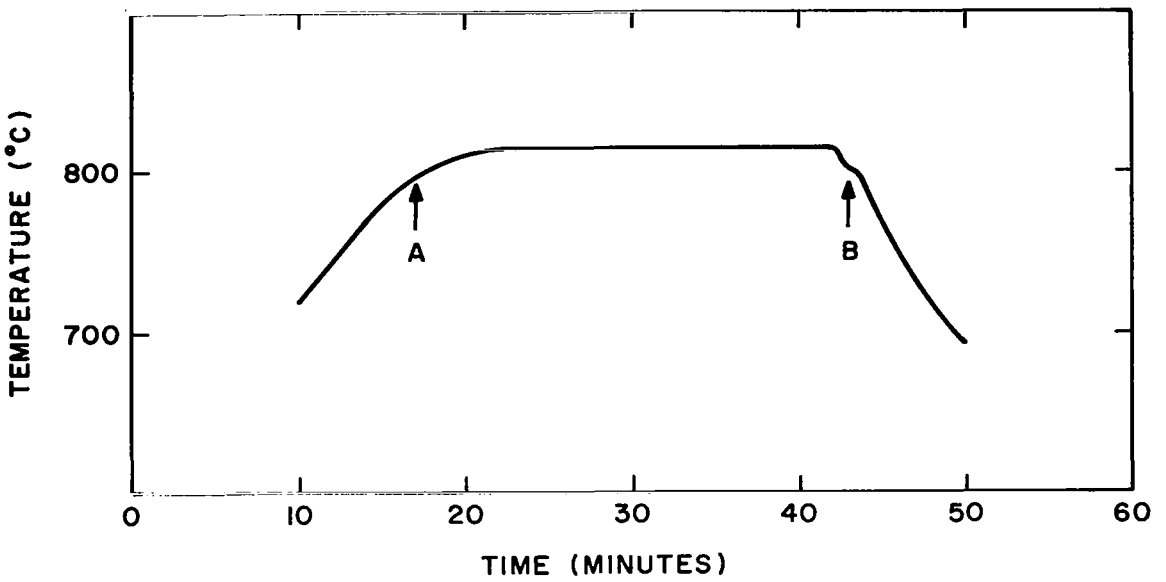

Figure 46. Temperature-time schedule for precipitation growth. The GaAs wafer is slid under the GaAs melt at A, and under the (InGa)P melt at B. The step at B is shown exaggerated in time.

800°C, then the substrate is slid under the GaAs melt, and the temperature is raised to 816° and held for 30 minutes. The furnace temperature is next lowered to 800°C during which time a new GaAs layer grows on the substrate, and the (InGa)P solution becomes supersaturated. After the temperature stabilizes, the wafer is pulled under the (InGa)P melt and 10 seconds later is pulled out again. A series of surface and cross section photomicrographs is shown in Fig. 47. The composition

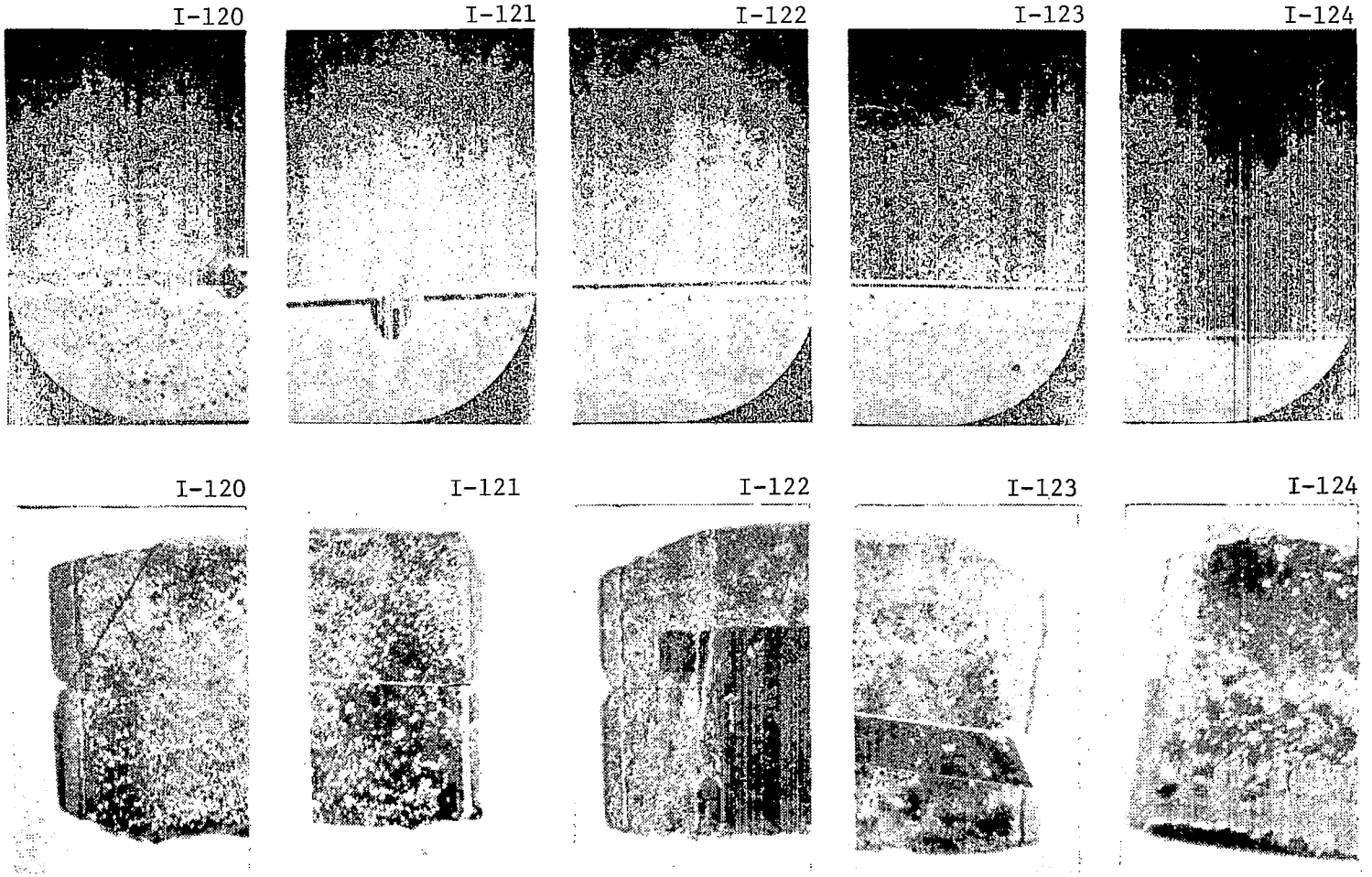

Figure 47. Photomicrographs of the cleaved cross section (top row, ∿ 300X) and the surface (bottom row, ∿ 4X), in a series of runs grown by precipitation. The melt composition changes from excess Ga over that needed to grow $In_{.5}Ga_{.5}P$, to insufficient Ga, as we go from left to right.

of the melts was varied from excess Ga on the left to insufficient Ga on the right. The difference in layer quality with composition can thus be followed. A typical thickness grown is 2.5 μm. Figure 48 is a high-magnification photomicrograph showing another layer grown by this technique. The perfect planarity of the interface and the uniformity of the (InGa)P layer are evident.

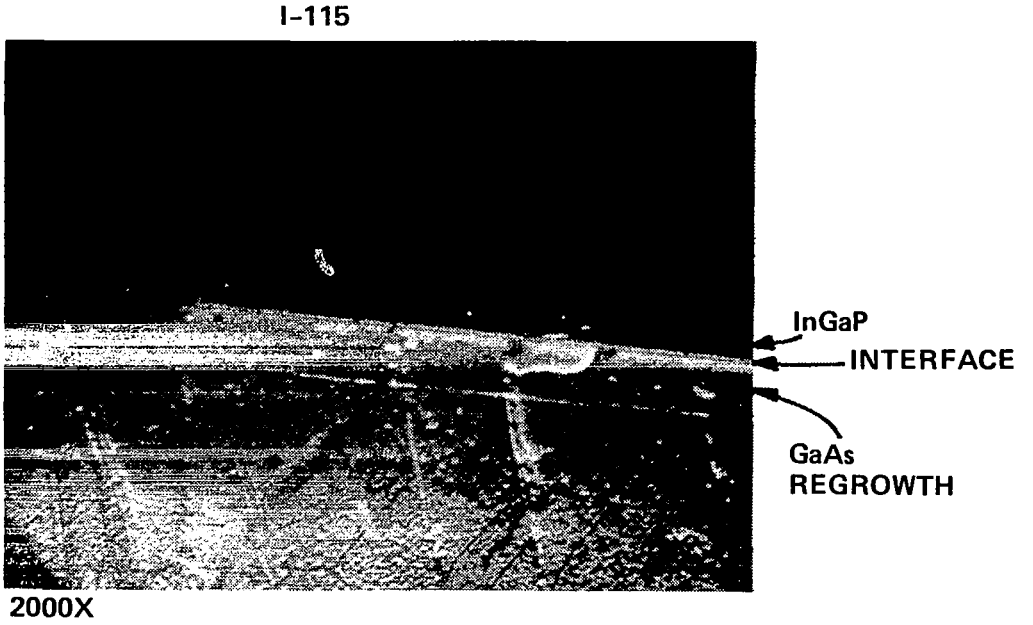

Figure 48. A high-quality (InGa)P layer grown on GaAs.

Besides photomicrography we have also examined the structure of these layers. In order to obtain more significant results, three different InGaP layers were compared. The first was a layer grown by standard cooling, the second by precipitation, and the third is a vapor-phase layer of the kind used in laser fabrication. The method used and the results obtained are discussed in the next section.

2. X-Ray Topography Studies of Epitaxial Layers. - The crystalline perfection of the (InGa)P layers was characterized by reflection x-ray topography. The (111) LPE and (100) VPE layers were examined using Cu $K\alpha_1$ radiation and the (440) and (422) diffracting planes, respectively. The topograph represents the crystallinity of the bulk of the LPE layers as the depth for 90% attenuation of the incident beam is about 10 μm for the 1- to 2-μm-thick layer. However, only the top section of the VPE layer is imaged as the depth for 90% attenuation is about

5 μm for the 20-μm-thick layer. (The lower penetration is due to the shallow angle of incidence of the x-ray beam for the diffraction conditions used for the VPE layer.) The topographs were taken with a Jarrell-Ash Lang camera and microfocus x-ray generator and recorded on Ilford G5 nuclear emulsions.

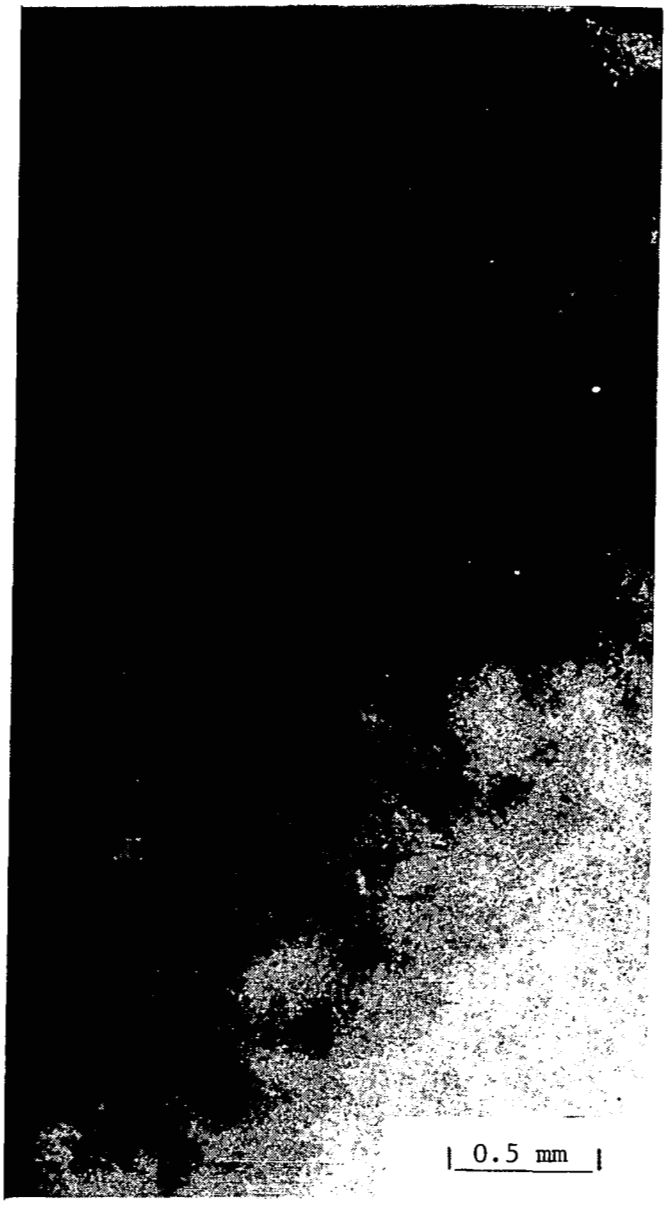

Figure 49. Reflection topograph of conventionally cooled (InGa)P layer grown on GaAs by LPE.

A reflection topograph of the conventionally cooled LPE layer is shown in Fig. 49. The layer is of poor quality and is composed of individual grains with various orientations. The dark spots are grains or clusters of grains with approximately the same orientation as the substrate. The white areas between grains are regions of material not properly oriented for diffraction.

Figure 50 shows a reflection topograph of an LPE layer grown precipitation. The "blurred" areas are excess indium on the surface.

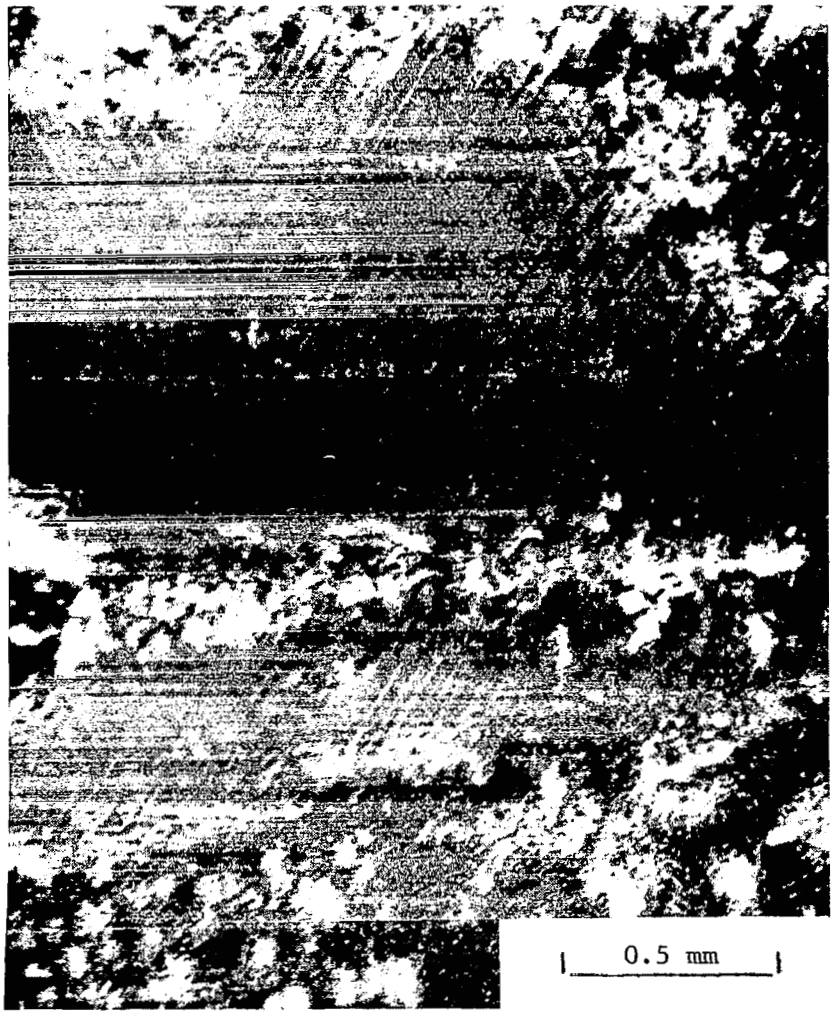

Figure 50. Reflection topograph of a precipitation-grown (InGa)P layer on GaAs.

Most of the topograph shows a uniform layer of (InGa)P. The linear arrays of defects observed are along the <110> directions, which lie in the (111) surface of the wafer. These may be clusters of misfit dislocations which are introduced by the small lattice mismatch between layer and substrate. Figure 51 is an optical micrograph of the surface of the crystal imaged in the topograph.

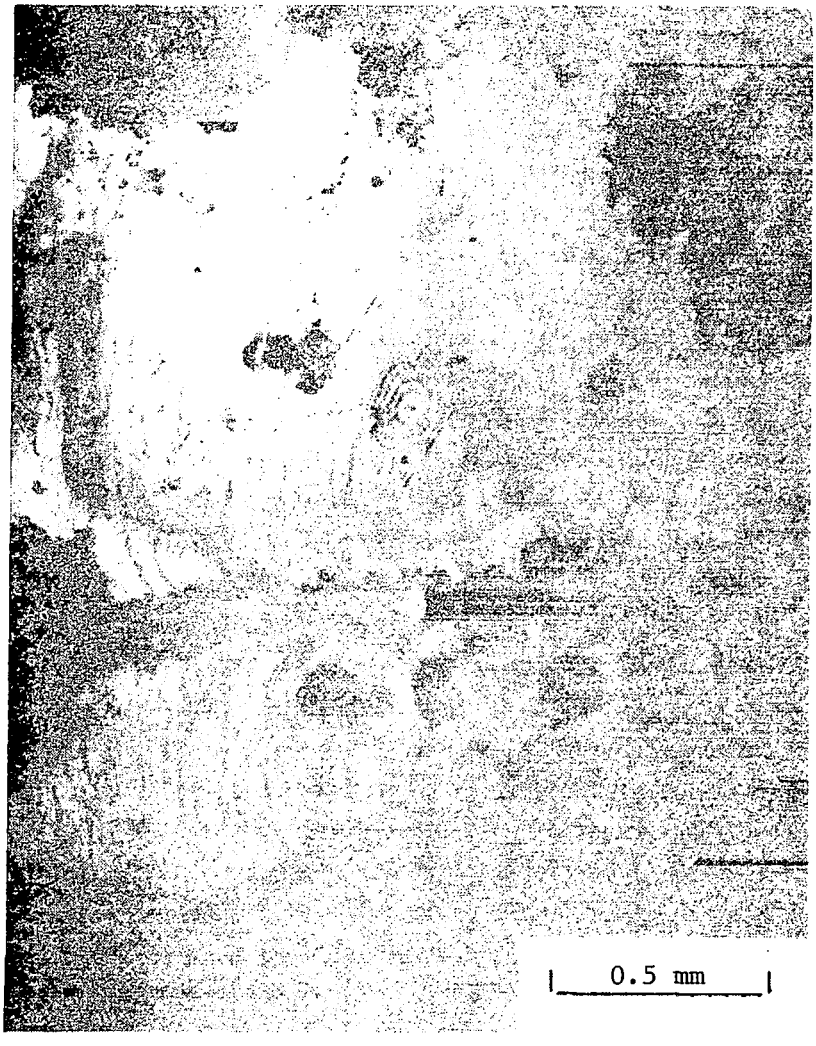

Figure 51. Optical photomicrograph of the surface of the crystal imaged in the topograph shown in Fig. 50.

Figure 52 is a reflection topograph of a high-quality VPE layer. The dominant feature observed is the cross-hatched pattern on striations

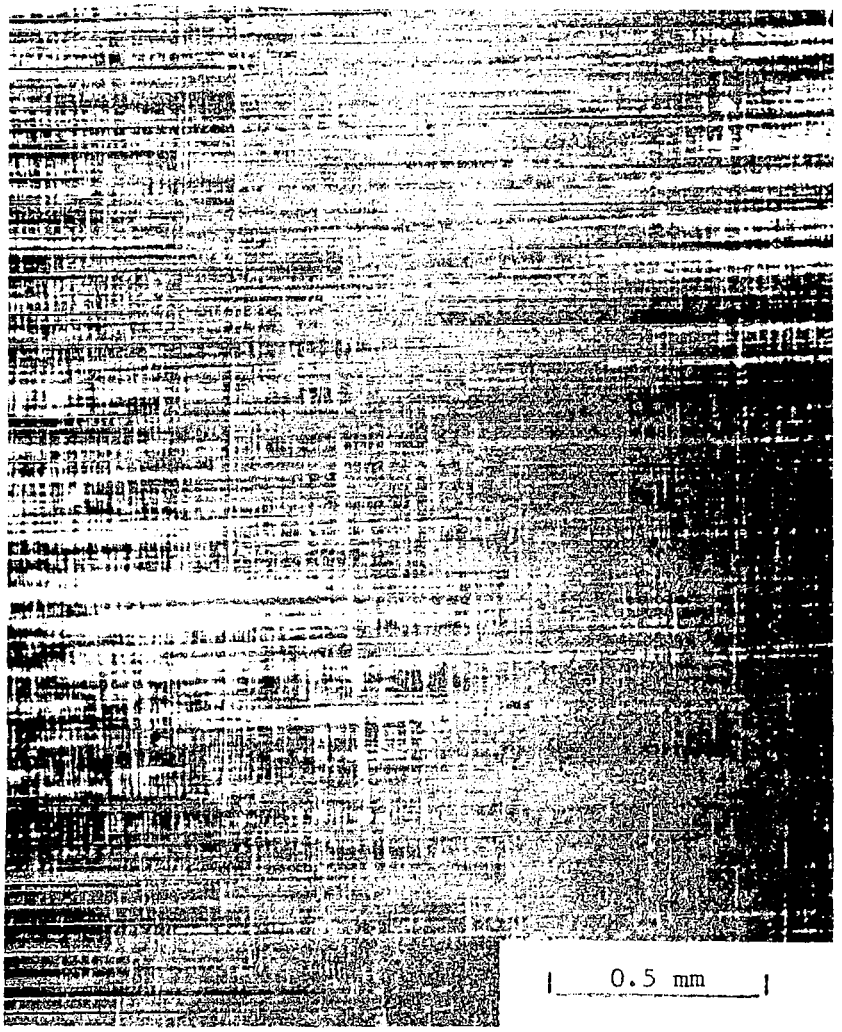

Figure 52. Reflection topograph of a high-quality VPE layer.

lying along the <110> directions in the surface plane of the (100) wafer. This structure, typical of heteroepitaxial VPE layers, is composed of clusters of misfit dislocations, and is undoubtedly associated with the lattice mismatch between layer and substrate. The crystal surface is shown in Fig. 53.

These results clearly indicate that the precipitation method has yielded device grade material, similar in quality to that obtained by vapor-phase epitaxy. The different orientation in cross-hatched pattern arises because of the different substrate orientations used, (100) for VPE and (111) for LPE.

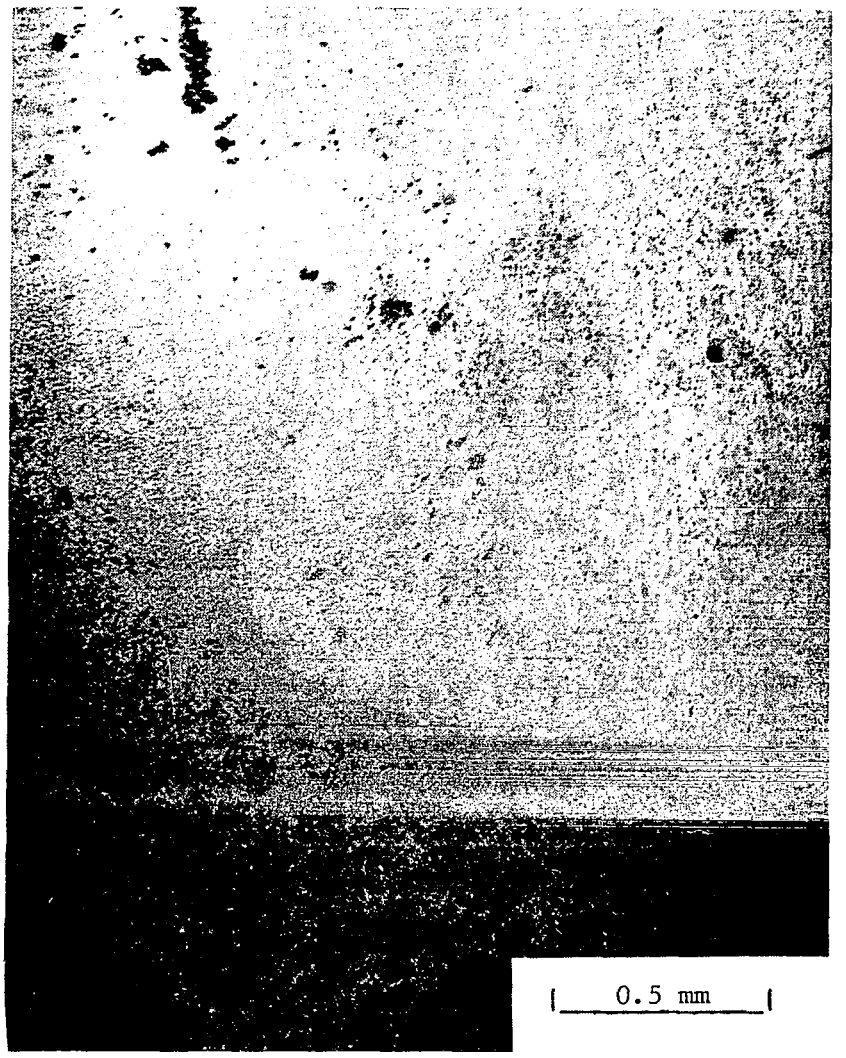

Figure 53. Optical photomicrograph of the surface of the crystal imaged in the topograph shown in Fig. 52.

It should be pointed out that in vapor-phase epitaxy, these problems are avoided as the gas streams are directed toward the substrate where they react and generate a layer whose composition remains constant as long as the gas flow and temperature remain unchanged.

3. Discussion of LPE Results. - Both isothermal growth and conventional cooling failed to produce good layers, and only precipitation from a super-saturated melt yielded structurally adequate material.

Several reasons can be suggested to explain this result. In the case of ordinary LPE growth by cooling, the composition of the grown material changes, and this introduces misfit dislocations and strains. For isothermal growth, one should, in principle, be able to overcome this problem and grow constant-composition material. Our lack of success in this method may be due to unsolved experimental problems, but there may also be more fundamental difficulties. To obtain homogeneous material, Ga and P have to diffuse through the solution over relatively long distances, so that great stability and avoidance of convection currents in the solution are essential. The precipitation method is a very simple way of solving these problems and, as shown above, is capable of yielding device-grade material. The application of this method to the fabrication of devices remains to be explored.

V. ROOM-TEMPERATURE CW LASERS: $Al_xGa_{1-x}As$

A. Multiple-Layer Epitaxy for CW Lasers

The special task of multiple-layer growth of cw laser structures involves growing adjacent very thin layers with widely varying compositions and dopings. The interfaces between these layers must be extremely flat and well defined; there must be no contamination from one growth solution to the next; the layer thickness must be precisely controlled with submicron tolerances; and the final surface must be free of any protrusions when the wafer is withdrawn from the growing apparatus.

There are many possible designs of the growth apparatus, but the linear (as opposed to circular) multiple-bin graphite boat (ref. 6) has proven the most popular. Two possible designs (ref. 7), among many, are shown schematically in Fig. 54. In Fig. 54(a), a GaAs source wafer, usually polycrystalline, precedes the substrate wafer into each bin and assures saturation of the solution before growth on the substrate is initiated. Figure 54(b) is an improvement over this design in that each solution has its own source wafer, and saturation of the solutions is maintained throughout the entire growth cycle. The source wafers are dropped into relatively small solutions that are near the growth temperature and are spread over the entire substrate wafer area by the quartz block weights. The resulting thin (typically < 1 mm) solutions yield epitaxial layers the thickness of which can be calculated directly from the phase diagram (ref. 44) because the formation of platelets in the solution is greatly reduced. Typical growth efficiencies, defined as the ratio of the thickness grown to that calculated from the phase diagram, range from 0.1 for 1-cm-thick solutions to greater than 0.9 for solutions 0.2 mm thick. More precise saturation can be obtained by adding a bottom source wafer, as shown in Fig. 54(a), to the thin solution method of Fig. 54(b). Figure 55 is a photograph of a seven-bin boat (with one side removed) which combines the ideas of Figs. 54(a) and 54(b). The top sources are shown in their initial position above the 1-g solutions which will be flattened to 1-mm thickness by the action of the quartz weights.

The reason for this preoccupation with melt saturation is apparent if one considers the growth of layers on the order of 0.1 μm in thickness. Thus, in Fig. 56 we see a cross section at 2000X magnification of a narrow cavity with a series of structural failures, spaced periodically along the wafer. These were caused by growth-meltback difficulties which only appear with very thin layers.

Another source of growth problems is illustrated in Fig. 57. One can see that certain areas of the substrate were not wetted by the high Al layers. This illustrates the special problems which arise in the growth of (AlGa)As, and which are connected with wetting difficulties caused, for example, by oxide film formation on the (AlGa)As melt.

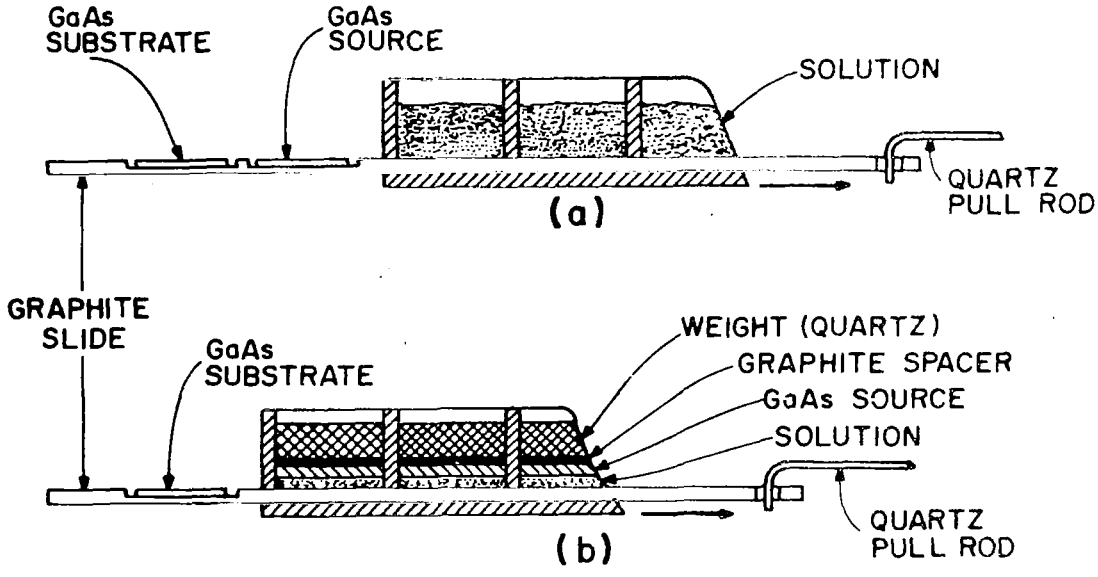

Figure 54. Schematic illustration of growth boat. In (a) the saturation of the solutions is completed by the source wafer preceding the substrate wafer while in (b) each solution is saturated by its own source wafer.

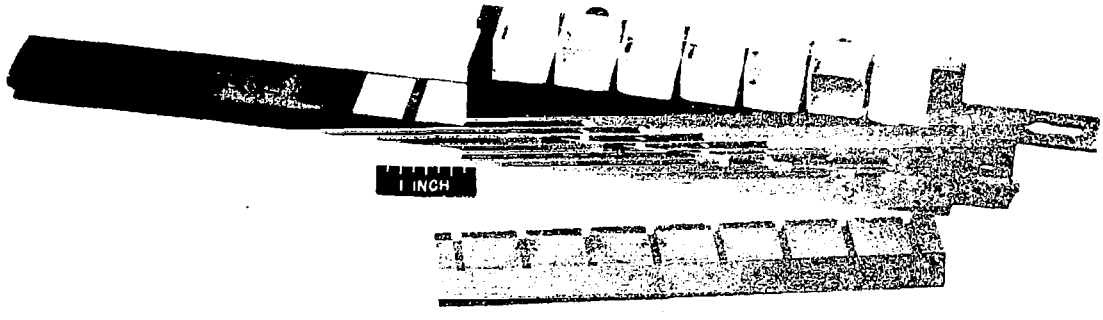

Figure 55. Photograph of seven-bin boat showing bottom as well as top sources in their initial position.

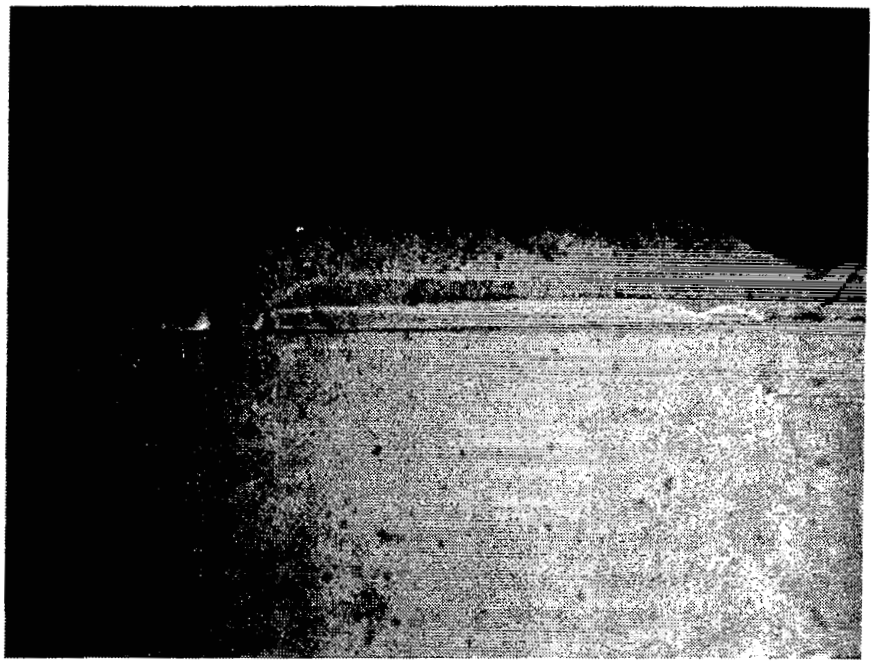

Figure 56. Cross section at 2000X magnification showing poor wetting of (AlGa)As layers and good wetting of GaAs layers.

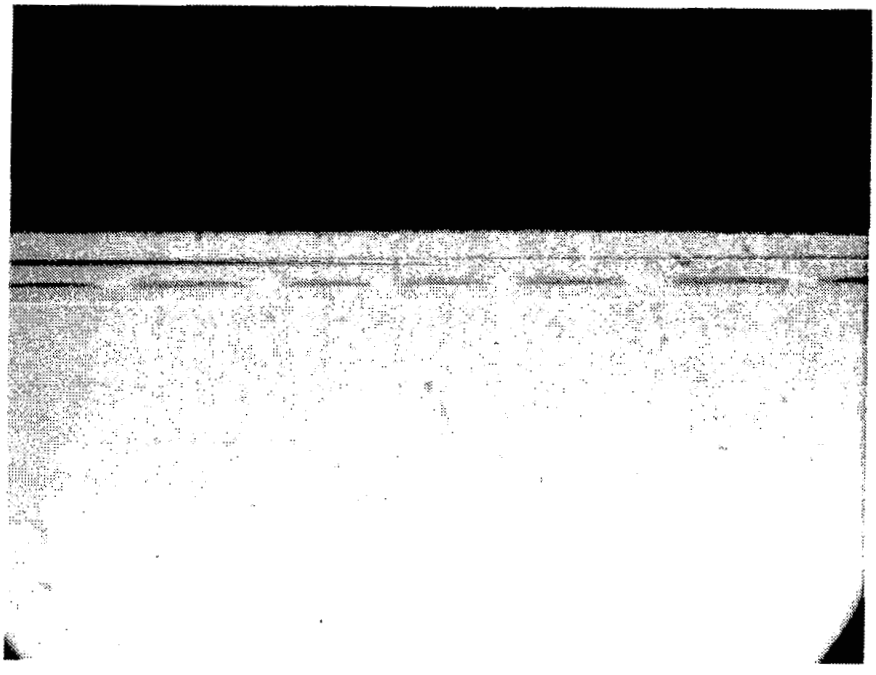

Figure 57. Structural flaws in very thin LPE layers caused by poor growth control (2000X magnification).

For this same reason, the longitudinal temperature gradient in the growth furnace is also important. If the substrate enters a bin at a temperature higher than the solution in that bin, there may be partial dissolution of the substrate because of undersaturation at the solid-liquid interface; therefore, a decreasing temperature gradient is undesirable when the control of extremely thin layers is involved. An increasing temperature gradient is more favorable because there will be deposition rather than dissolution when the substrate enters a bin which is at a higher temperature. In either case, large temperature gradients require more rapid cooling, thus aggravating the problem of layer thickness control.

The major cause of liquid cross-contamination between solutions in adjacent bins is also the cause of poor wiping after the growth of the final epitaxial layer. Any geometric artifact such as a major defect or dendrite on the surface will cause the solution to adhere in that area. One observes along both sides of the wafer, where the crystal is held in place, that dendrites have grown and that wiping after the last layer growth was incomplete. Since this inhomogeneity is confined to the edge of the crystal, it is not serious in terms of subsequent processing. However, along the leading edge there is a network of small defects, which are made visible by the presence of gallium solution not removed by the final wiping.

Figure 58 is a photograph of a multiple layer structure which is free of any surface irregularities. There are gradual steps in this surface with a height of only 0.1 μm or less; thus, the wafer can be processed for ohmic contacting without the need of a polishing step. This is especially important when the active layers of the structure are within a few micrometers of the surface as they are in the cw laser. A cleaved and stained cross section SEM photograph of a crystal with dimensions typical of cw double heterojunction lasers is shown in Fig. 59. Contact is made to the heavily doped GaAs:Ge surface contact layer grown on top of the (AlGa)As p-type region which provides the upper dielectric wall of the 0.2-μm-thick GaAs active region beneath it. To minimize (vapor) cross-contamination of the solutions, germanium with its lower vapor pressure is preferred over Zn as an acceptor, particularly in structures with thin regions which require slow growth ($< 0.5°C/min$).

B. CW Laser Diode Design Aspects

The problem of designing cw laser diodes with high concentrations of (AlGa)As in the recombination region to shift the emission wavelength

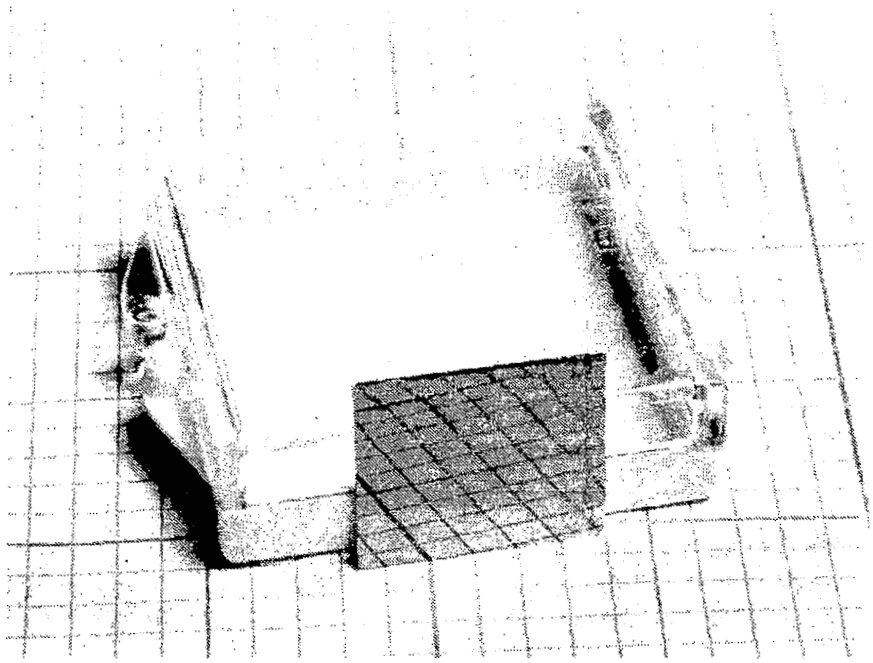

Figure 58. High quality, as-grown wafer containing multiple GaAs/AlGaAs layers required for DH cw lasers. One small square is 0.1 in. on a side.

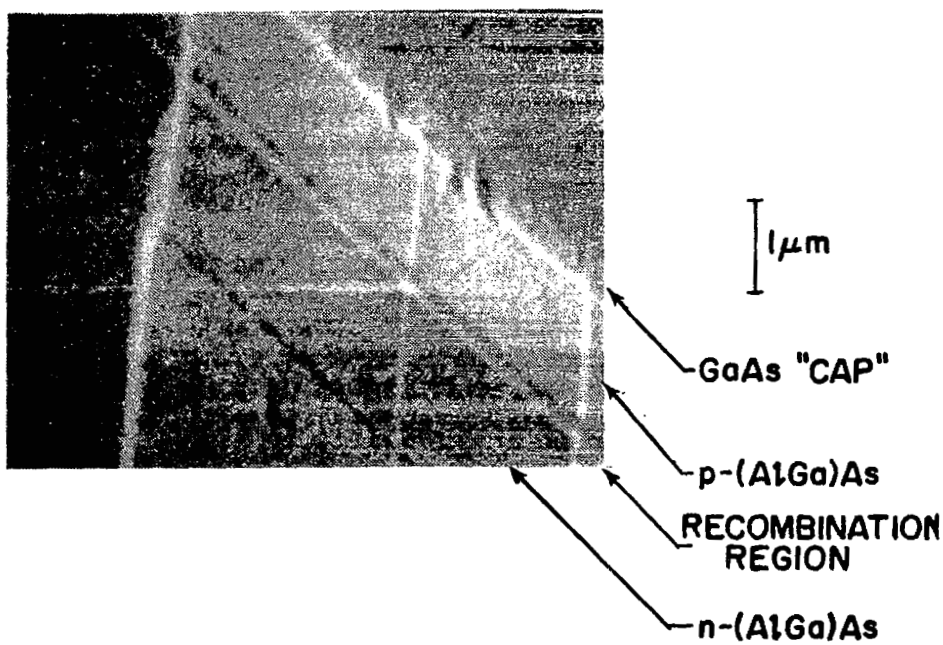

Figure 59. SEM photograph of a cw laser structure.

into the visible portion of the spectrum consists of compromises between the following requirements:

(1) Need to reduce the radiation and carrier confinement region to reduce the threshold current density.
(2) Minimum thermal and electrical resistance.
(3) Minimum strain introduced by the lattice parameter mismatch at the various interfaces.
(4) Maximum reliability under conditions of cw operation.
(5) Minimum beam divergence.

The desire to satisfy (1) leads to problems with (3) and (5) since high bandgap energy steps are needed at the heterojunctions to obtain maximum confinement, with the result that the strain is relatively high and the beam broad. With regard to (2), it is desirable to reduce the distance between the recombination region and the surface to a minimum. However, if this distance is too small, then excessive optical losses can occur as a result of the penetration of the optical field into highly absorbing regions near the diode surface. In the discussion that follows, we present the result of the design approach chosen in this program.

1. Radiation and Carrier Confinement. - Two basic approaches exist to reduce the threshold current density to a minimum: (a) High barrier heterojunctions at proper separation, to ensure full carrier and radiation confinement and (b) very closely spaced heterojunctions with adjusted barrier heights to ensure a controlled degree of radiation spread into the surrounding higher bandgap (AlGa)As.

The second approach, originally applied to GaAs double heterojunction diodes (refs. 45 and 46), leads to a desirable combination of low threshold current densities, moderate beam divergence, and ease of fabrication. This approach was used for the present devices. To illustrate the basic confinement phenomena, we show in Fig. 60 a plot of the radiation intensity as a function of distance across the recombination region for a heterojunction spacing d = 0.2 μm, assuming GaAs in that region. Three values of the refractive index step are chosen to show how it affects the spread of the radiation field beyond the recombination region. The areas of the curve are normalized to facilitate the visual determination of the fraction of the radiation inside the heterojunctions. The illustrative Δn values of 0.06, 0.10, and 0.22 are representative of the index steps attainable with the use of varying (AlGa)As values in the regions surrounding the recombination region (see Fig. 61* for a correlation between Δn and ΔE_g). With the lowest Δn value, the fraction of the radiation within the cavity is very small with strong tails extending 1 μm on both sides.

*Figure 61 appears earlier in this report as Fig. 14. It is repeated here for the convenience of the reader.

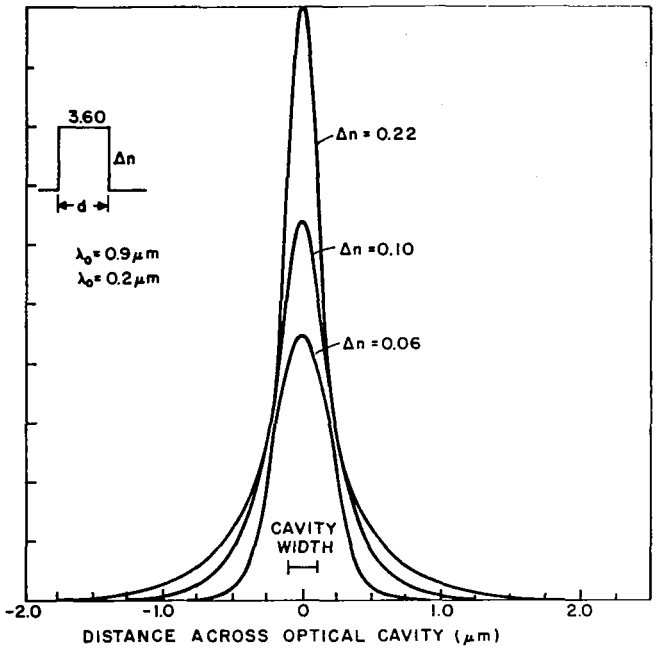

Figure 60.

Radiation intensity as a function of distance across the recombination region for a heterojunction structure with indicated geometry.

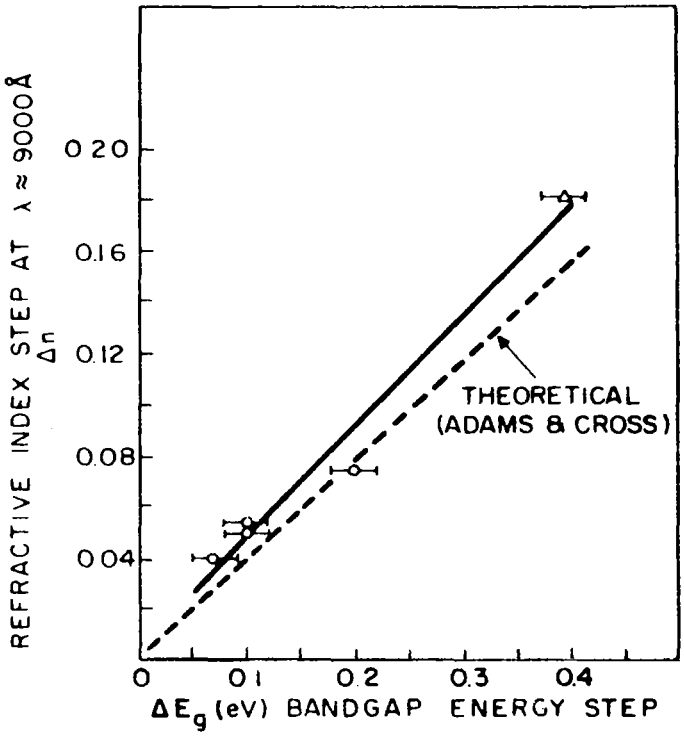

Figure 61.

Refractive index step (Δn) at 9000 Å as a function of the bandgap energy step at the heterojunction at room temperature. The theoretical curve of Adams and Cross (ref. 12) does not include the contribution to Δn due to differences in the free carrier concentration.

A quantitative determination of the degree of radiation confinement is obtained from Fig. 62 as a function of both Δn and d. As d is increased for a given Δn, the intensity confinement factor increases, but for d in excess of 0.8 μm, the confinement is nearly complete for all the Δn values shown.

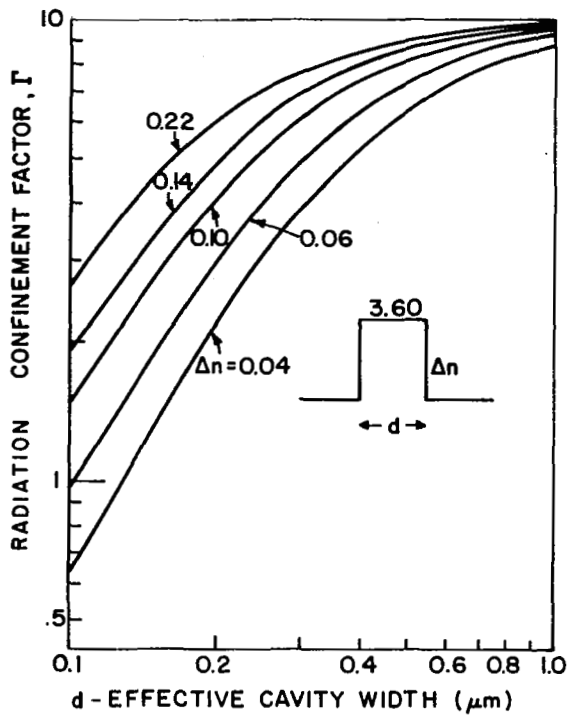

Figure 62. Radiation confinement factor Γ as a function of recombination region width and index step Δn.

The choice of heterojunction spacing and Δn values affects greatly the far-field pattern in the direction normal to the plane of the junction because the beam divergence increases with increasing confinement. Figure 63 shows the half-power (full-width) angular beam width as a function of d and Δn. From Fig. 63 it is clear that a very large range of beam width values is possible by properly choosing d and Δn. It is evidently desirable to obtain the lowest possible width consistent with low threshold operation. The design choice that was found most useful for the present program consisted of using d values between 0.2 and 0.3 μm, with $\Delta n \approx 0.1$ (corresponding to bandgap energy steps of $\Delta E_g \sim$ 0.2 eV at the two heterojunctions). This yields a theoretical beam width of 30 to 35°.

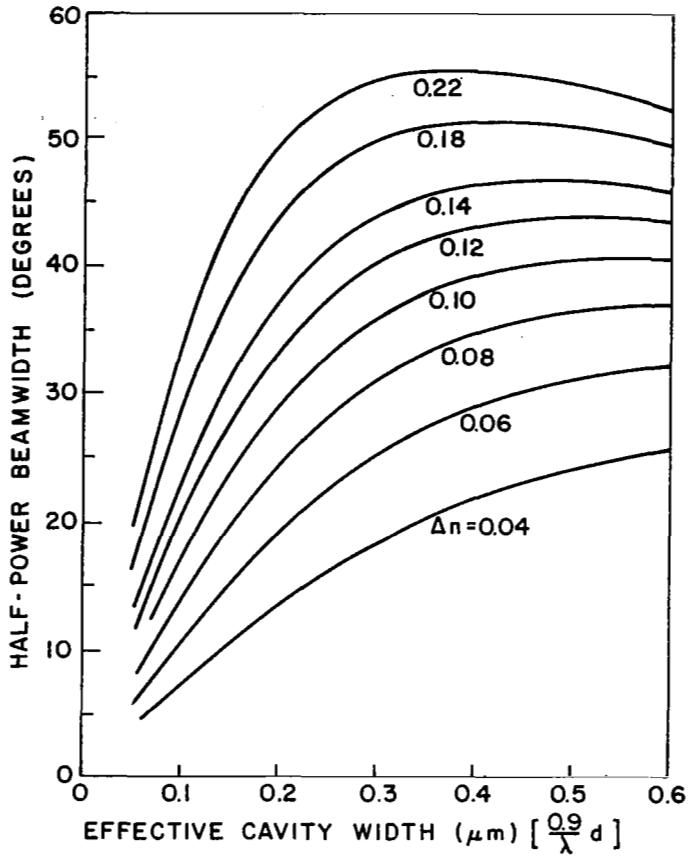

Figure 63. Beam width as a function of index step and recombination region width.

In view of the radiation spread, it is important to prevent excessive absorption losses due to field penetration into highly absorbing regions in the vicinity of the recombination region. The structure used incorporates a p-type GaAs surface layer to facilitate ohmic contact. It is possible to determine the effect of changes in relevant dimensions by solving the field distribution and the consequent gain coefficient needed at threshold, taking into account the absorption coefficients and the relative fraction of the wave traveling in the various regions in the vicinity of the recombination region. Figure 64 shows how the required gain coefficient at threshold varies with the distance between the recombination region and the highly doped (10^{19} cm^{-3}) GaAs surface layer for various values of the Δn. These calculated results show, for example, that for a $\Delta n = 0.1$, the distance W_1 should be at least 1 μm. With less confinement (e.g., $\Delta n = 0.06$), that distance would have to be doubled to $\sim$ 1.6 μm for the p^+ region not to affect the laser threshold.

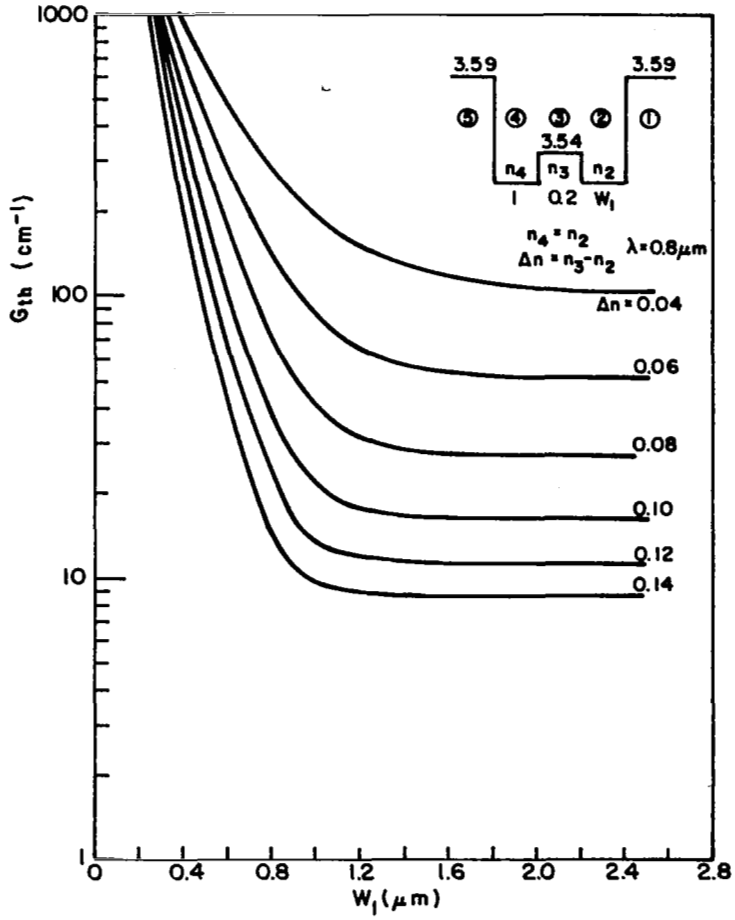

Figure 64. Gain at threshold for indicated geometry as a function of Δn and "wall" dimension.

2. Thermal Problems. - The importance of the various layers insofar as they contribute to the thermal resistance can be estimated. Thus, for a planar structure, the temperature rise is given by

$$\Delta T = \frac{IV(1-\eta)}{A}\left(\frac{d_3}{K_3} + \frac{d_4}{K_4} + \frac{d_5}{K_5} + \frac{W \ \ell n \frac{4L}{W}}{2\pi K_6}\right) \qquad (13)$$

where d_i, K_i refer to the thickness and thermal conductivity of the i^{th} layer or material, L is the device length, and W the width. From the data in Fig. 65 it can be seen that K_3 exerts a dominating influence on the thermal resistance. For example, with W = 100 μm, L = 400 μm, and IV $(1 - \eta)/A = 2000$ W/cm^2, we get

$$\Delta T = 1.6° \left((AlGa)As\right) + 0.4°(GaAs) + 1.25° \text{ (metallization)} + 1.1° \text{ (heat sink)} \quad (14)$$

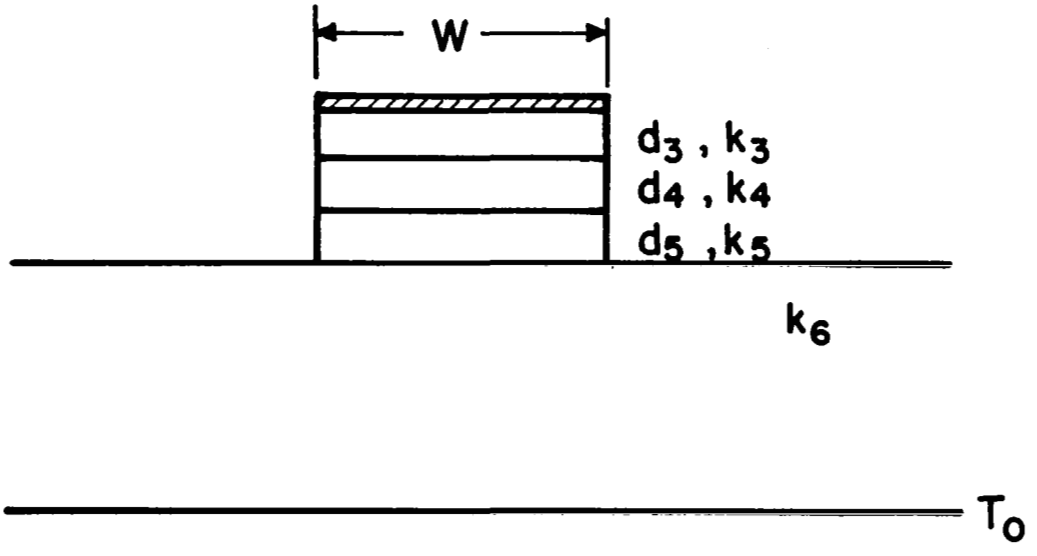

Thermal Conductivities ($Wcm^{-1}°C^{-1}$)

k_3 = 0.125	(AlGa)As	$d_3 \cong$ 1μm
k_4 = 0.5	(GaAs)	$d_4 \cong$ 1μm
k_5 = 0.8	(In)	$d_5 \cong$ 5μm
k_6 = 4	(Cu)	

Figure 65. Model for laser diode thermal conductivity calculation.

Regardless of the accuracy of this estimate, the first layer composed of (AlGa)As is seen to be more important than any of the others. Thus, it is an objective of proper design to keep this thickness to a minimum. The above estimate is optimistic since it is based on a grossly simplified geometry, it neglects interface effects, and it assumes perfect soldering.

Other calculations can be made, where one attempts to assess the importance of two- or three-dimensional heat flow, as compared with the simple case of one-dimensional flow. The question that one wishes to answer is whether better heat dissipation is in fact obtainable from a given stripe geometry. A rough way to obtain an answer to this problem consists in calculating the normalized thermal resistance for a stripe and a broad area unit, with a single thermal conductivity. We define this normalized thermal resistance R,

$$R = \frac{\Delta T}{IV} LK \tag{15}$$

where L is the diode length, K the thermal conductivity, and IV the power input. One obtains for the one-dimensional geometry, $R = d/W$ and for the stripe geometry, $R = (d/W)/(1 + 2d/W\pi)$. In these expressions d is the distance between the recombination region and the heat sink, and W is the device or stripe width. This is illustrated in Fig. 66 where it can be seen that the thermal resistance for the stripe does not begin to differ from that for the one-dimensional structure until the ratio d/W becomes equal to 1 or more. The stripe is beneficial (from the thermal point of view) when the distance from the heat sink approaches the device width. For our devices, with d on the order of 2 to 3 μm, W

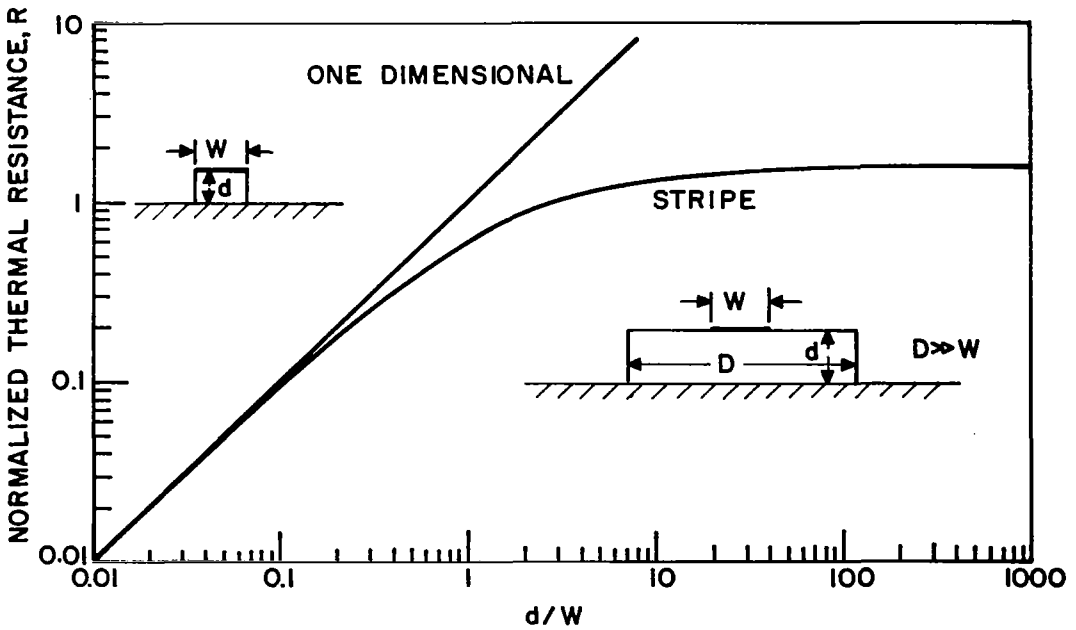

Figure 66. One-dimensional and two-dimensional (stripe) heat flow calculation for an idealized geometry.

must be also equal to a few μm, and for W $\gtrsim$ 20 μm the performance of a one-dimensional device should be not much different from that of a stripe. In fact, the situation is even more distorted, since stripe devices suffer from lateral loss of carriers and current confinement problems, so that their effective threshold current densities can become 2 or 3 times that of one-dimensional devices (see Section C). It appears, therefore, that as far as wide devices are concerned, stripe geometry offers no major *thermal* advantage.

3. Current Constriction. - The reasons for the use of stripe configurations for cw lasers are connected with better heat dissipation for narrow devices, with removal of sawed edges from the active region of the device (shown elsewhere in this report to be of paramount importance), and with reduced threshold current due to current constriction. To investigate alternate forms of current constriction we have studied proton bombardment isolation (ref. 47).

Standard layers were grown and stripes of metal were deposited on the surface, which then became masks for the proton bombardment. Experiments were conducted using 260-keV protons at a dose of $3 \times 10^{15}/cm^2$. The bombarded layer was processed both without and with annealing for 15 min at 450°C. The threshold currents obtained were low, about 150 mA for our standard material. However, in neither case was adequate life obtained under operating conditions. Typical output dropped to 50% of the initial value in 24 hr regardless of anneal. One explanation for this is associated with the damage introduced by the bombardment at the edge of the active region. As reported in other sections of this report, such damage can become the origin of defects which move into the recombination region during operation and which reduce the output and efficiency. It appears from the above work that the bombardment damage is not easily removed by anneal, and that more extensive studies would be required to elucidate this problem in order to obtain lasers comparable in quality to those we obtain with our regular process described below.

Our standard method of producing striped lasers involves the use of the simplest technique (ref. 48). A layer of SiO_2 is deposited on the surface of the wafer using a silane vapor phase deposition system. The wafer is next coated with photoresist, exposed through a mask containing the desired stripe configuration, and processed in the usual way, resulting in narrow ($\gtrsim$ 10 to 13 μm) openings in the SiO_2 (wider widths are also used). Zinc is now diffused through the openings, to a depth of approximately 0.2 μm, after which the p-surface is provided with solid metal contacts. A Sn-layer is used for the n-contact, after which the material is ready for cleaving and mounting.

A diffusion isolation process (ref. 49) for confining the current was also studied. This involved the growth of an n-layer (instead of

the usual p-layer) on top of the p-type (AlGa)As layer. Thus, current cannot flow except in regions made p-type by a subsequent diffusion step. The zinc diffusion must therefore penetrate to the p-type (AlGa)As layer, and *not* any deeper as that would affect the optical cavity and the laser reliability (see Section D-2). Diffusion depth is seen to be a critical parameter, and the diffusion process, in general, must be carefully controlled to avoid the introduction of nonradiative centers. By careful Zn-control, we have succeeded in fabricating long-lived ($\sim$ 1000 to 3000 hr) cw lasers by this method, but with no advantage on our standard oxide stripe process and a lower yield of useful diodes.

4. Facet Protection. - As shown in the section on reliability, we have found that facet erosion is an important potential degradation mechanism in cw lasers. Some form of facet protection is thus of great importance. We have experimented with Al_2O_3 coatings deposited by electron beam evaporation, and with glass coatings deposited by sputtering. The first method appears under fairly good control at present, so that we expect to be able to evaluate its effect on diode life in the near future. The second method has been shown to be feasible, and it offers the further advantage that the relatively low index of the glass ($\sim$ 1.5) makes the deposition of half-wave coatings less critical. Half-wave coatings are used at present since they do not affect the threshold current of the device, although one might for some applications prefer a different reflectivity.

C. Experimental Results

The laser structure used for most of the experiments is shown in Fig. 67. The lasing wavelength was varied by changing the Al concentration in the three relevant regions of the diode, with the bandgap energy step ranging from 0.2 to 0.4 eV depending on the specific device. In the majority of cases, the recombination region was undoped ($n = 5 \times 10^{16}$ cm^{-3}) to obtain the shortest possible lasing wavelength for a given Al concentration. With GaAs in the recombination region, the lasing wavelength is 8830 Å corresponding to 1.40 eV, or 25 meV below the best available value for the bandgap energy of GaAs at room temperature, 1.426 eV. Thus, lasing does not occur via the parabolic band edges, but rather through tail states that are probably introduced as a result of the high injected carrier level of about 10^{18} cm^{-3} as discussed elsewhere (ref. 50). The emission shifts to higher energy at the approximate rate of 0.01 eV per atom % Al in the recombination region.

The lowest threshold current densities have been obtained between 8800 Å and 7800 Å, with the device characteristics being most reproducible at this time in the 8800 to 8000 Å range. All the materials were

first evaluated in broad area diode form (forming the diode walls by sawing). Threshold current density for diodes 16 mils long in the above spectral range having the cw structure shown in Fig. 67 is typically 1300 to 1600 A/cm^2 (see Fig. 68) with differential quantum efficiencies of 35 to 40%.

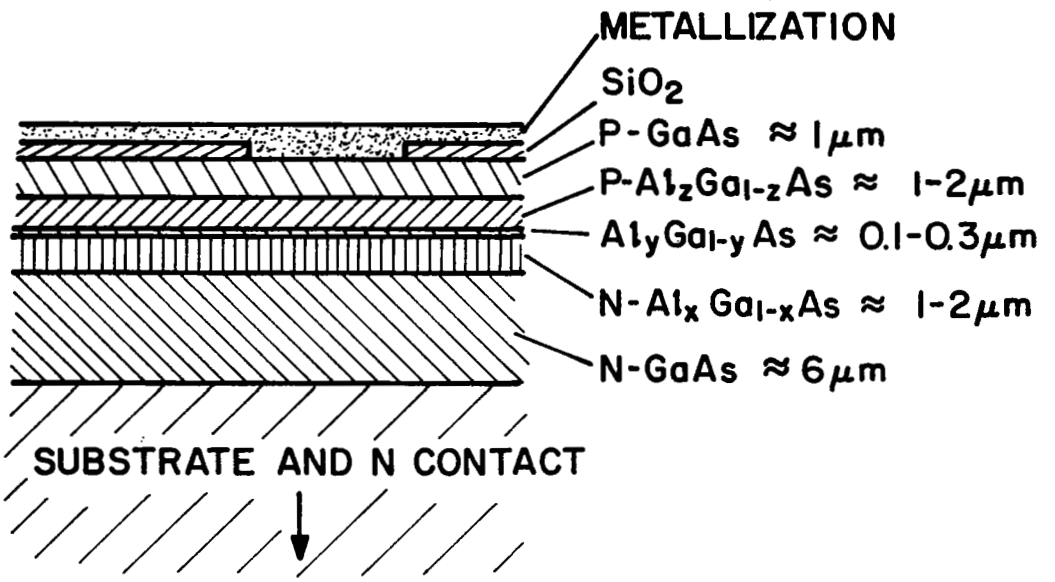

Figure 67. Typical laser structure for room-temperature cw operation.

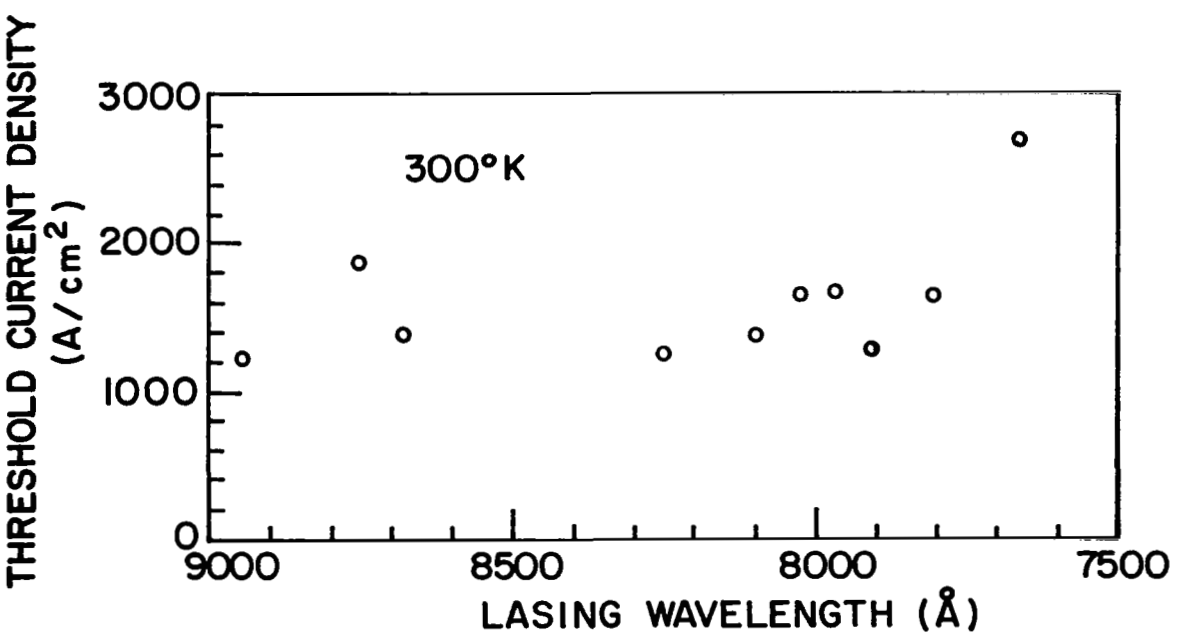

Figure 68. Dependence of threshold current density at room temperature on lasing wavelength of (AlGa)As cw laser structures (broad area contacts).

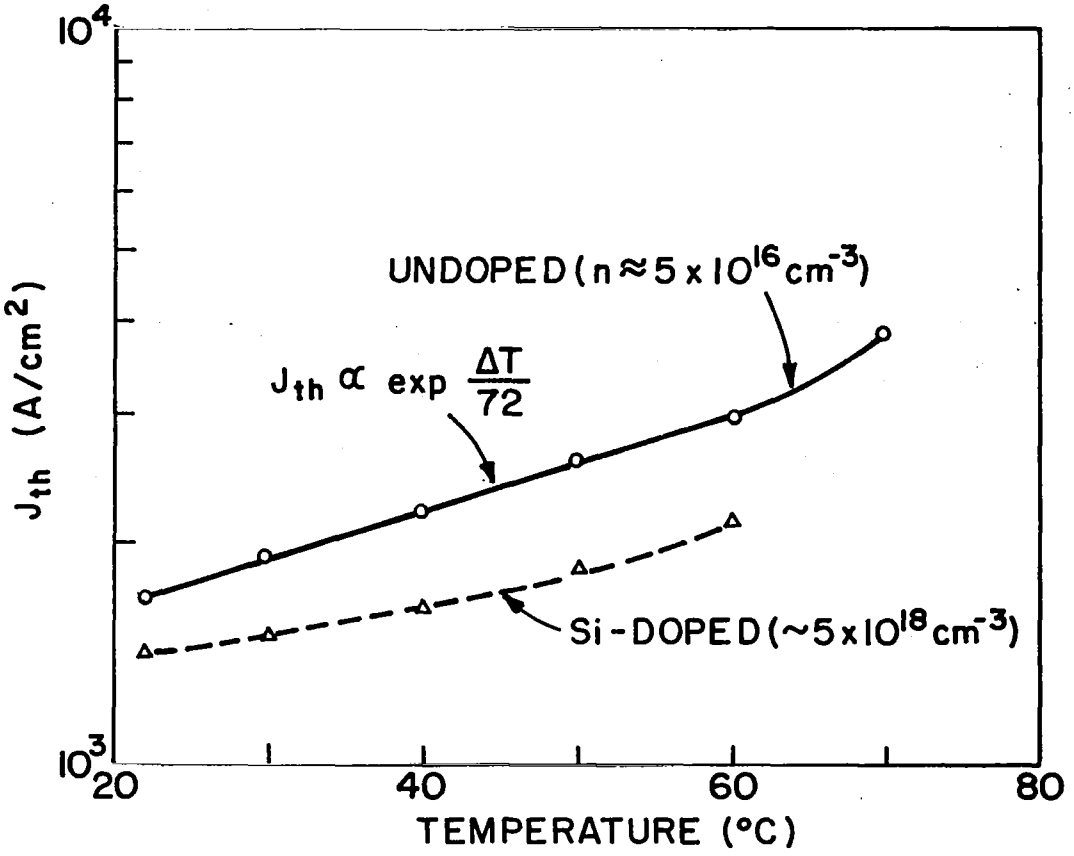

Figure 69. Threshold current density vs. temperature for laser with silicon in the recombination region ($Al_{.1}Ga_{.9}As$), and an undoped recombination region.

The dependence of the threshold current density on temperature is a function of the doping of the recombination region. In general, it is desirable to minimize the threshold increase with increasing temperature in order to allow the widest possible latitude in cw operation. Figure 69 shows the temperature increase of J_{th} for two lasers, one with an undoped recombination region, and the other with a recombination region containing about 5 x 10^{18} cm^{-3} Si atoms. The J_{th} increase with temperature is seen to be reduced to some extent by the addition of Si ($\sim$ 5 x 10^{18} cm^{-3}) to the recombination region, but the effect is not sufficiently large to be a dominant factor, and other device aspects are therefore to be considered of more importance. For the undoped diode,

$$J_{th} \propto \exp \frac{\Delta T}{T_o} \tag{16}$$

with T_o = 72°K. The above expression is useful in estimating the junction temperature rise as a function of duty cycle by noting the threshold increase. Also useful in this regard is the dependence of the emission wavelength. Figure 70 shows that above room temperature, for a diode with an undoped recombination region (n = 5 x 10^{16} cm^{-3}),

$$\frac{\Delta h\nu_L}{\Delta T} = 5 \times 10^{-5} \text{ eV/K.} \tag{17}$$

Slight variations are observed in other diodes with different doping levels, but the above value is representative of similarly constructed diodes.

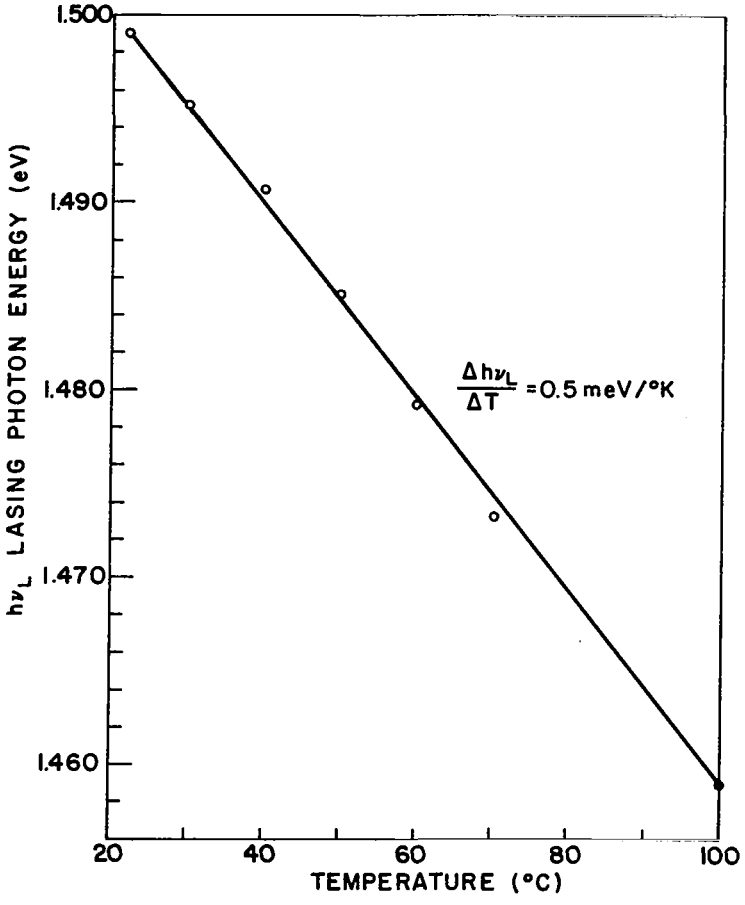

Figure 70. Lasing energy as a function of diode temperature for undoped recombination region DH laser emitting in the 8000- to 8200-Å range.

The majority of the cw laser structures were made using SiO_2 stripe isolation with stripe widths of 13 μm. In some wafers, comparative analyses were made with stripe widths of 50 and 100 μm. Table IV compares the threshold currents for the three stripe widths. Because the carriers spread beneath the stripe a minimum distance of a diffusion length within the recombination region, and since current confinement depends on the relevant layer conductivities, the effective diode width is several micrometers wider than the stripe. For the 13-μm stripe, the effective width as measured by infrared imaging of the emitting diode region is typically 18 μm, while with the 50-μm stripe width it is 55 to 60 μm. As seen in Table IV, the difference in threshold current density between the wide diodes and narrow stripes is about a factor of two. The reduction in diode efficiency noted with narrow oxide stripes is generally attributed to optical losses as well as carrier losses in the regions adjoining the stripe (ref. 51).

The shortest wavelength at which cw laser operation was obtained at or near room temperature was 7800 Å consistent with the ability to obtain very low threshold current densities. Figure 71 shows the power output of a cw laser emitting at ∿7800 Å as a function of diode current. Figure 72 displays the spectral emission as a function of current, with power emitted indicated for each spectral plot. The diode shown exhibits the desirable property of narrower spectral width with increasing current resulting in only two longitudinal mode lines at a 0.6-A current level. Other lasers do not show this improved modal selectivity with increasing drive, for reasons as yet unclear. The far-field beam pattern for the same device is shown in Fig. 73. The half-power full width in the direction perpendicular to the junction is 30°, while in the other direction the beam divergence is 6°. In general, we find that the beam divergence is not greatly affected by the increase in drive current above threshold.

During the present program, only a limited number of experiments were conducted in actually fabricating cw laser diodes with emission wavelengths below 7800 Å. We did find that the addition of aluminum to all of the regions of the laser structure to shift its wavelength to shorter values resulted in anomalously high threshold current densities far in excess (factor of 2 to 3) of what would be expected on the basis of the theoretical shift of the internal quantum efficiency with increasing aluminum. For example, at 7600 Å, the threshold current densities were about 5000 A/cm^2, instead of the expected 2000 A/cm^2. No obvious metallurgical flaws could be found in these lasers, which would explain their relatively poor performance. We suspect that the strains incorporated in these structures are at least partly responsible for the above anomalous behavior, and means of reducing these have to be found to improve these devices.

Several studies were made to determine the power limit achievable under cw operation by changes in the effective diode area. These studies were conducted with material emitting between 8100 and 8400 Å,

TABLE IV

Effect of Stripe Width on Threshold Current

Stripe Width (μm)	13	50	100
I_{th} (A)	0.3	0.59	0.91
J_{th} [Assumed full planar confinement]	4130	2100	1600
J_{th} (With current spread)	3000 (18 μm)	1900 (55 μm)	1520 (105 μm)

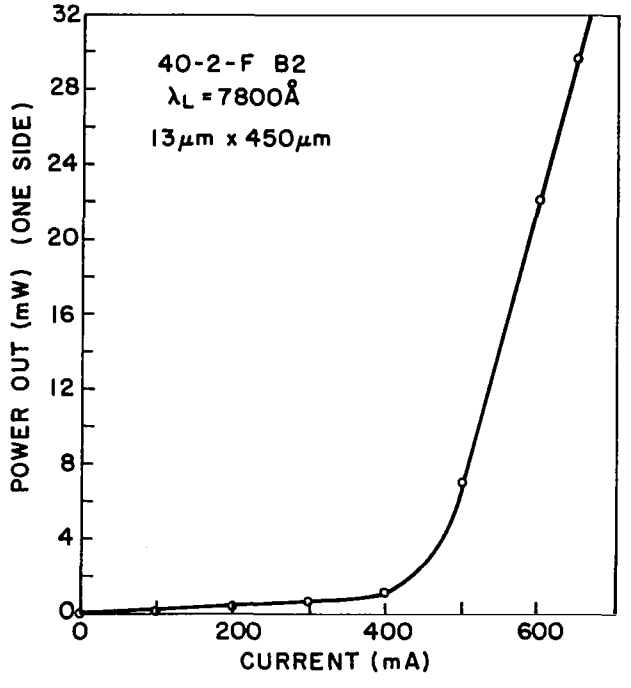

Figure 71. CW power output vs. diode current for laser emitting at 7800 Å.

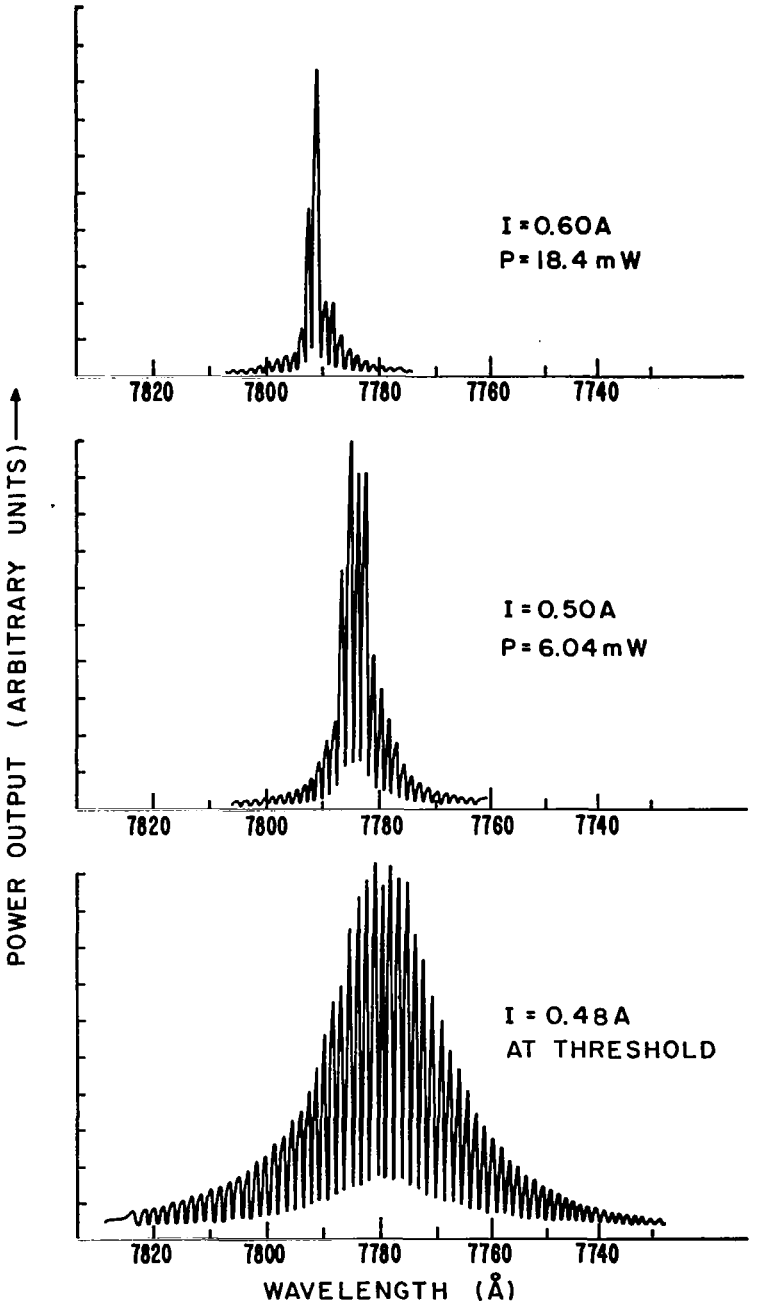

Figure 72. CW spectral emission as a function of current for laser with the power curve shown in the previous figure.

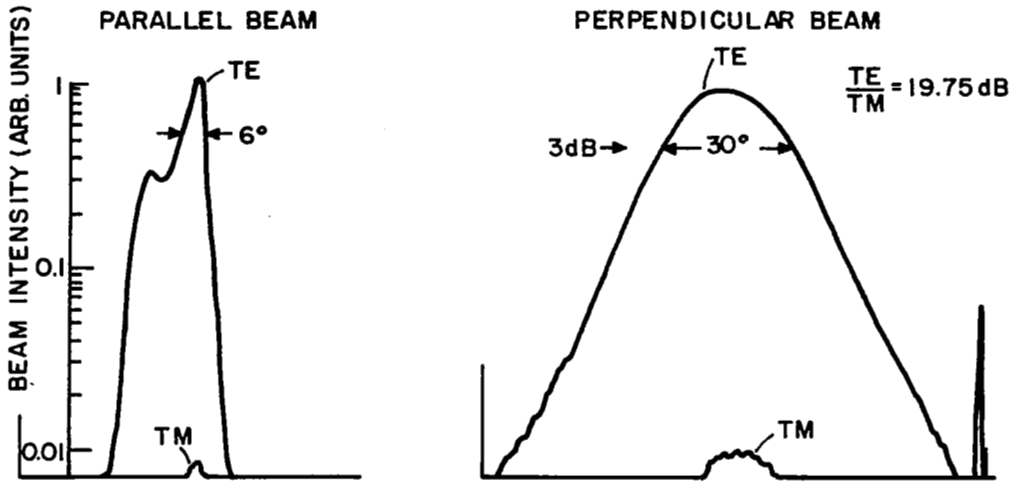

Figure 73. Far-field pattern of cw laser emitting at ∿7800 Å.

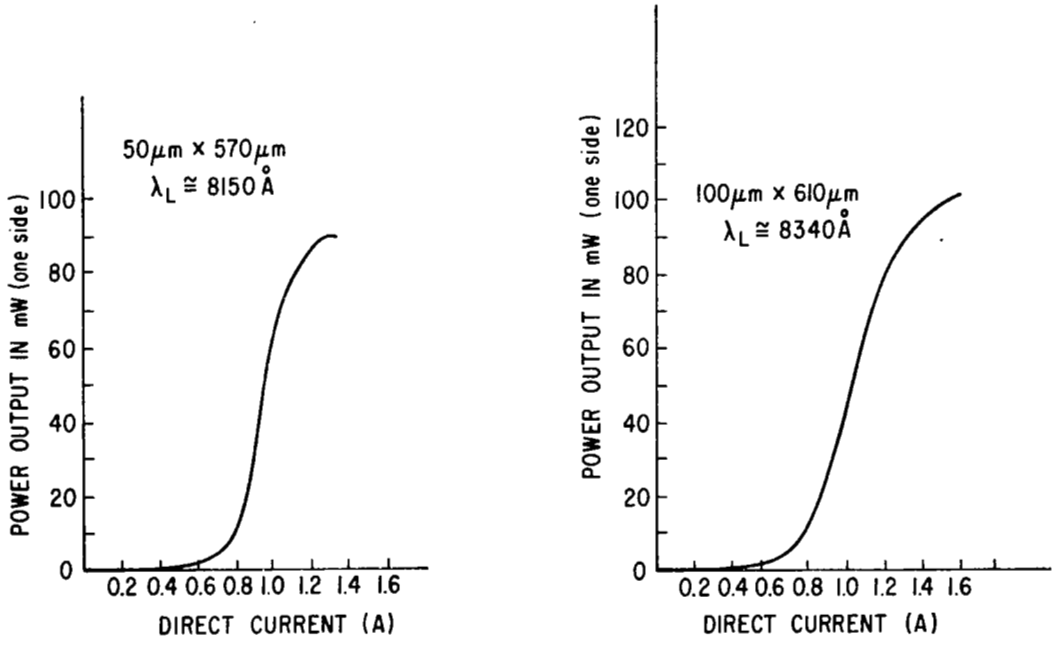

Figure 74. Power emission from one laser facet as a function of direct current for two lasers selected from different wafers operating at room temperature.
(a) Diode with 50-μm-wide stripe contact;
(b) diode with 100-μm-wide stripe contact.

using the SiO_2-isolation stripe-contact process with stripe widths of 13, 50, and 100 μm. Figure 74(a) shows the current dependence of the light emitted by a diode having a 50-μm stripe width. The cw threshold current is 0.76 A and the cw power output peaks at 90 mW (one side) at a current of 1.3 A. The saturation in the power output is due to the increase with current of the junction temperature and the consequent increase in the threshold current density. The position of the maximum in the power output depends on the thermal and electrical resistance of the diode, and on the threshold current density dependence on temperature (ref. 52).

Somewhat higher peak power levels are obtained with wider stripes. Figure 74(b) shows the cw power output from one facet of a 100-μm-wide stripe diode as a function of direct current. Here the power output saturates at 100 mW (200-mW total emission) at a current of 1.6 A.

D. Reliability of Room-Temperature CW Lasers

Power reduction under operating conditions of cw lasers can occur as a result of three basic factors:

(1) Increase in diode electrical and/or thermal resistance.
(2) Facet damage.
(3) Changes in the bulk of the device due to the formation of nonradiative centers.

The first problem is easily controlled by appropriate care in diode fabrication and contact procedures and is not a problem in present diodes. The other two areas are discussed below.

1. Facet Damage. - Facet damage can occur if the diode is operated under conditions where moisture is allowed to condense on the laser facet, and is accelerated if dust particles settle on the facet. Figure 75 shows the appearance of the facet after long-term operation in the laboratory with the facet unprotected. Water condensation on the facets can occur, if the heat sink is maintained a few degrees below room temperature.

Another mode of failure occurs if the power output is excessive, independent of the above ambient conditions.

It is known that facet damage in diodes operated in the pulsed mode can occur when the optical flux density is sufficiently high (ref. 53). The power level at which damage occurs decreases with increasing pulse length (ref. 54). It is of great importance, therefore, to determine whether the power levels described above for room-temperature cw lasers can lead to laser degradation caused by facet

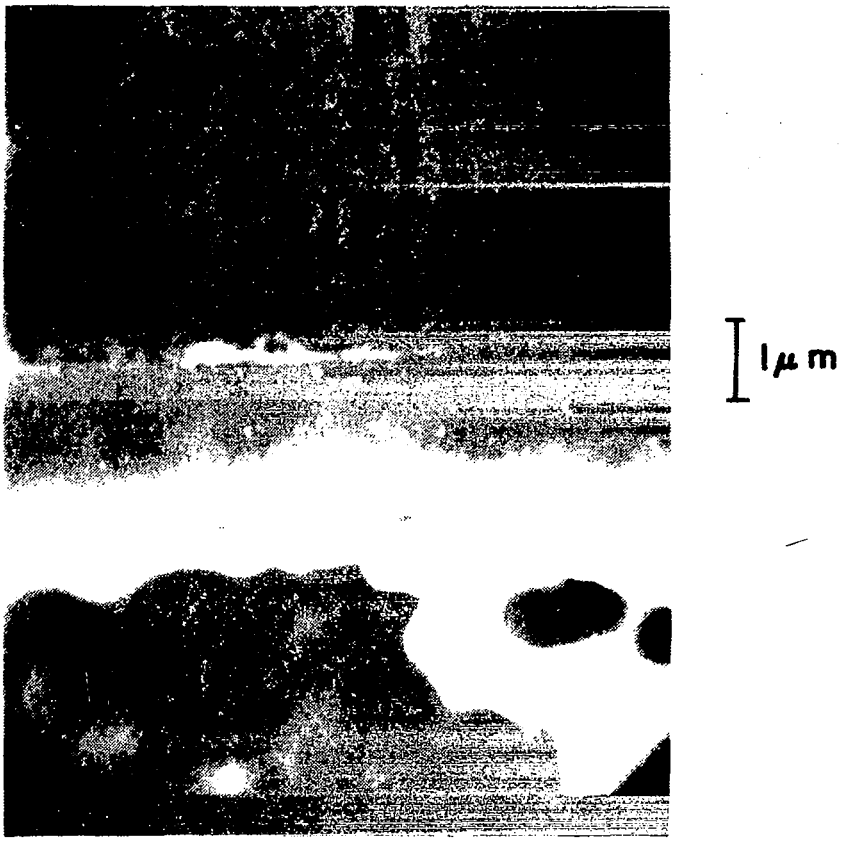

Figure 75. Scanning electron micrograph of cw laser diode after 900 hr of operation, showing facet damage. The diode was operated in an unprotected laboratory ambient.

damage. These facet damage effects were studied in the 13- and 50-μm-wide stripe diodes, where damage could be induced within relatively short periods of time (order of 1 hr) when the diodes were operated at their peak optical output. The diode facets were uncoated, and the damage experiments were conducted in a normal laboratory ambient with the heat sink temperature kept constant at ∿20°C.

We consider, for example, facet damage results obtained with the 50-μm-wide stripe laser initially emitting 90 mW from one facet. The power output gradually decreased until, at one quarter of its initial value, the damaged region on the facet shown in Fig. 76 was observed. The damaged region is 25 μm wide and occurs in the central region under the stripe contact where the current and, hence, the power emission are at a maximum. Facet damage could not be induced under similar test conditions in less-efficient diodes operating at the same current of

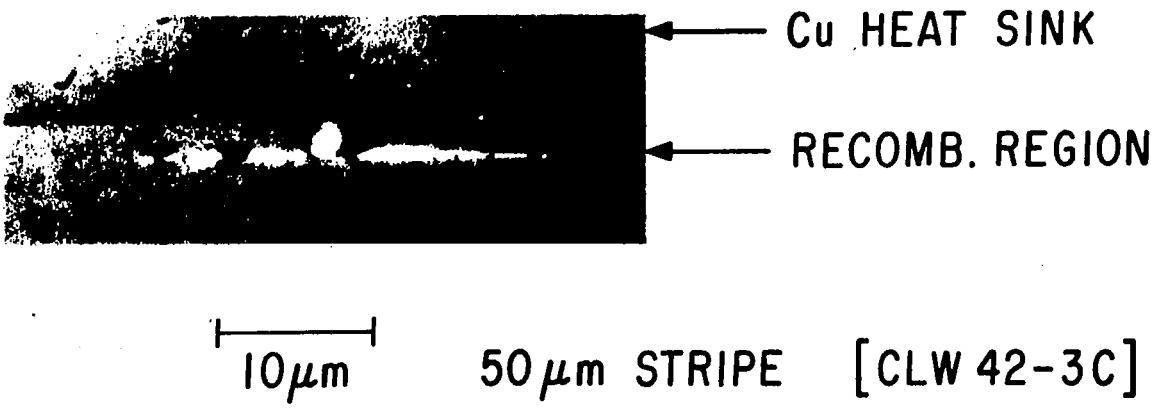

Figure 76. Optical micrograph of the facet damage following operation at the 90-mW emission level from a 50-μm-wide stripe diode. The extent of the damaged region is less than the full width of the stripe.

1.3 A (for example, diodes emitting only 70 mW instead of 90 mW), suggesting a correlation between facet damage and the power emission level. Other observations were consistent with this hypothesis. No facet damage was induced in the 100-μm-wide stripe diodes where a higher power level (110 mW) was emitted from a region about twice as wide.

The following comments are relevant to the facet damage data:

(1) The power level at which damage will occur will depend on the extent of the radiation spread in the plane of the junction (effective diode width) and in the direction perpendicular to the junction (radiation confinement). As shown by near-field studies, the effective lasing width of the 13-μm stripe diodes was about 20 μm, while that of the 50-μm stripe diodes was about 60 μm. Therefore, in the specific structures discussed, failure occurred at levels of about 1.5 mW per mm of effective diode width. (Considering the high field intensity to spread over 1 μm in the direction perpendicular to the junction, the optical power density is $\sim 1.5 \times 10^5$ W/cm^2.)

(2) It is known that coatings which reduce the field intensity at the laser facet increase their damage limit in the pulsed mode (ref. 55). A similar improvement is expected in cw laser diodes.

The damage results described above are phenomena which occur in a relatively short time period. It is evidently of practical interest to determine the power level which can be sustained for long-term

operation (>1000 hr). Such tests were conducted with the diodes operating in a dry air atmosphere to eliminate long-term effects due to moisture. Both 13-μm-wide stripe lasers and 50-μm-wide lasers were subjected to extended life tests at power levels of about one-third the maximum attainable from a given device. The output from one facet as a function of operating time at a *fixed current* is shown in Figs. 77(a) and 77(b). It is seen that the 50-μm-wide stripe diode is emitting an average of 33 mW from one facet (66 mW total) for more than 1000 hr with a drive current of 1 A. The 13-μm-wide laser is emitting between 6 and 7 mW for more than 2000 hr. (The fluctuations in the power output seen in Fig. 77 are believed to be related to slight changes in the ambient temperature, which reversibly affect the threshold current.) It is clear, however, that insufficient data are available to preclude stable operation at even higher operating power levels.

2. Bulk Degradation Effects. - The resistance to gradual degradation of laser diodes is known to be strongly influenced by metallurgical factors, several of which have already been identified, such as dislocations, impurity precipitates, and contaminants (refs. 56 and 57). We now discuss two additional factors that are shown to exert a strong influence on the life of cw laser diodes. These are: (1) the nature of the zinc diffusion, which is frequently used to improve the performance of ohmic contacts or to provide isolation in stripe contact geometries, and (2) mechanical saw damage to the laser sidewalls.

The effect of excessive zinc diffusion on diode life was studied in the following type of experiment. The p-surface of the wafer was protected with SiO_2 except for 13-μm-wide stripe windows. Zinc was next diffused to a depth of 1 μm, using an excess zinc source in a sealed ampoule. The diffusion front, as revealed by etching, was located at the boundary between the p-wall and the cap layer. It is, however, possible that some zinc (or associated lattice defects), not revealed by etching, penetrates into the "p-wall" or even into the recombination region. This would be significant here since the p-wall had a thickness of only 0.5 to 0.8 μm, which makes the latter possibility more likely. Control sections of the same wafer were processed without diffusion. Both sections of the wafer were then metallized and assembled for operation by mounting on copper heat sinks.

A comparison of the life of the diffused and the nondiffused diode, shown in Fig. 78, reveals a large difference. Diodes were operated at 500 mA, which was below lasing threshold, in order to make the emission more directly dependent on internal quantum efficiency. Note that the diffused diode degraded to half its initial output in 40 hours, while the nondiffused diode remained unchanged.

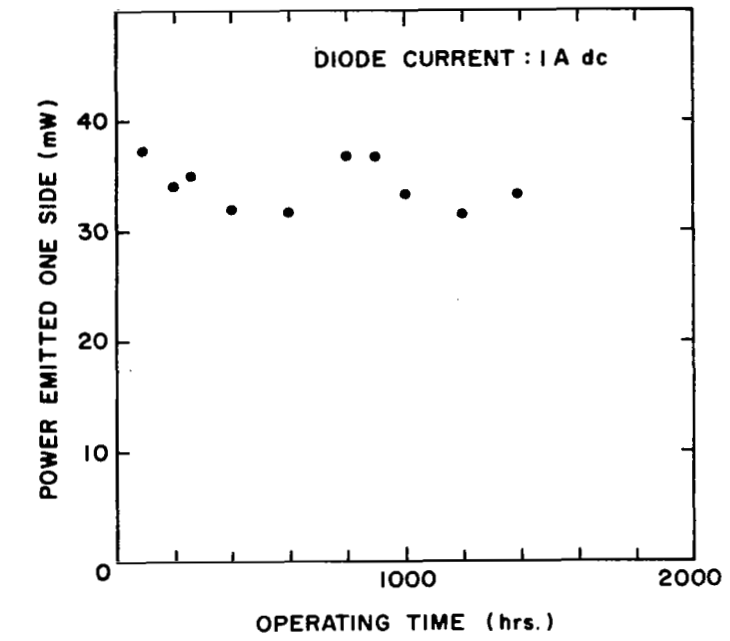

(a)

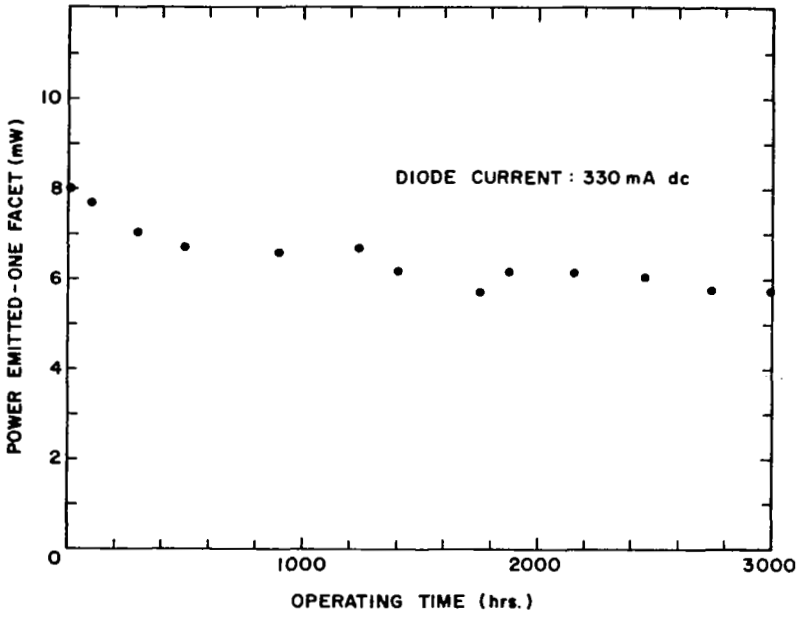

(b)

Figure 77. Power emitted from one facet of cw (AlGa)As lasers operating at room temperature at *constant current*. (a) Diode with 50-μm-wide stripe operating at a drive current of 1 A; (b) diode with 13-μm-wide stripe operating at 0.33 A. The fluctuations in the power output are partially due to slight changes in the ambient temperature, which reversibly changes the threshold current density.

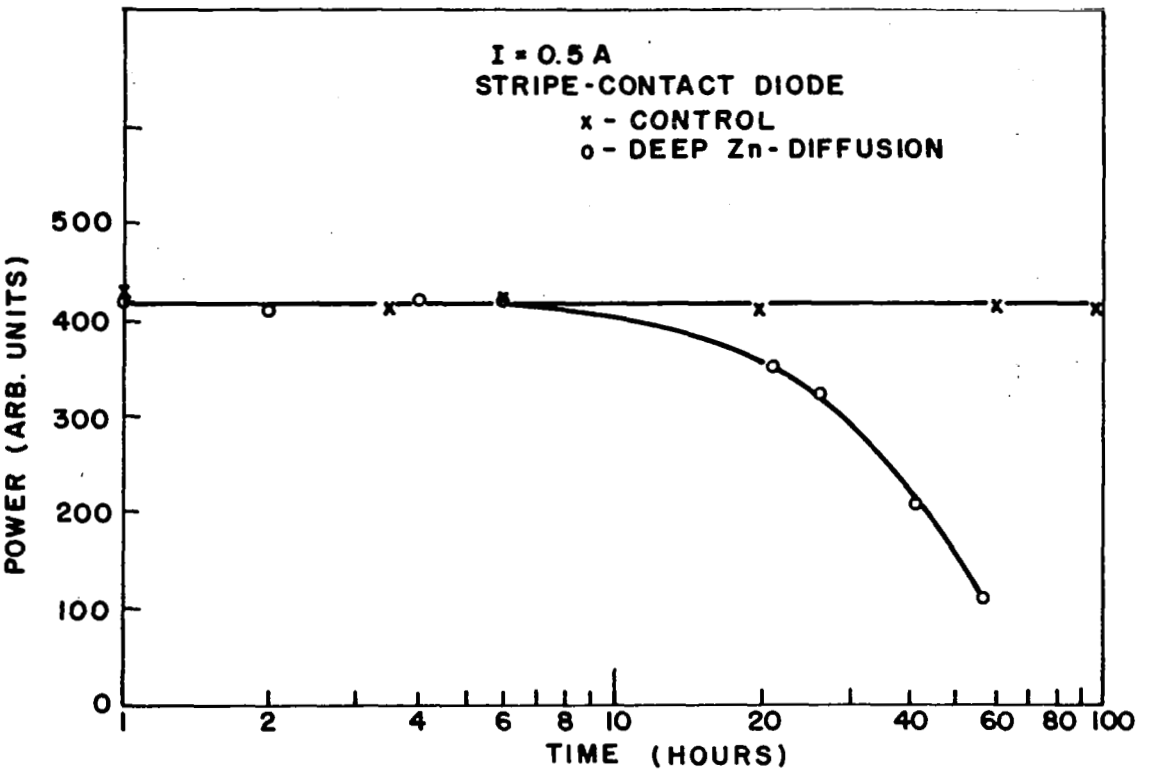

Figure 78. Power output as a function of time for two diodes fabricated from the same wafer but processed differently. One diode had a deep zinc diffusion (∿1 μm) from an excess zinc source prior to ohmic contact application, while the other diode was not diffused.

It is important to note that stable operation in the lasing state was consistently obtained not only for the undiffused diodes, but also for diodes similarly diffused with *shallow* diffusion depths; i.e., not more than a fraction of a micrometer. For example, Fig. 79 shows the nearly similar cw power output as a function of current of a shallow-diffused diode before and after 2000 hours of continuous operation (at which point the test was stopped). It appears, therefore, that the zinc diffusion front (including the attendant disruption of the lattice) must be kept away from the recombination region and even the p-wall to ensure reliable long-term operation.

It is probable that the high surface concentrations of zinc used for the present experiments cause formation of defects, including vacancies, which enhance the degradation rate. However, some of these zinc diffusion-induced effects may enter, regardless of the diffusion

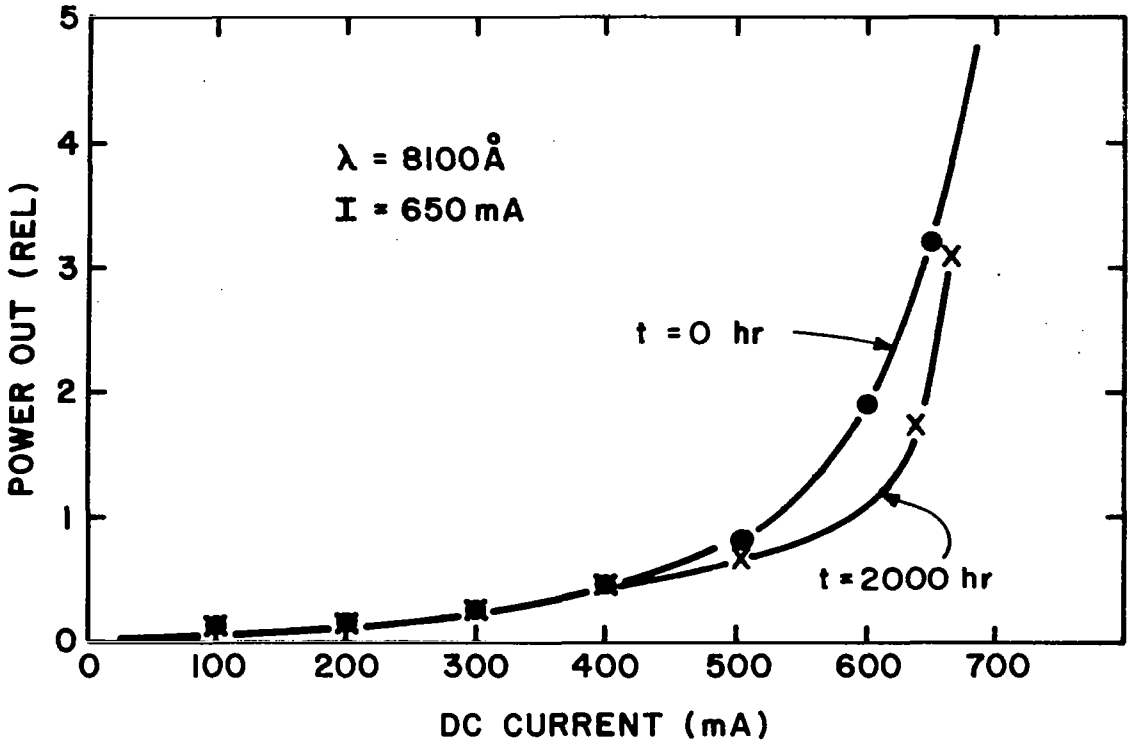

Figure 79. Power output vs. current of a cw laser diode with a shallow zinc diffusion (under 1 μm; i.e., not affecting the recombination region) before and after 2000 hr of continuous operation. The diode was operated in a dry air atmosphere to prevent facet damage.

process, if the diffusion front is too close to the recombination region. This will, of course, be the main problem in diffusion-isolated structures where careful control and possibly different diffusion processes are required.

The second major aspect affecting reliability concerns the method of defining the diode edges; i.e., the nature of the sidewalls. Diodes having sawed sides instead of the planar stripe-contact structure described above are much more susceptible to gradual degradation. This was shown by comparisons of diodes formed by the two methods, using the same wafer. Figure 80 shows the results of a representative test conducted using a sawed-side diode cut from the same wafer that yielded the reliable diode shown in Fig. 79. Figure 80(a) shows the power output as a function of current of the diode operating cw at the start of the test and after short time operating intervals. The rapid degradation

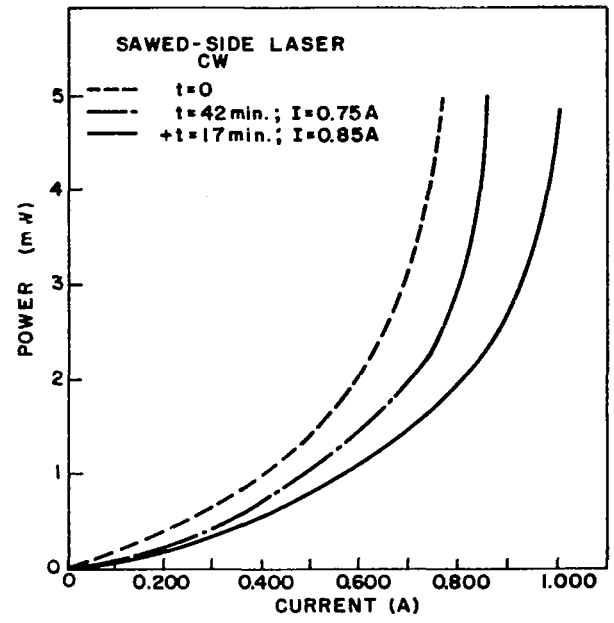

(a)

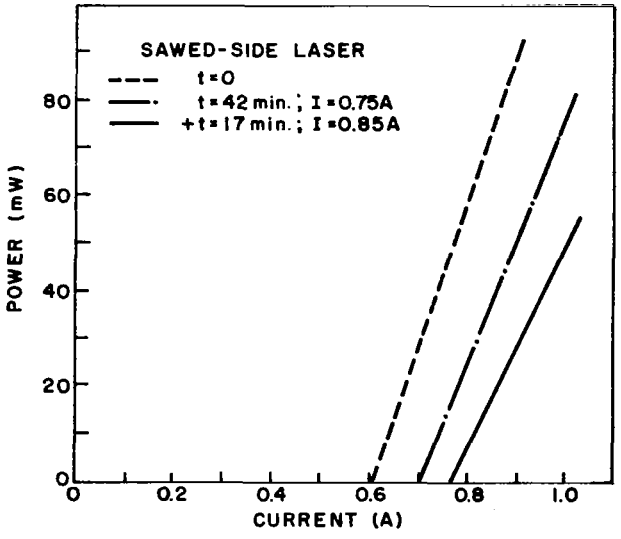

(b)

Figure 80. Power output vs. current for a broad area, sawed side, diode operating cw. The diode degradation is evident as shown, both in the dc mode (a), and the pulsed mode (b), by the displacement of the curves after an initial 42 min, followed by an additional 17 min at a higher current made necessary by the increase in the threshold current. The operating current density was $\sim$1600 A/cm^2.

within one hour is startling. No facet damage was observed. The fact that true bulk changes are occurring is confirmed by measurements of the pulsed power-current curves shown in Fig. 80(b). Note the increase in the threshold current and the decrease in the differential quantum efficiency, traditional features of gradual degradation in the absence of facet damage. The diode near-field emission became increasingly spotty in the course of operation, being particularly reduced at the diode sidewalls. Since this diode was operated at a current density ($\sim$1875 A/cm^2) equal to or lower than that prevailing in the stripe-contact lasers, and since we expect that the operating temperature is no higher than that of stripe-contact lasers, we believe that the rapid degradation is a consequence of the presence of saw damage at the diode edges. The effect of saw damage can be explained by several factors, including the in-diffusion of contaminants or more probably, the multiplication of dislocations in the highly disturbed material near the diode surface.

VI. EFFECT OF HYDROSTATIC PRESSURE ON HETEROJUNCTION LASER CHARACTERISTICS*

A. Introduction

Although the lattice parameters at the growth temperature of 800 to 900°C are equal at the $Al_xGa_{1-x}As$-$Al_yGa_{1-y}As$ heterojunction interfaces, they differ significantly at room temperature because of the different thermal coefficients of expansion of GaAs and (AlGa)As. The impact of strain takes on increasing importance with the increasingly Al-rich layers needed to shift the emission into the visible where the high Al-content (AlGa)As layers are grown on much thicker GaAs substrates. Since the lattice parameter of (AlGa)As is slightly larger than that of GaAs, the thin epitaxial layer is under compression. While it is suspected that these strained layers contribute to inefficient lasers, no definitive data were available.

The work described in this section was designed to explore the quantitative effect of stress on the (AlGa)As diode properties in the lasing state. While the use of uniaxial stress is attractive, it is limited because the diode material is very brittle, and, therefore, the diode easily shatters if the stress is not quite uniform on the diode surface. Hydrostatic measurements, on the other hand, require more complex equipment but are convenient because no material damage occurs, if the diodes are properly mounted with a soft solder such as In.

The equipment used for the measurements is described in Appendix I. The diodes were mounted on metallized ceramic strips with long copper leads for electrical connections. The diodes were test-pulsed at room temperature using a pulse length of ∿150 nsec and a repetition rate of ∿500 Hz. The duty cycle was low enough to ensure that the diode characteristics were not affected by heating during operation.

The Al concentration in the recombination region of the diodes tested ranged from ∿18% ($\lambda_L \tilde{\gtrsim}$ 7700 Å) to less than 1% ($\lambda_L \tilde{\gtrsim}$ 8900 Å) in order to explore the effect of the stress on diodes having different (AlGa)As concentrations.

*The experimental work described in this section was performed at Yeshiva University by Y. Juravel and P. M. Raccah.

B. Experimental Results

1. GaAs Heterojunction Lasers. - Both double heterojunction (DH) and LOC lasers were tested with essentially GaAs in the recombination.* The LOC laser was asymmetrical; i.e., it had a small refractive index step at the n-n heterojunction ($\Delta n \gtrsim 0.02$) and much larger one at the other (p-p) heterojunction, while the DH laser was symmetrical ($\Delta n \gtrsim 0.1$).

Figure 81 shows the power output curve of the DH laser as a function of the diode current for various values of hydrostatic pressure. (The atmospheric pressure measurements were repeated at the end of the stress experiment to establish that no irreversible effects were introduced by the hydrostatic stress.) Figure 81 shows a small reversible threshold increase with pressure, which can be expressed in a normalized form by $\Delta I_{th}/I^{\circ}_{th} \gtrsim 0.018$/kbar, using the initial threshold current, I°_{th}, as the normalizing quantity.

The shift in the dominant spectral line due to axial modes above threshold is shown in Fig. 82 as a function of stress. Two current levels were studied, and Fig. 82 shows that the shift of the emission is 0.99×10^{-2} eV/kbar at I = 0.7 A, and 1.03×10^{-2} eV/kbar for the line at 0.775 A, a difference which is not considered significant. As we will see below in greater detail, the above dominant axial mode line shift with pressure very nearly follows the increase in the band-gap energy with pressure, although *individual* mode lines vary far less with pressure (see below).

Turning to the asymmetrical LOC laser, Fig. 83 shows its power emission as a function of current at atmospheric pressure, 1 kbar and 1.884 kbars. The laser threshold is somewhat more stress sensitive than that of the DH laser, but still small, $\Delta I_{th}/I^{\circ}_{th} = 0.022$/kbar.

The shift of the spontaneous emission peak $h\nu_{sp}$ was measured below the lasing threshold, and the spectral lines were followed above threshold with as many of the lines as possible studied in the pressure range where they remained discernible. Figure 84 shows the increase with pressure of the spontaneous emission peak $h\nu_{sp}$ in the range between atmospheric pressure and 1.88 kbars, giving a value of $\Delta h_{sp}/\Delta p = 1.139 \times 10^{-2}$ eV/kbar. Figure 85 shows the shift with pressure of the axial mode lines. The *individual* line shift (0.27×10^{-2} eV/kbar) is considerably less than the spontaneous emission peak. However, consistent with Fig. 82, Fig. 85 shows that the "center of gravity" of the

*A small amount of Al could have been inadvertently introduced into the recombination region by transfer from melt to melt during LPE growth.

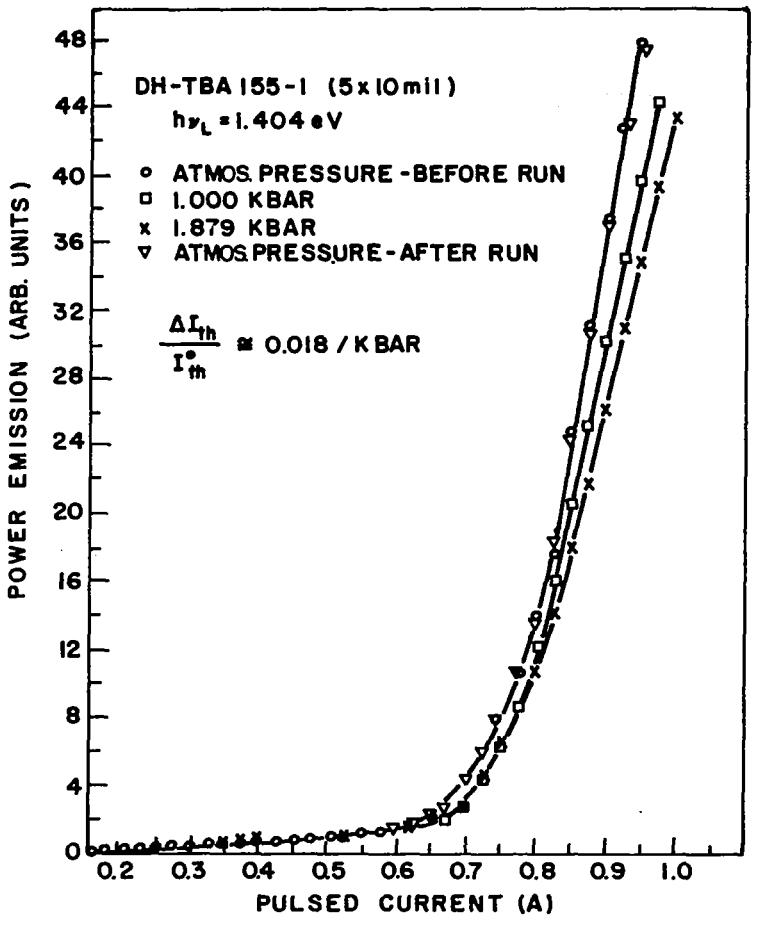

Figure 81. Power emission as a function of current under pulsed operation of a double heterojunction laser diode with GaAs in the recombination region as a function of hydrostatic pressure. The curve for atmospheric pressure was repeated at the end of the test to confirm the fact that no permanent diode changes were introduced by the applied stress.

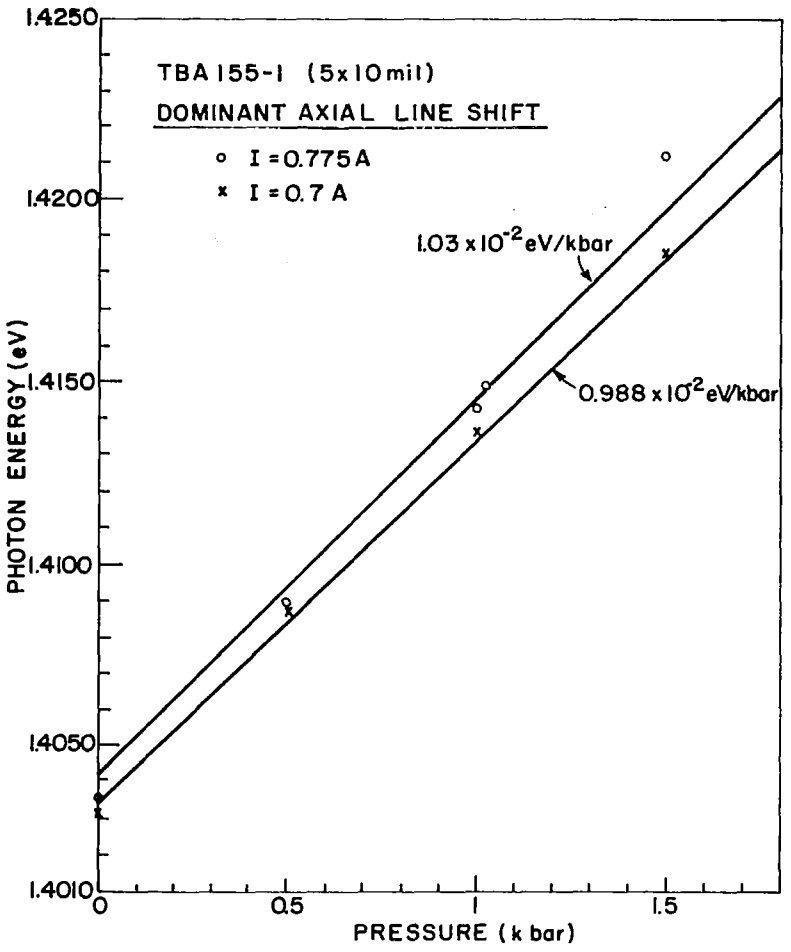

Figure 82. Dependence of the energy of the dominant axial line on hydrostatic pressure for the DH laser with GaAs in the recombination region. The measurements were at two different current levels above lasing threshold, I = 0.775 A and I = 0.70 A, with essentially similar results.

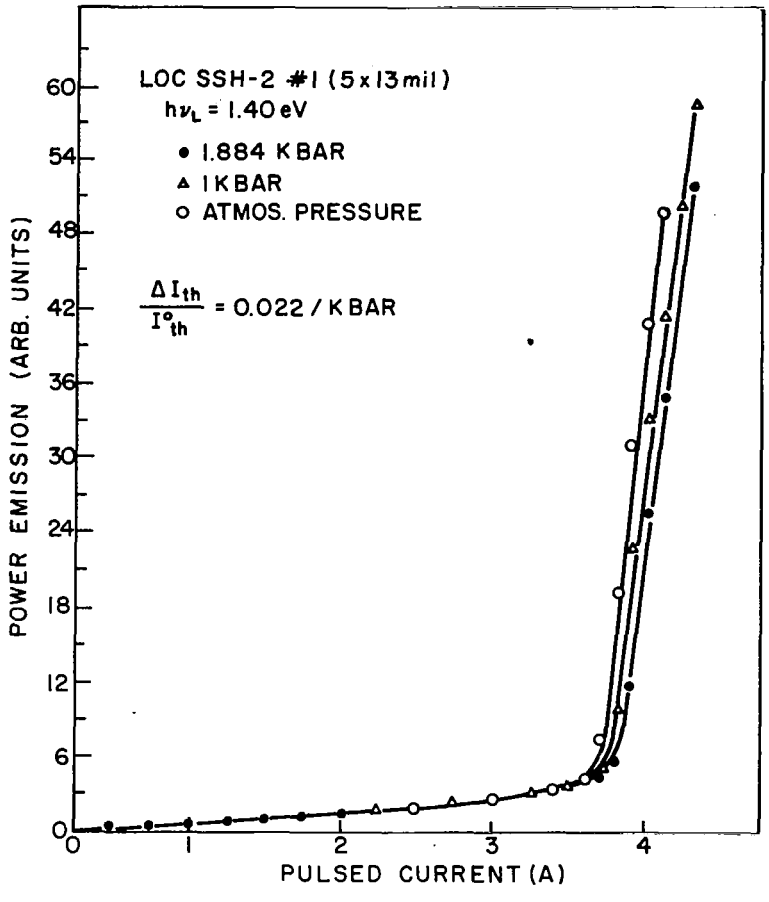

Figure 83. Power emission vs. current for an asymmetrical LOC laser with GaAs in the recombination region.

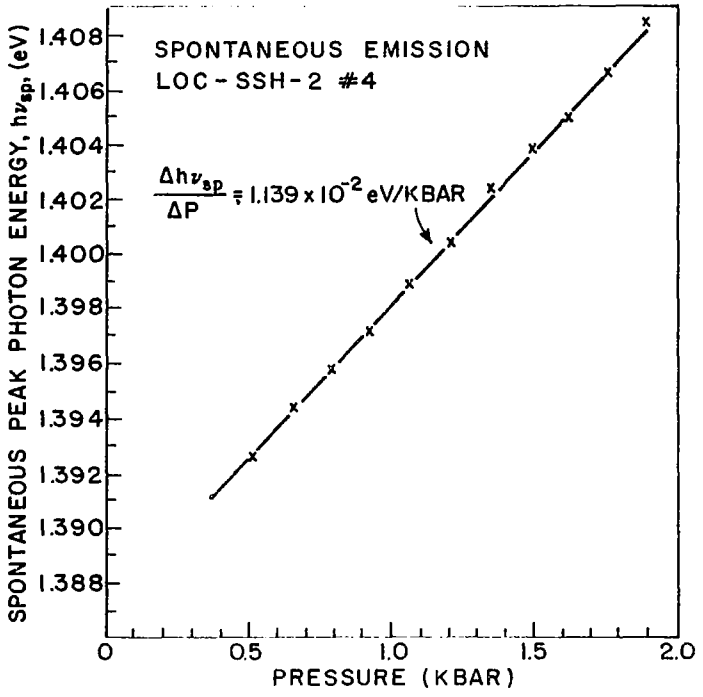

Figure 84. Shift of the spontaneous emission peak with hydrostatic pressure for a LOC laser with GaAs in the recombination region.

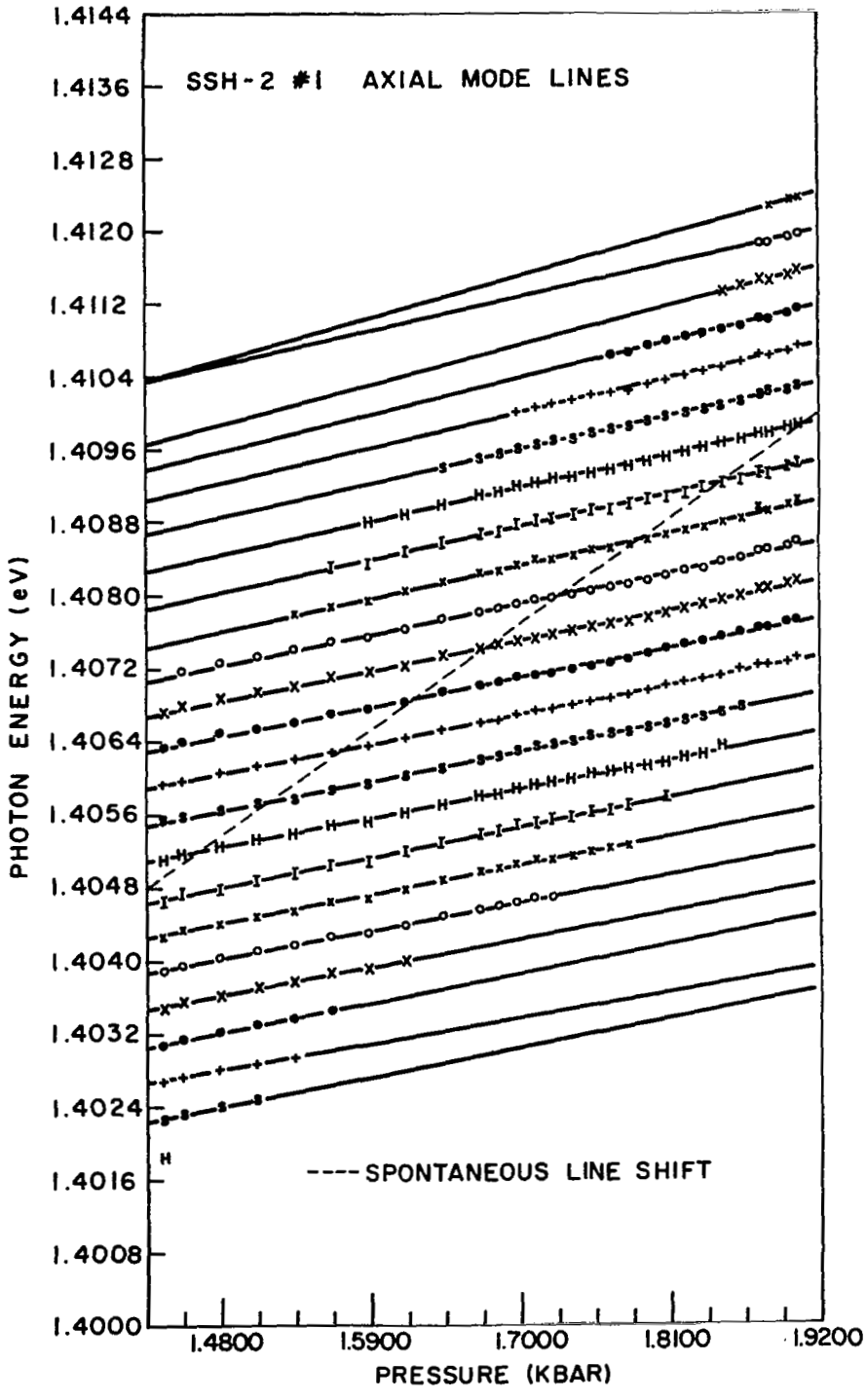

Figure 85. Shift of the axial mode lines with increasing pressure compared with that of the spontaneous emission peak. As the pressure increases, some of the mode lines disappear while new ones appear. Note that the spontaneous peak shift appears to follow the center of the mode line energy distribution.

modal line energy distribution increases at a rate comparable to that of the spontaneous line shift, as can be seen from the superimposed dashed line.

2. (AlGa)As Heterojunction Lasers. - The stress-dependence of the threshold current of a DH laser with $Al_{.1}Ga_{.9}As$ in the recombination region (λ_L = 8000 Å) is shown in Fig. 86. The relative change of I_{th} with stress is considerably larger than that of the GaAs heterojunction lasers,

$$\Delta I_{th}/I^{\circ}_{th} = 0.078/\text{kbar} \qquad (18)$$

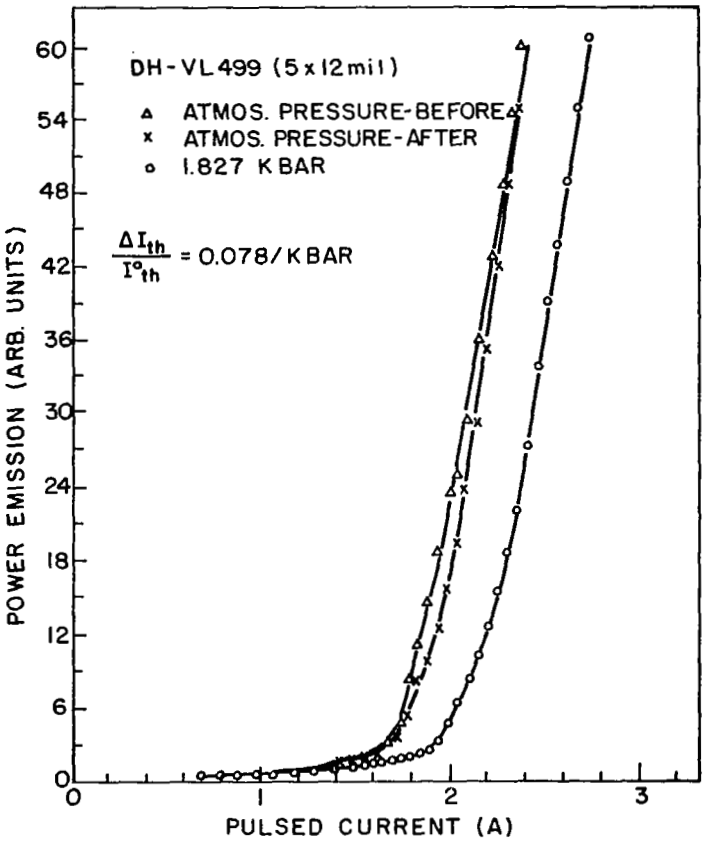

Figure 86. Power emission vs. current for a DH laser with $Al_xGa_{1-x}As$ in the recombination region ($x \cong 0.1$). The atmospheric pressure curve was repeated at the end of the stress equipment.

Figure 87 shows power output vs. pressure curves of the laser with $Al_{.18}Ga_{.82}As$ in the recombination region (λ_L = 7720 Å). The measurements of this diode were extended over a wider pressure range than the other devices, reaching 5 kbars, and, as shown in Fig. 88, the threshold increase with pressure remains nearly linear in the range studied, and can be approximated by

$$\Delta I_{th}/I^{\circ}_{th} \approx 0.11/\text{kbar} \tag{19}$$

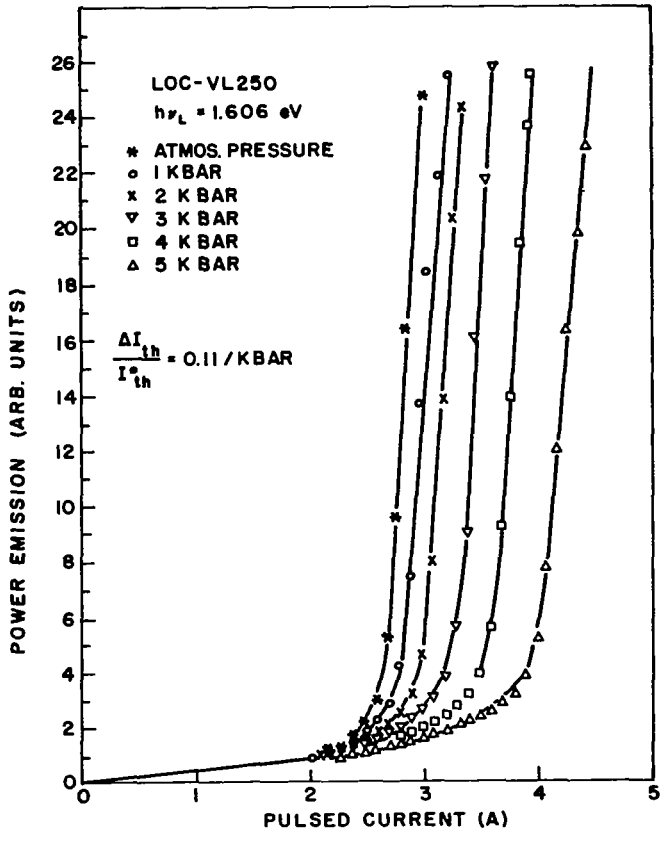

Figure 87. Power emission vs. current for various pressure values for a LOC diode with $Al_{.18}Ga_{.82}As$ in the recombination region.

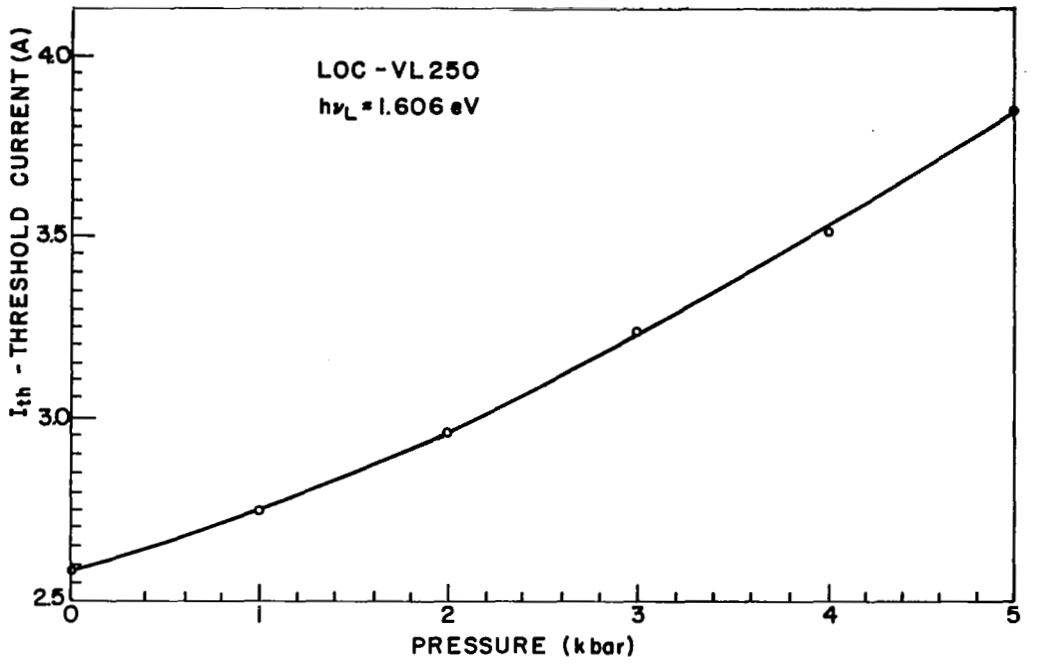

Figure 88. Threshold current as a function of pressure as deduced from the data shown in Fig. 87. (LOC laser with $Al_{.18}Ga_{.82}As$ in the recombination region.)

C. Discussion

The most important new result from the above-described experiments is the observation that the stress-dependence of the threshold current increases with increasing Al content in the recombination region. There are two basic possible factors explaining the threshold increase: (1) A reduction in radiation confinement with increasing pressure for a given diode geometry and (2) a change in the internal laser dynamics which is affected by additions of Al to the recombination region. For example, the transfer of electrons from the Γ to the X conduction band minima.

The first effect is not believed to be significant on the basis of the comparison of the DH and LOC GaAs heterojunction lasers tested. The most probable cause for the reversible reduction of the radiation confinement would come from a reduction in the refractive index step at one or both of the heterojunctions defining the optical cavity. The fact that the threshold change with pressure of the asymmetrical LOC diode with weak confinement was comparable to the change observed for the strongly confined DH diode suggests that no significant reduction occurs in the refractive index step with increasing pressure, which would lead to greatly increased threshold currents with pressure. In

the case of the (AlGa)As heterojunction structures tested there is no reason to believe that the observation made for the GaAs heterojunction structures is not applicable; i.e., we expect no significant loss of radiation confinement, particularly since the (AlGa)As diodes tested contained reasonably high heterojunction barriers comparable to those in the GaAs DH unit.

Having excluded the first effect, we are left with the second effect. It is possible that trapping states exist in the material, the density of which increases with increasing Al content, and that their effectiveness increases with pressure. However, at this time no additional data exist which would allow these hypothetical states to be better defined. It is possible that these states are associated with the six <100> indirect conduction band minima, and since the direct bandgap at $\bar{k} = 0$ increases with hydrostatic pressure while the indirect bandgap decreases, the effect of states associated with the indirect bandgap minima would tend to become increasingly important with increasing Al content in the recombination region. Additional work in progress with higher Al-content diodes should help to elucidate this point. We note that deep states that affect the laser behavior were postulated on the basis of uniaxial stress work, which showed that (AlGa)As heterojunction diodes became increasingly susceptible to uniaxial stress-induced increases in threshold (ref. 61).

We wish to emphasize, however, that other factors affecting the laser dynamics could be more relevant. Additional experimental and theoretical studies are expected to elucidate the laser properties under stress.

In summary, it is evident that stresses can adversely affect the performance of (AlGa)As heterojunction lasers, with proportional severity as the Al content increases. Therefore, it is desirable that construction technologies be developed which minimize these stresses to permit improved laser diodes emitting closer to the visible spectral range.

Turning our attention to the shifts in the spontaneous emission peaks and of the axial mode lines, we find general agreement with earlier data obtained with homojunction lasers. The value of 1.139×10^{-2} eV/kbar obtained from Fig. 84 for the shift in the spontaneous emission line is generally accepted as representative of the shift in the bandgap energy of GaAs. Other values in the literature are close, for example, 1.09×10^{-2} eV/kbar (ref. 58) (measured at 200°K), and 1.1×10^{-2} eV/kbar (ref. 59).

The shift in the energy distribution and individual energy values of the axial lines with pressure is explained by two effects:

(1) The dominant intensity line or "center of gravity" shift is expected to follow the bandgap energy shift with various modes on the low energy side disappearing, while new lines on the high energy side appear as is indicated in Fig. 85.

(2) The individual axial line width is the result of a change in the refractive index with pressure for a given energy value due to the bandgap energy increase

$$\frac{1}{\lambda}\frac{d\lambda}{dp} = -\frac{1}{h\nu}\frac{d(h\nu)}{dp} = \frac{\frac{1}{L}\left(\frac{dL}{dp}\right) + \frac{1}{n}\left(\frac{dn}{dp}\right)_{\lambda}}{\left[1 - \frac{\lambda}{n}\left(\frac{dn}{d\lambda}\right)_{p}\right]} \tag{20}$$

where L is the laser length and n is the refractive index.

In the above equation, the length change with pressure is small $\left(-0.43 \times 10^{-3}(\text{kbar})^{-1}\right)$ (ref. 60), while the term in the denominator is ~ 1.5, leaving the change of n with pressure the dominant effect. From the experimental value obtained from Fig. 85 for the shift in mode energy with pressure (0.27×10^{-2} eV/kbar), we obtain

$$\frac{1}{n}\frac{dn}{dp} = -0.33 \times 10^{-2}\ (\text{kbar})^{-1} \tag{21}$$

This value, measured for the first time at room temperature, falls within the range of previously measured quantities (refs. 59 and 60), (below room temperature) of $0.4 \pm 0.1 \times 10^{-2}$ eV/kbar.

VII. CONCLUSIONS

Two alloy systems, (AlGa)As and (InGa)P, have been studied for their properties relevant to obtaining laser diode operation in the visible region of the spectrum. (AlGa)As was prepared by liquid-phase epitaxy (LPE) and (InGa)P was prepared both by vapor-phase epitaxy (VPE) and by liquid-phase epitaxy. Various schemes for LPE growth were applied to (InGa)P, one of which was found to be capable of producing device material. However, as this method is less advanced, and in many ways less suitable than the VPE method, all the InGaP device work was done using vapor-phase epitaxy.

The most successful devices were fabricated in (AlGa)As using heterojunction structures. At room temperature, the large optical cavity (LOC) design has yielded devices lasing in the red (7000 Å). However, because of the relatively high threshold due to the basic band structure limitation in this alloy, practical laser diode operation is presently limited to about 7300 Å. At liquid-nitrogen temperature, practical continuous-wave operation has been obtained for the first time at a wavelength of 6500 to 6600 Å, with power emission in excess of 50 mW. The lowest pulsed lasing wavelength is 6280 Å. At 223°K, lasing was obtained for the first time at 6770 Å, but with high threshold currents.

Despite the achievement of the shortest laser diode wavelength ever achieved, the research conducted on (InGa)P epitaxial materials using electroluminescence, photoluminescence, and cathodoluminescence leads to the conclusion that several major problems limit the use of this alloy for practical laser diodes.

(1) Heterojunction structures are impractical because of the metallurgical limitations inherent in the lattice parameter mismatch which is much larger with composition change than in (AlGa)As. Thus, efficient room-temperature lasing in the visible is difficult to achieve.
(2) While electron-beam-pumped lightly doped material shows that epitaxial (InGa)P is relatively efficient in the direct portion of the alloy composition range, the laser diodes fabricated have high threshold current densities and low differential quantum efficiencies. This is believed due to the difficulty of incorporating the requisite high dopant density without introducing an unacceptably high defect density. The dopant-related defects are intimately related to the existing flaws formed in the process of epitaxial growth. Despite the difficulties encountered in fabricating (InGa)P laser diodes, this program has resulted in diodes

emitting at 77°K at 6420 Å in material deposited on GaAs substrates, and 5980 Å in material deposited on GaP substrates. The latter result is the shortest diode laser wavelength ever achieved.

(3) Because of the relatively deep acceptor ionization energies, considerable freeze-out occurs at low temperatures. This results in poor power conversion efficiencies compared with those of (AlGa)As or GaAs devices.

The latter portion of the program, as described in this report, has been concerned with obtaining room-temperature cw operation from diodes emitting as close to the visible portion of the spectrum as possible. This phase of the program has resulted in several new achievements, in a spectral range extending to wavelengths as short as 7800 Å. Major factors affecting reliability have, for the first time, been identified and eliminated, leading to power emission values as high as about 30 mW from one laser facet for stable operating periods in excess of 1000 hr (with the limit not yet reached).

Stable cw operation at room temperature requires very low threshold current densities, and we have found that the required threshold values have been extremely difficult to achieve for lasing wavelengths much below ∿7800 Å, although they should be theoretically achievable.

Experimental studies using uniaxial stress experiments (performed at Yeshiva University) have suggested that the laser threshold is anomalously increased by elastic stress, thus, providing one possible reason for the excessive increase in threshold of diodes with aluminum increase. Future efforts to realize the potential of the (AlGa)As alloy system more closely must include technologies designed to reduce strain in the diodes.

APPENDIX

HYDROSTATIC STRESS APPARATUS AND TECHNIQUES*

A. Portable Pressure Generator

Helium gas is supplied to the pressure cell from a remote, portable intensifier driver system, assembled from commercially available parts.** This pressure generator can provide up to 14 kilobars (∿200,000 psi) of compressed helium. A block diagram of the portable pressure generator is shown in Fig. 90.

The pressure generator consists of two stages. In the first stage, the helium is compressed in an air-operated diaphragm compressor (Aminco-Model No. 46-14021) and is delivered to the high pressure end of the piston intensifier. The compressor is then isolated from the piston intensifier by a manual high-pressure needle valve (Harwood Engineering Model No. D-2684). Next, the piston intensifier (Harwood Engineering Model No. A2.5J) is driven by pumping oil (diesel turbine engine mobile oil #24) at its low pressure end to compress the helium to the desired value. A manganin wire gauge (Harwood Engineering Model No. E2512), in conjunction with a bridge circuit, is used to monitor the high pressure outputs from the piston intensifier.

Solenoid valves are used in the air lines of the air-operated hydraulic pump and compressor to turn them on or off. Pressure gauges are placed at the input of the first stage and at the input and output of the second stage of the compressor. The pressure connections to the various components of the pressure generator as well as to the optical cell are made with hard-drawn 316 stainless steel tubing (0.1875 in. o.d. by 0.025-in. i.d.) supplied by Harwood Engineering Company, and coupled with standard Harwood gland nut and collar. Before coupling, the tube had to be coned and threaded.

For safety, rupture disks and release valves are provided at the input and output of the two-stage air-operated diaphragm-type compressor. The complete assembly is housed in a 0.25-in. steel-plated frame, and hinged doors are used to absorb some of the impact in case of explosion.

The operating procedure for the pressure generator is as follows:

(1) All release valves are to be closed; the oil return reservoir valve and the needle valve are to be opened.

*Contributed by Y. Juravel and P. M. Raccah, Yeshiva University.

**The design of the pressure generator was obtained from Dr. J. Kafalas, Lincoln Laboratory, Lexington, Mass.

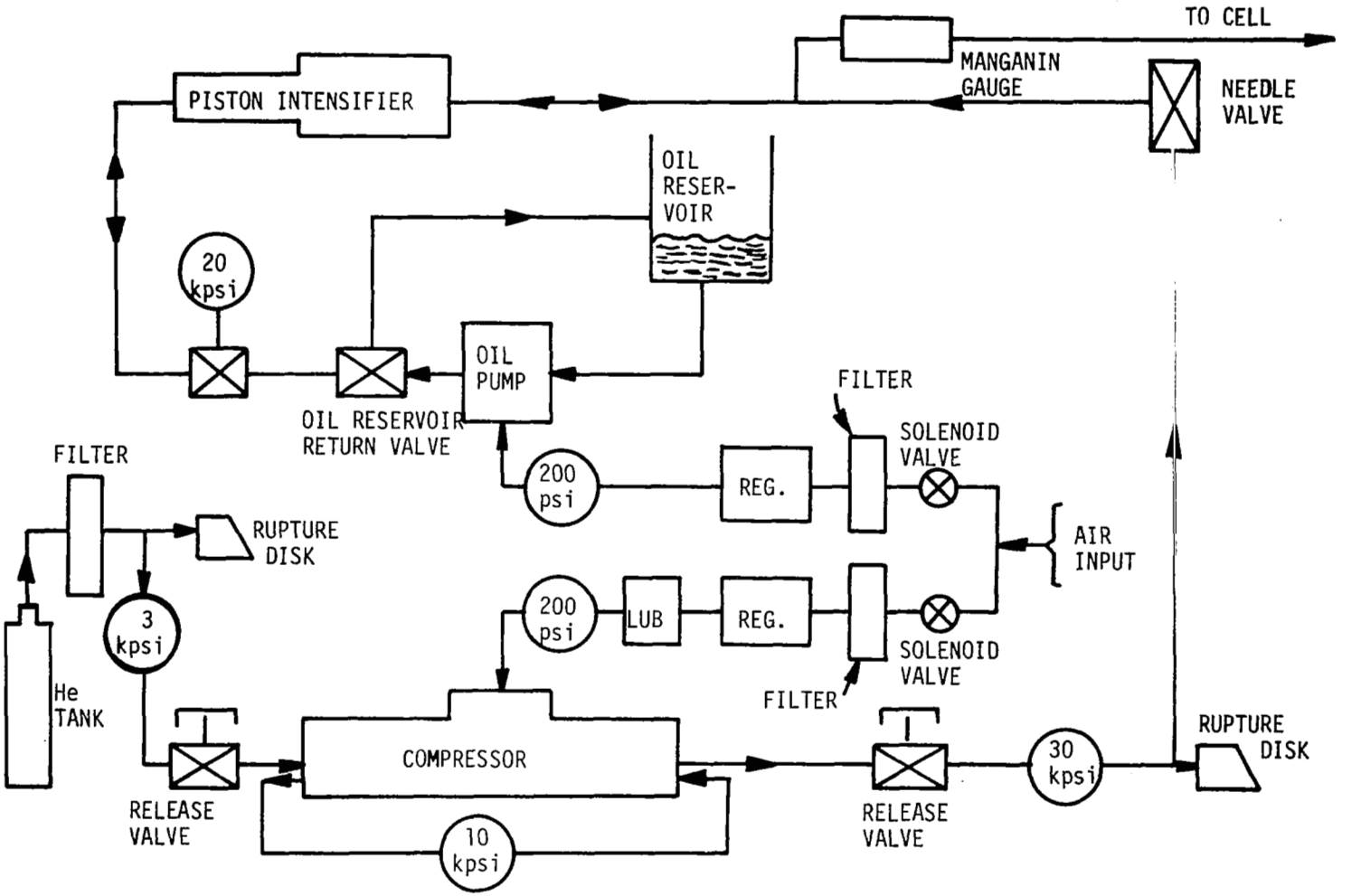

Figure 89. Block diagram of pressure generator.

(2) Set the helium input pressure at the helium tank to approximately 1500 psi and introduce the helium to the first stage of the compressor.
(3) Turn on the compressor (120 psi of compressed air is required) until the desired pressure indicated on the output gauge is reached. Never exceed 30,000 psi. At this point the compressed helium is fed into the high end of the piston intensifier, driving back the piston to its initial position. Helium is also being introduced through the manganin gauge to the pressure cell. The manganin gauge could also be used to monitor the output pressures. If higher pressures are desired, proceed to Step (4).
(4) Turn off the compressor, close the needle valve and the oil return reservoir valve.
(5) The hydraulic pump is then activated, which drives the piston intensifier, compressing the helium to the required value which is monitored by the manganin gauge.

To avoid optical misalignments, caused by the helium being introduced into the pressure cell and by mechanical vibrations of the hydraulic pump (transmitted to the pressure cell through the pressure tubing), the following procedure is used.

(1) The maximum pressure required is developed and introduced into the cell.
(2) Alignment is performed and the optics-electronics optimized.
(3) The experiment is then performed at the maximum pressure.
(4) The pressure is reduced at an extremely slow rate by controlling the opening of the oil reservoir valve. When the desired pressure is reached, the reservoir valve is closed and the experiment performed. This procedure is repeated for the next pressure and so on.

Also, to avoid systematic errors caused by the temperature dependence of the various parameters under investigation (i.e., transition energies, conductivity), no measurements were taken until five minutes after the pressure in the cell had been changed. This time interval allowed the interior of the cell to return to ambient temperature after the energy had been added or removed from the system by the compression or expansion of the gas.

B. Optical Pressure Cell

The principal design considerations of the optical pressure cell are the requirement of effective cryogenic pressure seals and the need

to keep the dimensions of the cell to a minimum. The cell was designed to be placed in a liquid-helium cryostat and is to contain two optical windows, an electrical port, a pressure port, and a port for the sample holder for easy access to the sample under investigation. By using helium gas as the pressure-transmitting medium, hydrostatic pressures are possible at temperatures down to the freezing curve of helium; at lower temperatures the solidified helium is sufficiently soft and plastic that nearly hydrostatic conditions exist after slow cooling (ref. 63).

Figure 90 shows the assembly of the pressure cell and its various components. Beryllium copper is used since it is easy to machine and heat-treat and does not have the problem of brittle fracture at low temperatures as steel does (refs. 63 and 64). A cold-rolled Be-Cu rod (2.25 in. in diameter) of 1/2 hard "Berylco 25" alloy is used for the cell body.

The cell employs the conventional Bridgeman seal (refs. 65 and 66). This method uses the unsupported area principle, as shown in Fig. 90. The total pressure exerted on the mushroom head is transferred to the soft packing seal, which has an area less than that of the bore since the stem of the mushroom plug is floating. Thus, no matter what pressure is to be contained, the pressure in the seal is always higher. The hydrostatic pressure in the cell tends to compress the packing seals, exerting a force against the mushroom stem. When sufficient force is exerted, the stem will be "pinched off" creating a very hazardous situation since the stem is expelled with a velocity comparable to that of a rifle bullet. The dimensions of the plug should be chosen such that the pressure exerted on it is well below its tensile strength (ref. 67). As a general rule the stem's diameter should be about half the total bore diameter (ref. 65). A supporting plug is used not only to hold the packing seals in place but also to safeguard against a pinch-off stem.

1. Optical Windows. - In selecting a window, consideration must be given to the following factors:

(1) Transmission range of interest
(2) Ability to resist stress
(3) The effect of a helium atmosphere on window characteristics
(4) Ability to withstand thermal shock at low temperatures
(5) Thermal contraction so that it could maintain a good seal at low temperatures.

The ability to resist stress is a function of the window's thickness and the unsupported area (aperture). The equation used to calculate the maximum allowed pressure that the window can withstand before rupture is

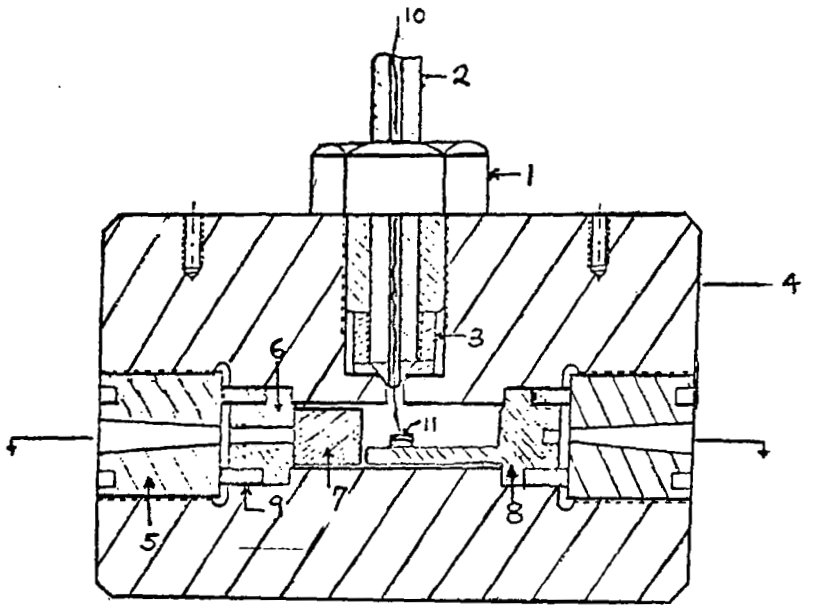

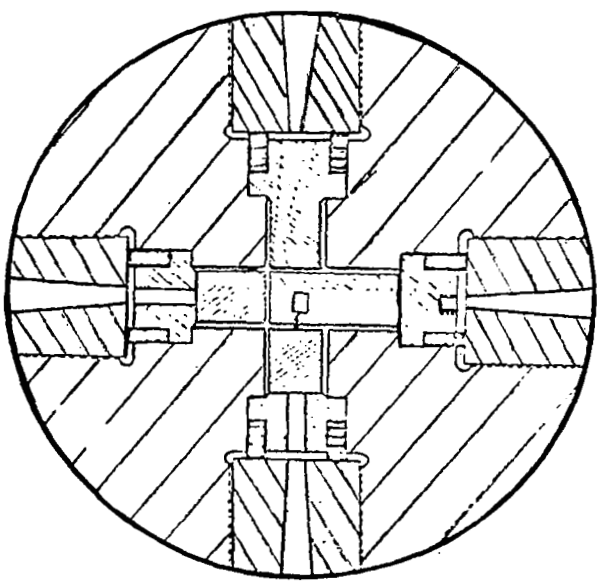

1. Gland nut
2. Tubing
3. Tubing collar
4. Be-Cu cell body
5. Support plug
6. Mushroom plug
7. Window
8. Sample holder
9. Seals
10. Teflon insulated wire
11. Diode

Figure 90. Assembly of the pressure cell.

$$P = \frac{R}{\text{safety factor}} \left(\frac{t}{r}\right)^2 \qquad (22)$$

where R is the modulus of rupture of the window,

t is the window's thickness, and

r is the radius of the aperture.

A safety factor of 2 is used in the above calculations of P. Due to the size of the optical cell we are limited to a thickness t = 0.25 in. and an aperture r = 0.0625 in. It should also be noted that the modulus of rupture R usually decreases with a decrease in temperature, and thus the allowed pressure is decreased.

Sapphire (ref. 68) with a thickness of 0.25 in. and a diameter of 7/32 in. was chosen as the window material. It possesses an 85% transmission (for a 1-mm-thick plate) between the spectrum range of 2,800 Å to 5 μm. Also, the modulus of rupture of sapphire is 65,000 psi. Thus, a maximum pressure of 520,000 psi could be achieved before the window shatters.

2. Optical Mushroom Plug. - The face of the optical mushroom plug is surface-ground and lapped (ref. 70). The seal is satisfactory when the plug can be picked up by lifting the window without separating window and plug. The matching flat surfaces provide the gas-tight seal to prevent leakage out of the center hole. A thin layer of adhesive mixture made of equal parts of GE-7031 varnish and toluene (ref. 64) is used as an alternative method of bonding. This method makes it possible to use a window whose face is scratched and therefore no longer adheres properly.

3. Pressure Seals. - The pressure seals consist of bronze, indium, and copper rings (ref. 64). Small beryllium copper (Be-Cu) rings of triangular cross section (delta rings) are used to prevent extrusion of the packing rings. The delta rings are held in place by a Be-Cu support ring that is supported by the threaded support plug. The assembly of the rings is shown in Fig. 91.

The bronze and copper rings serve to contain the soft indium ring. Indium is very effective as a gas seal because it adheres well to the Be-Cu walls to provide an excellent initial seal, and because it flows easily to maintain a seal during thermal cycling. Rubber is not a good seal since it becomes brittle at low temperatures (ref. 65).

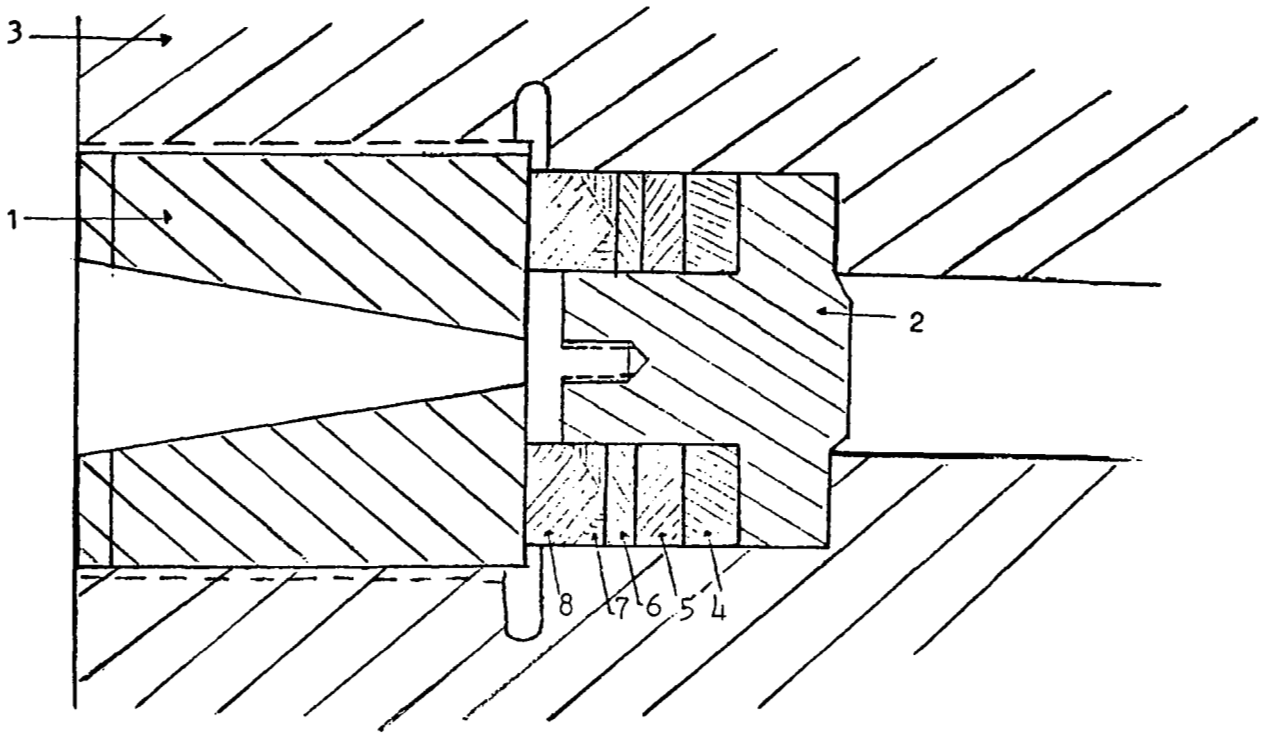

1. Support plug
2. Mushroom plug
3. Cell body
4. Bronze ring
5. Indium ring
6. Copper ring
7. Be-Cu delta rings
8. Be-Cu support ring

Figure 91. Ring assembly, use of the unsupported area technique.

The mushroom plug and packing are removed as a unit, using an extractor tool that screws into the last 0.0625-in. of the aperture hole. This allows easy replacement of the seals, which is required to change samples.

The threaded support plug has a 12° tapered aperture hole to reduce shadowing. A key slot was made for a 1/2-in. wrench so that it can be screwed in flush with the cell body. The support plug was designed to withstand 200,000 psi without shearing.

4. Electrical Terminals. - There are two methods of introducing electrical leads into the cell. Fine wires can be led down the pressure

tubing from a conventional closure at room temperature. Alternatively, one of the windows in the optical cell is replaced by an electrical plug similar to the design by Blosser and Young (ref. 70).

To provide an electrical plug for the cell, wires are embedded in a conical epoxy shell that fits into a conical opening of the plug. A Be-Cu cone is used to force a seal against the plug shown in Fig. 92. Several attempts were made to introduce the electrical leads by this method without success. Instead, a Teflon-insulated 0.0045-in.-diameter silver wire was introduced into the cell through the pressure tubing from a conventional high-pressure closure. The closure is similar in design to the manganin wire gauge which was supplied by Harwood Engineering Co.

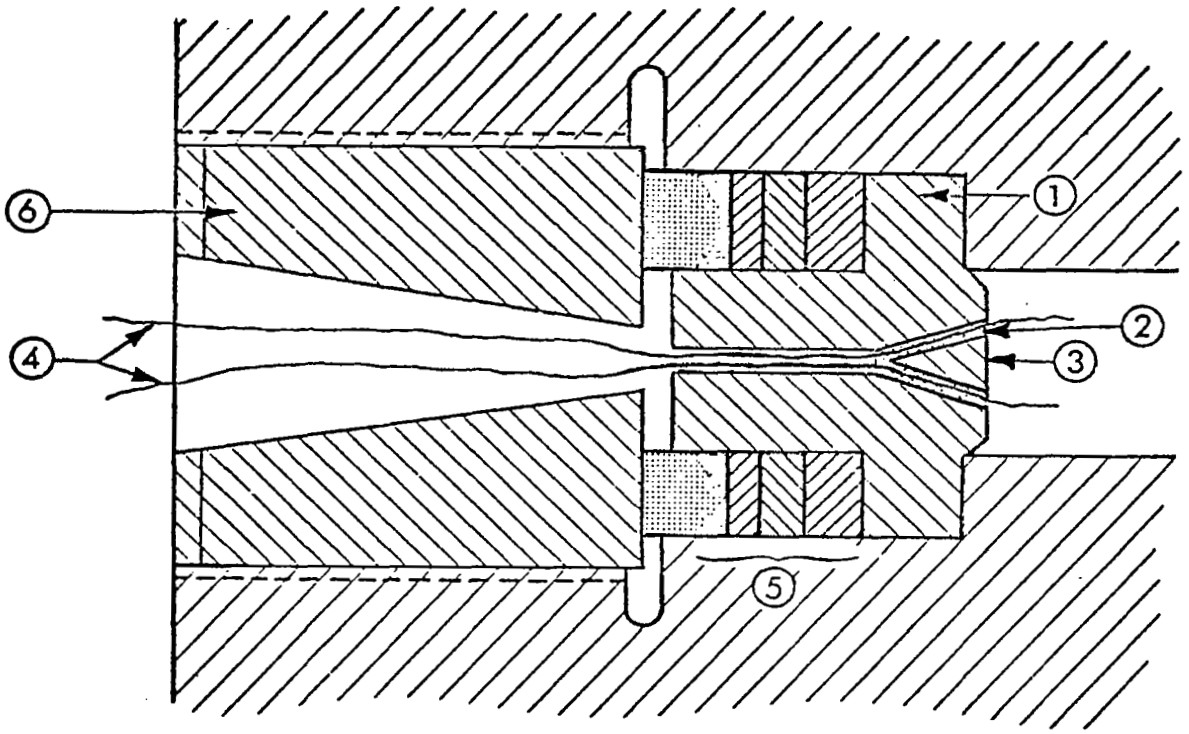

Figure 92. Cell closure for electrical leads.

The diagram of the closure is shown in Fig. 93. The anode made of hardened steel is used as the electrode. A lava cone acts as the seal as well as an insulator. "Spaghetti" is used to insulate the wire from the main body. Before assembly, GE-RTV102 silicone rubber adhesive was spread around the lava cone. The assembly was made with the wet adhesive to obtain a good seal.

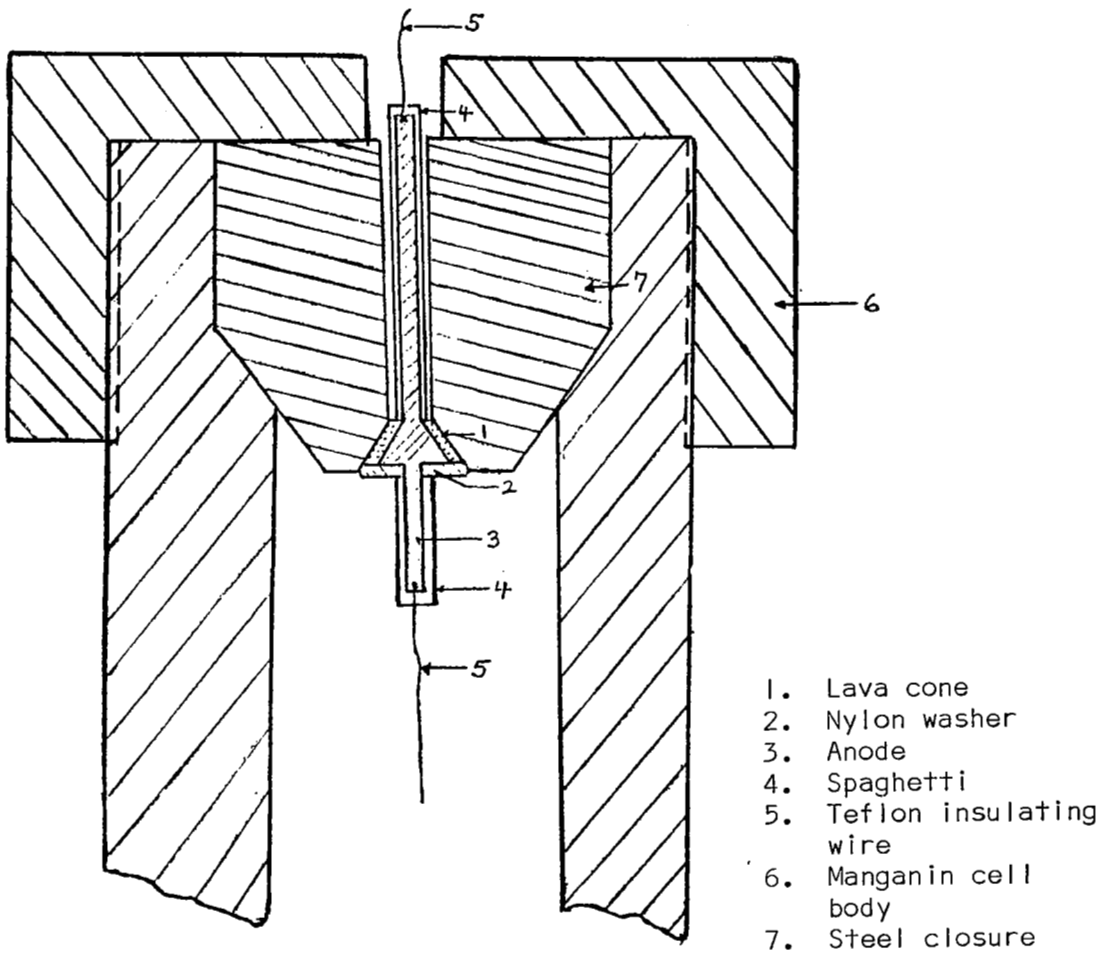

Figure 93. A conventional seal for introducing electrical leads.

The samples under investigation were mounted on a BeO_2 substrate that was attached to the sample holder with GE-7031 varnish. The Teflon-insulated wire was soldered to the positive terminal of the sample on an indium strip made on the BeO_2 substrate. The other lead was silver-painted to the sample holder, which makes contact with the body of the cell and acts as the other electrode.

C. Properties of Helium

The equation proposed to represent the melting curve of helium is

$$\frac{P}{16.45} = \left(\frac{T}{0.992}\right)^{1.5544} - 1 \tag{23}$$

where p is the pressure in atmosphere. This equation agrees with experiment within 1% down to 2.4°K, which is very close to the λ point. Therefore, the quantum effect of helium in considering the behavior at temperatures greater than 2.4°K can be ignored. The solidification of helium under pressure occurs at temperatures higher than the normal liquid vapor critical temperature (T_c = 5.2°K). Also, helium gas is completely transparent in the visible and near infrared, and has a very small change of refractive index with pressure.

D. Pressure Determination

The determination of pressure in the cell becomes a problem at temperatures below which helium solidifies. Above the freezing point of helium, the pressure is measured externally, using a Harwood Engineering, Inc., manganin gauge and bridge. The manganin gauge is located in a separate pressure vessel at room temperature. The pressure can be measured within 100 psi, and there was no apparent pressure change during a run. The gauge vessel also serves a secondary function as a pressure reservoir, its larger volume suppressing the variation of pressure with temperature in the cell.

Below the freezing point, the manganin gauge no longer gives the cell's pressure, since the pressure line is blocked with frozen helium. The final pressure in the cell at temperatures below the freezing point of helium can be estimated from thermodynamic data available for solid helium. Assuming cooling at constant volume from the freezing point determined by the gauge pressure, the calculated final pressure can thus be determined.

REFERENCES

1. H. Kressel and H. Nelson, RCA Review 30, 106 (1969).
2. H. Nelson and H. Kressel, Applied Physics Lett. 15, 7 (1969).
3. J. I. Pankove, *Optical Processes in Semiconductors*, (Prentice-Hall New York, 1971).
4. H. Kressel, "Semiconductor Lasers," in *Lasers*, Vol. 3, A. Levine and A. DeMaria, Eds., (Marcel Dekker, New York, 1971).
5. C. J. Nuese, H. Kressel, and I. Ladany, IEEE Spectrum 9, 28 (May 1972).
6. H. Nelson, U.S. Patent 3,565,702 (1971).
7. H. F. Lockwood and M. Ettenberg, J. Crystal Growth 15, 81 (1972).
8. H. Kressel, F. Z. Hawrylo, and N. Almeleh, J. Appl. Phys. 40, 2224 (1969).
9. Zh. I. Alferov, et al., Sov. Phys. Semiconductors 5, 987 (1971).
10. J. F. Womac and R. H. Rediker, J. Appl. Phys. 43, 4129 (1972).
11. J. K. Butler and H. Kressel, J. Appl. Phys. 43, 3403 (1972).
12. M. J. Adams and M. Cross, Solid-State Electron. 14, 865 (1971).
13. H. Kressel, H. Nelson, and F. Z. Hawrylo, J. Appl. Phys. 41, 2019 (1970).
14. F. Stern, Phys. Rev. 133, A1653 (1964).
15. J. Zoroofchi and J. K. Butler, J. Appl. Phys. 44, 3697 (1973).
16. H. Kressel, H. F. Lockwood, and F. Z. Hawrylo, J. Appl. Phys. 43, 561 (1972).
17. H. Kressel, H. F. Lockwood, and H. Nelson, IEEE J. Quantum Electron. QE-6, 278 (1970).
18. A. G. Sigai, C. J. Nuese, R. E. Enstrom, and T. Zamerowski, J. Electrochem. Soc. 120, 947 (1973).
19. C. J. Nuese, D. Richman, and R. B. Clough, Met. Trans. 2, 789 (1971).
20. R. E. Enstrom, C. J. Nuese, V. S. Ban, and J. R. Appert, *Proc. 4th Int. Symp. on Gallium Arsenide and Related Compounds*, to be published.
21. M. R. Lorenz, W. Reuter, W. P. Dumke, and R. J. Chicotka, Appl. Phys. Lett. 13, 421 (1969).
22. R. Z. Bachrach and B. W. Hakki, J. Appl. Phys. 42, 5102 (1971).

23. J. Chevallier and A. Laugier, Phys. Stat. Sol. (a) 8, 437 (1971).

24. A. Onton, and R. J. Chicotka, Phys. Rev. B4, 1847 (1971).

25. D. R. Scifres, H. M. Macksey, N. Holonyak, Jr., and R. D. Dupuis, J. Appl. Phys. 43, 1019 (1972).

26. E. W. Williams, A. Ashford, P. Porteous, and A. M. White, Solid State Commun. 8, 501 (1970).

27. E. W. Williams and H. B. Bebb in *Semiconductors and Semimetals*, Vol. 8, R. K. Willardson and A. C. Beer, eds., p. 321 (Academic Press, New York, 1972).

28. O. Röder, U. Heim, and M. H. Pilkuhn, J. Phys. Chem. Solids 31, 2625 (1970).

29. U. Heim, O. Röder, H. J. Queisser, and M. H. Pilkuhn, J. Luminescence 1, 542 (1970).

30. J. U. Fischbach, G. Benz, N. Stath, and M. H. Pilkuhn, Solid State Commun. 11, 725 (1972).

31. J. M. Chamberlain, H. B. Engun, K. A. Gehring, and R. A. Stradling, Solid State Commun. 9, 1563 (1971).

32. C. J. Nuese, A. G. Sigai, M. S. Abrahams, and J. J. Gannon, J. Electrochem. Soc. 120, 956 (1973).

33. D. M. Eagles, J. Phys. Chem. Solids 16, 76 (1960).

34. A. M. White, P. J. Dean. K. M. Fairhurst, W. Bardsley, E. W. Williams, and B. Day, Solid State Commun. 11, 1099 (1972).

35. P. J. Dean, quoted by H. C. Casey, Jr., and F. A. Trumbore, Mat. Sci. Eng. 6, 69 (1970).

36. H. Kressel, F. Z. Hawrylo, M. S. Abrahams, and C. J. Buiocchi, J. Appl. Phys. 39, 5139 (1968).

37. B. Tuck, J. Phys. Chem. Solids 28, 2161 (1967).

38. H. J. Queisser and M. B. Panish, J. Phys. Chem. Solids 28, 1177 (1967).

39. G. B. Stringfellow, J. Appl. Phys. 43, 3455 (1972).

40. C. Alibert, G. Bordure, A. Laugier, and J. Chevallier, Phys. Rev. 6B, 1301 (1972).

41. M. R. Lorenz and A. Onton, *Proc. of the Tenth Int. Conf. on the Physics of Semiconductors* (Cambridge, Mass., 1970), p. 444.

42. C. J. Nuese, A. G. Sigai, and J. J. Gannon, Appl. Phys. Lett. 20, 431 (1972).

43. M. B. Panish and M. Ilegems, Third Int. Symp. on GaAs, Aachen, Germany, Paper 7.

44. M. Ilegems and G. L. Pearson, Proc. of the Second Int'l Symposium on GaAs, The Institute of Physics and the Physic. Society of London, p. 3 (1969).

45. H. Kressel, J. K. Butler, F. Z. Hawrylo, and M. Ettenberg, RCA Review 32, 393 (1971).

46. H. Kressel and F. Z. Hawrylo, U. S. Patent 3,747,016 (1973).

47 J. C. Dyment, L. A. D'Asaro, J. C. North, B. I. Miller, and J. E. Kipper, Proc. IEEE 60, 726 (1972).

48. This method was first applied to laser diodes by J. C. Dyment, Appl. Phys. Letters 10, 84 (1967).

49. H. Yonezu et al., Japan. J. Appl. Phys. 12, 1585 (1973).

50. H. Kressel, H. Lockwood, F. H. Nicoll, and M. Ettenberg, IEEE J. Quantum Electronics QE-9, 383 (1972).

51. B. W. Hakki, J. Appl. Phys. 45, 288 (1974).

52. R. W. Keyes, IBM J. Research & Develop. 15, 401 (1971).

53. H. Kressel and H. P. Mierop, J. Appl. Phys. 38, 5419 (1967).

54. Extensive data are given by P. G. Eliseev in *Semiconductor Light Emitters and Detectors*, A. Frova, ed., (North Holland Publishing Co., Amsterdam, 1973).

55. M. Ettenberg, H. S. Sommers, Jr., H. Kressel, and H. F. Lockwood, Appl. Phys. Letters 18, 571 (1971).

56. H. Kressel, N. E. Byer, H. F. Lockwood, F. Z. Hawrylo, H. Nelson, M. S. Abrahams, and S. H. McFarlane, Met. Trans. 1, 635 (1970).

57. For a review see H. Kressel and H. F. Lockwood, J. de Physique, Suppl. No. 4, 35, C3-223 (1974).

58. G. E. Fenner, J. Appl. Phys. 34, 2955 (1963).

59. J. Feinleib, S. Groves, W. Paul, and R. Zallen, Phys. Rev. 131, 2070 (1963).

60. M. J. Stevenson, J. D. Axe, and J. R. Lankard, IBM J. Res. and Develop. 7, 155 (1963).

61. T. Kobayashi and K. Sugiyama, Japan. J. Appl. Phys. 12, 1388 (1973).

62. J. W. Stewart, Phys. Rev. 129, 1950 (1963).

63. W. Paul and G. B. Benedek, "Nonmagnetic High Pressure Vessels," Rev. Sci. Instr. 30, 874 (1969).

64. D. B. Fitchen, "Four-Window Cell and Cryostat for High Pressure Studies at Liquid Helium Temperature," Rev. Sci. Instr. 34, 673 (1963).

65. C. C. Bradley, *High Pressure Methods in Solid State Research*, (New York Plenum Press, New York, 1969), pp. 28-32.

66. A. M. Warschauer, W. Paul, "Unsupported Area High Pressure Seal," Rev. Sci. Instr. 28, 62 (1957).

67. P. W. Bridgeman, *The Physics of High Pressure*, (G. Bell and Sons, London, 1958), Chapt. II.

68. Adolf Meller Company brochure, "Meller Quality", Adolf Meller Company, P. O. Box 6001, Providence, Rhode Island (1973).

69. E. Fishman and H. G. Drickamer, "Equipment for High Pressure Optical Spectroscopic Studies," Anal. Chem. 28, 804 (1956).

70. L. G. Blosser and H. S. Young, "Electrical Seal for Use at High Pressure," Rev. Sci. Instr. 33, 1007 (1962).

*U.S. GOVERNMENT PRINTING OFFICE: 1975 - 635-053/96